# Status report on the WP2 of the Swiss-Danish instrumentation work packages for the European Spallation Source, ESS

Εστία

a

## focusing reflectometer for small samples

using the

## *Selene* guide concept

*Selene*

focusing reflectometer

Jochen Stahn
Uwe Filges
Panagiotis Korelis
Emmanouela Rantsiou
Tobias Panzner

Ursula Hansen
Marité Cardenas

**project team**

| Jochen Stahn | Laboratory for Neutron Scattering | senior scientist |
| | Paul Scherrer Institut | - project leader |
| | Switzerland | - concept |
| | jochen.stahn@psi.ch | - experiements |
| | +41 56 310 2518 | - McStas |

| Panagiotis Korelis | Laboratory for Neutron Scattering | post-doc |
| | Paul Scherrer Institut | - McStas (gravity) |
| | Switzerland | |
| | panagiotis.korelis@psi.ch | |
| | +41 56 310 5813 | |

| Uwe Filges | Laboratory for Developments and Methods | senior scientist |
| | Paul Scherrer Institut | - McStas, MCNPX |
| | Switzerland | |
| | uwe.filges@psi.ch | |
| | +41 56 310 4606 | |

| Tobias Panzner | Laboratory for Developments and Methods | pst-doc |
| | Paul Scherrer Institut | - McStas |
| | Switzerland | - experiements |
| | tobias.panzner@psi.ch | |
| | +41 56 310 4342 | |

| Emmanouela Rantsiou | Laboratory for Developments and Methods | pst-doc |
| | Paul Scherrer Institut | - McStas, MCNPX |
| | Switzerland | |
| | emmanouela.rantsiou@psi.ch | |
| | +41 56 310 4631 | |

| Marité Cardenas | Nano-Science Center | senior scientist |
| | University of Copenhagen | - scientific advice |
| | Denmark | |
| | cardenas@nano.ku.dk | |
| | +45 35 320 431 | |

| Ursula Bengaard Hansen | Nano-Science Center | student assistant |
| | University of Copenhagen | - McStas |
| | Denmark | - experiements |
| | uhansen@fys.ku.dk | |
| | +45 60 478 615 (mobile) | |

| Beate Klösgen | Department for Physics, Chemistry and Pharmacy | associate professor |
| | University of Southern Denmark | - scientific advice |
| | Denmark | |
| | kloesgen@sdu.dk | |
| | +45 6550 2561 | |

| *Selene* |  moon, dark side | titan goddess |
| | detail of the ceiling painting | |
| | *Selene and Endymion* | |
| | at the | |
| | *Ny Carlsberg Glyptotek*, Copenhagen | |

## Εστία                                    a focusing reflectometer for small samples

The *Swiss-Danish Instrument Initiative* presents Εστία[1], a concept for a focusing reflectometer optimised for small samples. The scientific focus of this instrument is the investigation of the structural and magnetic depth profiles of solid film structures. Probing liquid/solid interfaces or lateral structures is also possible, with a compromised performance. To account for these types of samples we suggest to also build a complementary reflectometer for liquid surfaces and organic samples in general, and eventually one instrument dedicated to the investigation of lateral structures.

The unique feature of Εστία is its truly focusing neutron guide, based on the *Selene* concept. Its point-to-point focusing leads to a drastically reduced beam intensity in the guide, while almost conserving the phase space density actually needed for the measurements. Also the beam is convergent at the sample which avoids over-illumination of the sample (if required) and of the sample environment. The special geometry allows for efficient optics to polarise and filter the beam, or to implement constant resolution without using choppers.

The convergent beam can be used efficiently on sample surfaces reaching from $1 \times 1\,\text{mm}^2$ to $40 \times 10\,\text{mm}^2$. To allow for high detector angles and to reduce the influence of gravity, the preferred scattering plane is horizontal. The wavelength range $\lambda = 5\,\text{Å}$ to $9.4\,\text{Å}$ was obtained by reducing the counting time and avoiding the proton pulse duration for data acquisition.

Εστία provides several operation modes, where switching from one to the other implies only the insertion of some optics or the activation of a slit. In a low-resolution mode it will be possible to investigate dynamic processes in the second time range, or to trace the influence of external conditions on magnetic properties. An other mode gives the performance of a conventional TOF reflectometer, allowing for the separation of specular and off-specular scattering. And using the high divergence of the beam for energy-angle encoding results in a constant resolution for specular reflectivity, a wide $q_z$-range, and in a *nice q*-space volume for off-specular measurements.

Further options are the generation of a clean parallel beam, e.g. for GISANS experiments, or the addition of spin echo techniques. The instrument will have a full polarisation and polarisation analysis option. It will allow for heavy and bulky sample environment, and accept high magnetic fields.

---

[1]This is a working title. Estia is the Greek goddess of the hearth, the family, and architecture. In modern Greek the word means *point of interest or importance* and is used for example when adjusting a telescope or a camera lens.

# Contents

# 1 Scientific Case

[5 pages] [Describe the key scientific drivers and relate them to the scientific ambition expected of the ESS. Highlight any new science that the concept would enable and justify its significance in the wider scientific context. Estimate the size and impact of the existing and potential user community. Compare the concept to similar existing instruments and other concepts within the same instrument class at the ESS. Identify the infrastructure and supporting facilities necessary to support the proposed experiments.]

Physical, chemical and biological states or processes at interfaces and surfaces are getting more and more into the focus of both, fundamental and applied research. This field reaches from improving surface conditioning or understanding biological mechanisms at cell membranes via the improvement of magnetic data storage and processing to the investigation of novel phenomena when conflicting properties are forced to coexist on an atomic scale.

One of the best suited methods to investigate interfaces is reflectometry. Where neutron reflectometry in particular provides a high penetration depth, and a sensitivity also for light elements. And it probes magnetism:w
. Accordingly the neutron reflectometry user community and the requirements for the instruments are quite broad. As a consequence the ESS *Scientific and Technical Advisory Panel for reflectometry* recommended to build two reflectometers, one optimised for soft matter samples including the possibility to measure on liquid surfaces. The other one with complementary (and overlapping) characteristics is to essentially serve the research on solid-state materials. This proposal deals with the second, the solid-state reflectometer.

The combination of the highly brilliant neutron beam at the ESS with novel neutron optics and a novel guide design will improve the performance of reflectometry with polarised neutrons for small samples composed of thin layers by up to two orders of magnitude compared to existing instruments. The reason for this gain is that the design enables changing the resolution conditions in a very wide range, and that it opens the possibility for new measurement schemes. In the following we present a not-complete list of key applications for a focusing reflectometer at ESS, a list of design criteria, and the performance expected.

## 1.1 selected scientific opportunities

### 1.1.1 magnetic heterostructures

Heterostructures involving magnetic materials are the basic building blocks of a large number of magneto-electronic devices such as read heads or magnetic random access memories. In addition such heterostructures are increasingly being used as magnetic sensors in industrial applications and in automotive industry. The performance of the magnetic devices relies on the magnetic and elastic properties of the individual layers and on the coupling between the layers. These effects are a function of the morphology and microstructure of the grown layers and accordingly change during the growth of the heterostructures. To access the structure within the layers and the perfection of the layers, reflectometry with polarised neutrons is a very powerful tool as it allows performing vector-magnetometry in heterostructures layer by layer. The current trend is to decrease the size of the devices and to go towards thinner layers. Therefore, it is very important to adapt the experimental techniques to cope with the small cross sections of these materials.

example to come[1]

---

[1] provided by Bernhard Keimer, Max Planck Institut für Festkörperforschung, Stuttgart, Germany

### 1.1.2   multifunctional materials

The last few years have witnessed a tremendous activity in the search for multifunctional materials combining magnetic, charge and orbital degrees of freedom, which may be controllably tuned. These systems combine several *ferroic* properties, i.e. symmetry breaking order parameters such as polarisation, magnetisation, and strain, which are subject to control parameters such as electric and magnetic field, and stress, respectively. The most direct way to engineer the desired functionality at room temperature is the combination of ferroic materials in a heterostructure. For the investigation of the interactions between the magnetic and non-magnetic layers neutron reflectivity is the only means to directly determine the formation of magnetic order and domain formation.

**strain-induced ferromagnetism at the film/substrate interface in orthorhombic $LuMnO_3$ thin films**
Materials featuring the co-existence of coupled magnetic and ferroelectric order allow the switching of magnetic moments by an electric field and vice versa.[1, 2] Experimentally, only a few multiferroic materials are known to be ferromagnetic (FM), with the large majority being antiferromagnetically ordered. This class of materials can potentially be used for future magnetic storage devices with an electronic read-out. To identify and probe the spatial extend (thickness dependence) of ferromagnetism in a thin film non-destructively, polarised neutron reflectomentry reaching large $q_z$ is the best suited technique available.[3, 4] Single crystalline like thin films of orthorhombic $LuMnO_3$, a material which is known to exhibit magnetically-induced ferroelectricity with an E type antiferromagnetic (AFM) ground state, were found to have FM localised close to the substrate-film interface.[5] Surprising is the fact, that an intrinsic robust AFM can be converted into a FM with $T_C > T_N$. The most likely origin is growth induced strain at the substrate/film interface and a change in crystalline symmetry.

Future experiments will address the exchange biased coupling of the FM and AFM when applying electric fields while conducting PNR measurements. The samples have to have electrodes structured onto the surface which limits the space available to conduct the reflectivity measurements.[2]

### 1.1.3   novel electronic phases at interfaces

Insulating metal-oxide heterostructures may develop mobile electron gases at the interfaces, which show a rich spectrum of physical properties which are of increasing scientific and technological interest. A prominent example is the interface $LaSrO_3/SrTiO_3$. For example it has been established that depending on the number of layers, the interfaces show an integer Quantum Hall Effect, magnetism, or even superconductivity. Gate fields can be used to alter the carrier density to an extent that the electrons are driven to become superconducting. For the investigation of the magnetic and superconducting properties neutron reflectometry is the method of choice as it is sensitive to buried interfaces.

**Induced magnetism at oxide interfaces**     The recent discoveries of a number of fascinating unexpected phenomena at interfaces between different perovskite oxides have been received with tremendous enthusiasm, leading to the emergence of the field of oxide interface engineering.

The conduction properties found at some interfaces between insulating oxides have attracted a lot of attention. Such conducting interfaces, first discovered in 2002 between a Mott insulator ($LaTiO_3$) and a band insulator ($SrTiO_3$) [6] and in 2004 between two band insulators ($LaAlO_3$ and $SrTiO_3$) [7], have been shown to host two-dimensional electron gases. These discoveries generated an impressive amount of work trying to understand the origin of the conductivity and studying the properties of these fascinating systems, among them superconductivity and magnetism [8, 9].

Several oxide interface systems display induced magnetic structures. Among those, the observation of exchange bias in superlattices composed of nominally paramagnetic metallic $LaNiO_3$ and semiconducting ferromagnetic $LaMnO_3$ ultrathin layers is particularly exciting [10]. A shift of the magnetisation loop is observed when samples are field-cooled to below $20 - 25\,K$. Curiously, the effect appears mainly for superlattices grown along the less conventional [111] pseudocubic direction, which maximises the interactions between the Mn and Ni atoms at the interface.

The presence of exchange bias reveals the existence of a strong interfacial coupling, likely to be related to a charge transfer $Mn^{3+} + Ni^{3+} \rightarrow Mn^{4+} + Ni^{2+}$. It also implies the emergence of magnetism in the nominally paramagnetic $LaNiO_3$ layers. Although a number of different magnetic structures have been proposed to explain this intriguing observation [10], the exact magnetic properties of the interface is unclear. The ultrathin $LaNiO_3$ layers could be undergoing a transition to an antiferromagnetic state with the usual up-down spin

---

[2]provided by Christof Schneider, Paul Scherrer Institut, Switzerland

arrangement, or the more complex spin arrangement common to the other members of the rare earth nickelates family [11] even evolving to a spin-density wave.[10]

Moreover, TEM measurements have shown that the LNO/LMO interface is not quite the same as the LMO/LNO one. In the first case, a 1 monolayer interdiffusion is observed versus a two monolayer roughness for the second system. Preliminary magnetic and electrical transport measurements on these bilayers have also provided evidence for a significantly different magnetic behaviour. As a result, it is likely that the interface charge transfer and subsequent magnetic coupling could be different.

For several systems including the LNO/LMO superlattices described in some detail above, neutron reflectivity would be an ideal probe of the magnetic properties induced through the interface. Indeed, a precise chemical and magnetic profile measurement with monolayer sensitivity would represent an important step towards the understanding of charge transfer induced magnetism through these interfaces. [3]

### 1.1.4    in-situ monitoring of film growth

While the in-situ characterisation of thin films during growth by means of electron diffraction, for example RHEED, and even scanning probe microscopy and photo-spectroscopy is common practise, only few efforts have been made to characterise the evolvement of the magnetic properties during the deposition of the layers. Neutron reflectometry is the method of choice as it measures directly the magnitude and the orientation of the magnetic moments throughout the heterostructure on a microscopic scale in contrast to XMCD where only the surface is measured and vector information is lost.

An optimised beam line at ESS would allow conducting in-situ reflectometry with polarised neutrons in real time.[4]
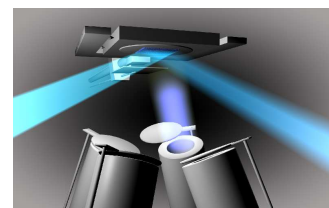
### 1.1.5    diffusion processes in solids

Self-diffusion of atoms in solids is a fundamental point-defect mediated matter transport process. It plays a key role for the design and optimisation of materials as well as for the performance of devices in various branches of technology like energy storage/conversion, electronic devices, sensor technology and nanostructural materials design. The investigation of diffusion processes on very short lengths scales ranging from atomic distances up to some tens of nanometers is an emerging field of research. It is especially important for the characterisation of nanostructured materials, metastable compounds and thin films as well as for the study of diffusion process close to room temperature and ultra-slow diffusion processes.

A method which can be used to realise such measurements is neutron reflectometry in combination with isotope multilayers [12]. Using this method, the destruction of an artificial lattice of stable isotopes by thermally induced interdiffusion is detected. Up to now, the method was used ex-situ to study self- and impurity diffusion in complex amorphous materials and metastable chemical compounds [12, 13, 14], in nano-crystalline metals [15], in single crystalline semiconductors [16], in ion conductors [17] and in electrode materials for Li-ion batteries [18].

In the framework of a seminal advancement of the method, in-situ experiments at elevated temperatures should be carried out in order to monitor real-time atomic migration processes in equilibrium and non-equilibrium states. This requires a superior time resolution (seconds) for specular reflectivity, the use of small samples ($< 25\,\mathrm{mm}^2$) due to handling with expensive isotopes, and a $q_z$-range up to $0.4\,\text{Å}^{-1}$ for the detection of diffusion close to atomic distances.[5]

### 1.1.6    laterally structured surfaces

For laterally structured samples it is essential to measure the off-specular reflected signal. It is important to stress that the proposed instrument can be operated almost like a conventional TOF reflectometer. *Almost* means that the beam is still convergent. The only restriction is the maximum sample width, all other features are not compromised. I.e. the brilliance available for off-specular measurements is about the same as for a conventional instrument.

---

[3]provided by Jean-Marc Triscone, Université de Genève, Switzerland
[4]provided by Peter Böni, Technical University Munich, Germany
[5]provided by Harald Schmidt, Clausthal University of Technology, Germany

**finite size effects in complex oxides**     A number of interesting finite size effects on the magnetic and superconducting properties could be studied in nanostructured samples of complex oxides, like in manganites, ruthenates or cuprates. In a collaboration between the University of Fribourg and the laboratory for nanotechnology at PSI, x-ray lithography and lithography with an e-beam writer have been used already to produce large area samples (up to $4\,mm^2$) with micro- and nanostructures (squares and lines with different sizes and spacings).[6]

## 1.2     performance criteria

### 1.2.1     sample size

A reduction of the size of the neutron beam spot in PNR experiments to an area as small as $1\,mm^2$ is a very desirable improvement. It is of significant advantage for a number of samples that are of scientific interest in the field of magnetic and superconducting thin film materials. Specific examples are:[6]

**limited homogeneous area**     PLD grown thin film samples are generally limited in their lateral size. Most materials can be comfortably grown for sizes up to $5 \times 5\,mm^2$. These limits naturally arise due to the finite size of the laser plume and from the requirement of having a very homogeneous temperature over the entire substrate area. Larger area thin films and multilayers can be grown (for example by toggling) but at the cost of unwanted variations in thickness and structural and chemical homogeneity.

**scanning graded samples**     Multilayers with a ramp-type change of the layer thickness in one direction. These could be used to measure very efficiently, by scanning the neutron beam along the ramp direction, the influence of the layer thickness on the magnetic properties

**masking of contacts**     There are various types of devices based on oxide multilayers in which interesting magnetic effects can be induced by applying a voltage, for example in spintronic devices or in multiferroic ones. In most cases this requires electrodes which need to be contacted on the side of the sample. A small footprint would allow us to keep these contacts away from the area that is probed in the PNR experiments.
The figure shows a contacted sample as used for MuSR measurements.[19]
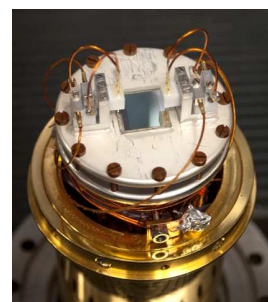
**limited sample size**     Bulk materials with interesting surface magnetic properties that can only be grown as relatively small single crystals. Examples are topological insulators in which characteristic magnetic states can be induced by electric currents. There are also ruthenates like $SrRuO_3$ for which a high temperature ferromagnetic surface state has been predicted.

**compatibility with other techniques**     Techniques complementary to neutron reflectivity like XRD, XMCD or resonant x-ray reflectometry performed at synchrotron sources, or probes like SQUID or transport measurements often impose a restriction for sample size of $5 \times 5\,mm^2$ to $1\,cm^2$. It is of huge advantage if the very same sample can be investigated also by neutron reflectometry.

### 1.2.2     measurement time

Short measurement times are needed for the in-situ investigations mentioned above. E.g. for the growth studies too long counting times result in the oxidation of the sample. To monitor real time atomic migration processes a time resolution in the second-range is necessary. And also when scanning parameter ranges (e.g. external electric or magnetic field, temperature) a fast (*quick and dirty*) way to explore the phase diagram would be favourable to identify the most interesting conditions for a high-quality measurement.

### 1.2.3     resolution

Heterostructures made from topological materials involving chiral structures such as the B20 compound MnSi or thin films (even monolayers) showing chiral magnetic order driven by the inversion symmetry at interfaces may become important functional materials for information technology or spintronics because the involved chiral entities are intrinsically very stable for they are protected by topology. In these materials several length scales compete with each other for example exchange length, modulation length, film thickness, etc. A wide

---

[6]provided by Christian Bernhard, Université de Fribourg, Switzerland

adaptability of the resolution (1% to > 10%) will allow to investigate the structural and magnetic properties over a very wide range of length scales while maintaining a high intensity.[7]

### 1.2.4    off-specular scattering

In-plain off-specular scattering gives information about the lateral inhomogeneity of the sample in the μm range. This allows for measuring the size of domains, or the periodicity and density profile of artificially structured surfaces.

### 1.2.5    polarisation

The investigation of magnetic depth profiles and of magnetic reversal processes is one of the main applications for the solid-state reflectometer. Spin polarisation and spin analysis are thus essential options of any respective neutron reflectometer already today, and even most of the soft matter reflectometers have at least a polarisation option.

### 1.2.6    extensions

**GISANS**     There is a growing demand to investigate laterally structured samples ... The beam needed for this Gracing Incidence Small Angle Neutron Scattering (GISANS) has to be highly brilliant, which restricts this method to the high-flux neutron sources. And often theses measurements are performed on SANS instruments rather than on reflectometers. As a result, the specular reflectivity needed for data analysis has to be obtained on an other instrument. It thus is desirable that a new reflectometer at a source with high brilliance allows for the implementation of a GISANS option.

**spin-echo methods**     To implement a spin echo option, several meter of free space before and eventually behind the sample are needed.

### 1.2.7    sample environment

There is a wide variety of equipment around the sample. In the scientific examples mentioned above this included cryomagnets, in-situ furnaces, PLD- or sputtering-chambers. Further on one will need solid-liquid cells with thermalisation, cools for spin echo methods. This means that there has to be a lot of space around the sample position available, and a flexible but reliable way of mounting all these items.

## 1.3    instrument performance

The accessibility of small sample sizes down to the $1\,mm^2$ range was chosen as the leading design criterion for the reflectometer proposed here. Concentrating on small samples opens the possibility to use focusing optics for beam transport and beam shaping. The essentially new feature of the proposed reflectometer is the truly focusing (*Selene*-type) guide system. The secondary instrument, i.e. sample stage and environment, spin analysis and detector are *conventional*.

The need to reach high $q_z$ and thus high detector angles favours a horizontal scattering geometry. This is also supported by the fact that than gravity affects the beam profile and divergence only in the sample plane. The only restriction caused by the vertical sample plane is that liquid/gas and liquid/liquid interfaces can not be studied, and that sedimentation in liquid/solid cells might cause problems. But exactly these applications are the aim of the other reflectometer.

The expected performance of the proposed reflectometer are

- maximum illuminated sample width 10 mm;

- minimum sample surface $1\,mm^2$;

- fulfilling the standard repertoire of time-of-flight reflectometers without compromises, e.g. specular and in-plain off-specular reflectometry;

- new operation modes are possible, e.g. with selectable constant resolution, or enabling high-speed specular reflectivity measurements by accepting a complex resolution function and a possibly higher background;

---

[7]provided by Peter Böni, Technical University Munich, Germany

- for sample environment and add-ons like spin echo equipment there are several meters of free space around the sample position without compromising on the performance;

- the scattering geometry is horizontal, leading to restrictions or even exclusion for certain soft-matter experiments, but allowing for high $q_z$ and a minor influence of gravity;

- a clearly defined beam footprint is possible and enables the concentration on a certain area on the sample, thus e.g. allowing for scanning the sample;

- optical elements can be used to obtain e.g. a parallel beam for GISANS experiments;

- in cooperation with Robert Georgii and Wolfgang Häußler, both from the Technical University Munich, we investigate the possibility to have a MIEZE set-up as an add-on. [→2.10.4]

To our knowledge there exists no neutron reflectometer with focusing in the scattering plane. First studies with add-on optics to realise this were performed on Amor@PSI [20] and at J-Parc. A prototype of a full *Selene* guide was build within the project leading to this proposal.[21] The original idea to combine angle-dispersive and energy-dispersive operation modes go back to F. Ott.[22, 23]

## 1.4    overlap with the soft-matter reflectometer

The vast majority of present-days experiments would in principle be possible on both instruments, where the better choice depends on the suited resolution, polarisation (and analysis), sample size, and compatibility with sample environments and add-ons. Still, the expected cutting-edge science in both fields requires the mutually excluding design criteria leading to the two reflectometers.

Since soft-matter samples often can be produced with surface area of $10\,\mathrm{cm}^2$ to $100\,\mathrm{cm}^2$ they would profit from a footprint larger than $\approx 1\times 5\,\mathrm{cm}^2$, which is about the upper limit for the proposed instrument still giving a well defined resolution and footprint. Completely excluded are measurements on gas/liquid or liquid/liquid interfaces due to the horizontal scattering geometry. These experiments and the related design criteria form the key drivers for the other reflectometer to be build at the ESS. That one will also be able to profit from larger sample sizes.

Besides these constrictions the proposed instrument can be used for typical soft-matter measurements as well — in some cases even opening up new possibilities: Measuring over a large sample size implies averaging over the whole surface area and thus details from inhomogeneities are completely lost. Focusing on very small surface areas ($\approx 1\,\mathrm{mm}^2$) will enable scanning the samples as it will be able to look at inhomogeneities within the sample plane with high detailed structure in the direction perpendicular to the interface. Thus, this reflectometer can be though as a neutron profilometer that probes the density profile perpendicular to the interface on a mm scale, rather than just its outer morphology.

Also the power of the *Selene*-type reflectometer relies on the high intensity of its focusing concept. It implies that it will be able to measure in the sub-second time scale. The increase of diffuse scattering due to the much higher divergence in this mode is at least partially compensated for by the reduced sample size.

One essential requirement for the soft matter reflectometer is to cover a huge $q_z$ range without moving the sample. This results in a short instrument using a broad λ range, and most likely only moderate to low resolution. The proposed instrument selects a smaller λ-range, starting at higher λ so that it optimally uses the flux. An other consequence is the higher intrinsic resolution.

## 1.5    user community, existing facilities

Neutron investigation techniques, namely neutron reflectometry, allows the destruction free investigation of even very sensitive materials (such as soft condensed matter materials, biological specimen and tissues). Some 35 dedicated neutron reflectometer instruments are available worldwide at about 15 neutron sources (nuclear research reactors as well as spallation sources) for scientific purposes and user operations covering a wide $q$-range for the investigations. There exist some more neutron reflectometers for e.g. neutron optics testing or industrial applications.

One can roughly subdivide the existing neutron reflectometers into two types, one with horizontal scattering plane and another with vertical scattering plane. The latter ones are capable of measuring solid/liquid, liquid/liquid and liquid/air interfaces also, these reflectometers are often specially designed for investigation with

biological samples and self-organising soft matter molecules. The reflectometers with horizontal scattering planes are widely used for investigations in the branch of hard condensed matter, magnetism and superconducting materials, in almost all cases probing solid/solid interfaces.

While the available neutron reflectometers at smaller sources are often designed as multi-purpose devices with vertical scattering geometry, larger facilities (such as ORNL, ILL, ISIS or FRM II) usually house more than one reflectometer, and there exist often the combination of a dedicated soft matter (vertical scattering plane) reflectometer, and a hard condensed matter (horizontal scattering plane) reflectometer in addition, to optimally exploit the appropriate $q$-ranges for the respective investigations.

The typical user request for beam time is much larger than the capacity of the existing reflectometers, typical overload factors range from 1.35 (EROS, Saclay) up to 2.2 (FIGARO, ILL). Depending on the instrument dedication, there is a growing demand for e.g. investigations at the air/water interface. Typical load factors for this type of reflectometry measurements at dedicated instruments range from 6% (REFSANS, FRM II) to 60% (FIGARO, ILL).

## 1.6 infrastructure & support facilities

The sample environment needed to cover the standard applications contains cryomagnets (state-of-the-art are $7\,T$, asymetric field), cryostats, Helmholtz coils (for lower fields, often combined with a closed-cycle refrigerator), and in-situ furnaces. More specialised equipment as liquid/solid cells often is provided by the users. For these a device for thermalisation should be present at the instrument. A furnace for off-situ annealing, a glove box, and a fridge for sample storage should be accessible.

For sample preparation a chemistry lab should be located not too far away. This in mainly needed by the soft-matter community, but it might also serve e.g. for (HF−) etching a substrate prior to in-situ growth studies.

For non-standard experiments like the in-situ growth studies, the equipment most likely will be provided by the users. But they still need supply of power, gases ($N_2, Ar, He$) and cooling (water).

It proved to be very helpful at PSI to have direct access to a small workshop in the experimental hall (also as a user), and to mechanical support on short notice. E.g. to modify or build adapter plates or sample holders.

# 2   Description of Instrument Concept and Performance

[10 pages] [Describe the instrument concept and evaluate its expected performance using relevant performance indicators (as defined for the instrument class by the corresponding STAP). Explain how the concept addresses the scientific drivers described above. Justify how the concept makes use of the ESS long-pulse structure.]
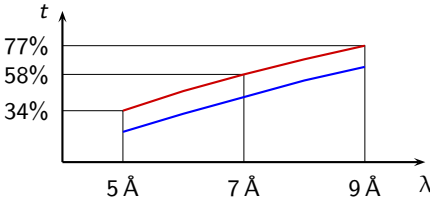
It is proposed to build a polarising reflectometer, optimised for samples of $1\,\text{cm}^2$ area, or less, capable to cover a wide $q_z$ range with variable resolution. The scattering plane is horizontal to allow for wide detector angles. The unique feature of this instrument is its truly focusing guide system, which reduces background and illumination of sample environment, and which opens new possibilities for beam shaping and filtering.

In the following the lay-out of the instrument is presented, followed by a presentation of the guide system and its key features. These strongly influence the design of the components presented thereafter. The essential parameters of the instrument are given in table 2.1.

The final sections of this chapter deal with the operation schemes [→2.10], simulations [→2.11], and a discussion of the performance [→2.12].

Table 2.1: Key features of the reflectometer for small samples.

| parameter space | | |
|---|---|---|
| $q_z$-range | $[0, 1]\,\text{Å}^{-1}$ | to be covered in 5 measurements |
| λ-range | $[5, 9.4]\,\text{Å}$ | |
| sample size | $[0.3, 50] \times [0.3, 10]\,\text{mm}^2$ | $x \times y$ |
| maximum divergence | $\Delta\theta_{xy} = 1.5°$ | scattering plane |
| | $\Delta\theta_{xz} = 1.5°$ | sample plane |
| resolution | | |
| intrinsic $\Delta\lambda/\lambda$ | 2.1% | $5.0\,\text{Å}$ |
| | 4.0% | $9.4\,\text{Å}$ |
| $\Delta q/q = \text{constant}$ | 3%, 5%, 10%, … | with multilayer monochromator |
| geometry | | |
| scattering plane | horizontal | |
| total length | $58.0\,\text{m}$ | |
| sample / detector | $6.2\,\text{m}$ | |
| 2θ | $-2°$ to $50°$ $(110°)$ | for $q_z \leq 1\,\text{Å}^{-1}$ $(2\,\text{Å}^{-1})$ |
| moderator | cold | |

guide transmission

| λ | t | |
|---|---|---|
| $5\,\text{Å}$ | 34% | 20% |
| $6\,\text{Å}$ | 47% | 32% |
| $7\,\text{Å}$ | 58% | 43% |
| $8\,\text{Å}$ | 68% | 54% |
| $9\,\text{Å}$ | 77% | 63% |

analytical, based on eqn. 6.5.2

McStas simulations

## 2.1 instrument lay-out

The principle instrument lay-out is shown in figure 2.1. The various components are briefly presented here. A more detailed discussion follows in the next sections.
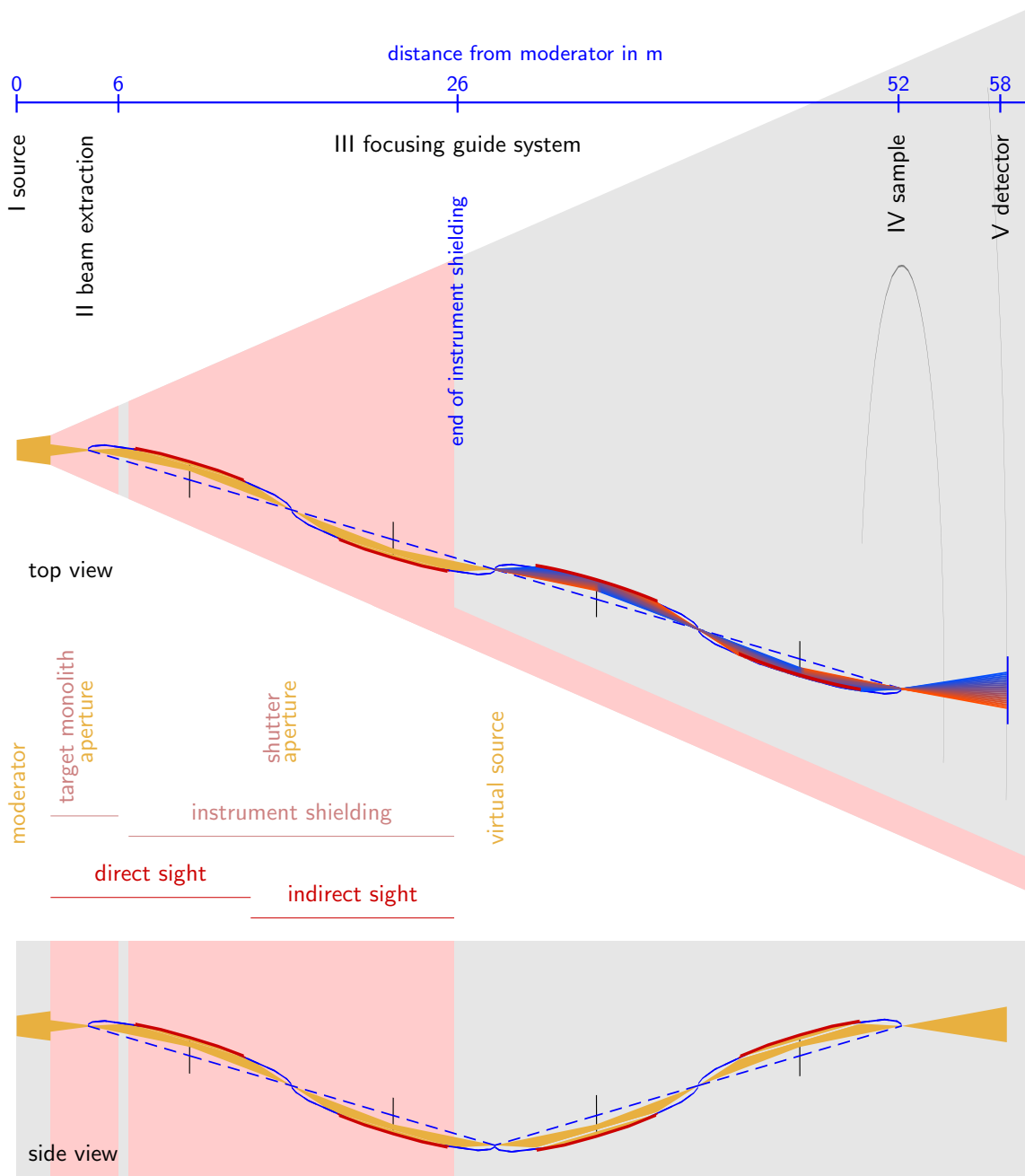


Figure 2.1: Sketch of the instrument lay-out. The direction normal to the beam is stretched by a factor 10 for clarity. The gray area in the upper sketch represents a 5° wedge on the floor. The detector will move outside this area for high angles. The light red area represent shielding, i.e the target monolith, the common instrument shielding and individual instrument shielding. The thick red lines represent the *Selene* guide segments, where the blue lines give the shapes and the long axis of the related ellipses. The golden area are the beam paths within the extraction unit and the first *Selene* guide section. For the second section the λ-θ encoding mode is shown, where the λ is here encoded in a colour reaching from red to blue. (For the nomenclature of the components, please refer to table 5.1.)

**I source** The instrument needs a cold moderator as neutron source, where the effective flux maximum (i.e. including losses and rescaling [→2.5.1]) determines the minimum wavelength $\lambda_{min}$.

**II beam extraction** [→2.3] The purposes of the beam extraction unit are to form a pin-hole at $x = 4.2$ m of $10 \times 10$ mm$^2$, and otherwise to stop as many fast neutrons and $\gamma$ radiation as possible.

**III focusing guide system** [→2.2] The essential difference of the presented instrument compared to conventional reflectometers is the truly focusing guide system.

Between the pin-hole forming a virtual source, and the sample a focusing guide system is realised, based on the *Selene* concept. The complete guide consists of 4 segments, each a 7.2 m long elliptically shaped reflector where the focal point distance is 12 m. The usage of 4 instead of 2 longer segments allows to get out of line of sight twice at $x \approx 25$ m, and to use the mentioned pin-hole in the extraction unit.

The first 2 segments create an image of the pin-hole in the mid of the guide ($x = 28.2$ m, in the following referred to as *virtual source*), where precision beam-shaping and $\lambda$- and polarisation filtering is then performed. The last 2 segments focus the clean beam to the sample.

Additional beam-defining elements like slits, choppers, polarisers, and monochromators, can be located in the spaces at $x \in [25.8, 30.6]$ m, $x \in [25.8, 42.6]$ m, and $x \in [49.8, 52.2]$ m.

**IV sample** [→2.7] The sample is located at the final focal point at $x = 52.2$ m. The *Selene* guide ends 2.4 m upstream the sample position. This and the focused beam (making a nearby slit obsolete) allow for installing voluminous sample environment.

**V detector** [→2.9] A position sensitive detector is located at $x = 58$ m, where its angular resolution dominates the resolution of this instrument concept. For diffraction a second, shorter detector arm allowing for higher $2\theta$ can be installed.

## 2.2 Selene guide

**task: deliver a focused beam to the sample with adjustable divergence and footprint**

Since the *Selene* guide dominates the complete instrument lay out, it is presented first. Special aspects discussed in the appendix are: design considerations [→6.1], coma aberration [→6.3], and chromatic aberration due to gravity [→6.4].

The reason for using a truly focusing guide is that it allows for shaping the phase space required at the sample already at the guide entrance. This has the consequence that radiation issues and illumination of the sample environment are strongly reduced. It is important to notice that most other guide concepts based on elliptic guides are not exactly focusing: They suffer from strong coma aberration effects and create a divergent beam at the exit. [24, 25]

The *Selene* guide can be seen as an extended Montel optic as used at synchrotron beam-lines. Two planar-elliptic reflectors form a gorge with L-shaped cross section. The distance of the guide entrance to the virtual source at the initial focal point is chosen in a way to avoid multiple reflections for each reflector. The first guide segment creates an image at its second focal point which is blurred due to coma aberration. To correct for this, an identical guide segment is used, mounted parallel to the first one, but reflecting in the opposite direction. This inverts the coma effect and re-establishes the image of the virtual source at the final focal point. A sketch of the guide geometry is shown in figure 2.2
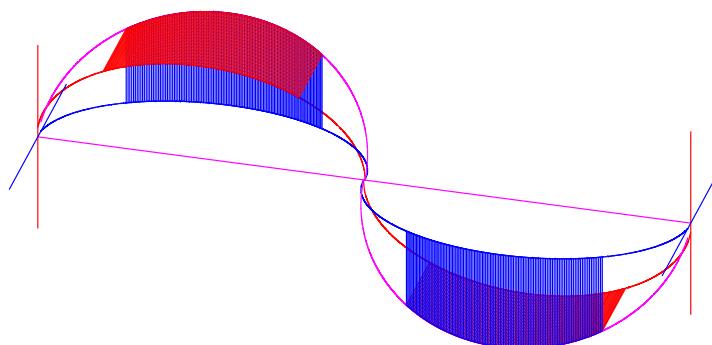


Figure 2.2: Sketch to illustrate the shape of the *Selene* guide. Shown are two segments with L-shaped cross section, sharing the long axis (magenta) and a focal point.

Table 2.2: Parameters of the *Selene*-type guide. For a given instrument length of 58 m and $\Delta\theta_{xy} = \Delta\theta_{xz} = 1.5°$ the following guide parameters are obtained by analytical calculations. [→6.1]

| | | |
|---|---|---|
| **guide parameters** | | |
| $c$ | 6.0 m | half distance between focal points |
| $\xi$ | 0.6 | effective length of the build guide |
| $b/a$ | 0.01754 | $\Rightarrow \quad b = 105.26$ mm, $\quad a = 6000.92$ mm |
| **distances** | | |
| moderator / pin hole | 4.2 m | first focal point |
| $2c$ | 12.0 m | length of ellipses |
| $\xi \cdot 2c$ | 7.2 m | length of (coated) guide sections |
| $(1-\xi) \cdot 2c$ | 4.8 m | space between guides |
| $(1-\xi) \cdot c$ | 2.4 m | space before sample |
| sample / detector | [1.5 ... 7.5] m | high-angle diffraction vs. high resolution |
| $\Delta z$ at sample | 0 / 522.7 mm | vertical offset of one *Selene* section |
| $\Delta y$ at sample | 0 / 522.7 mm | horizontal offset of one *Selene* section |
| **free space withing flight-path for beam- / pulse-shaping (distance from the moderator)** | | |
| $x =$ 6.0 m → 6.6 m | | gap behind target monolith |
| 13.8 m → 18.6 m | | eventually frame-overlap chopper |
| 25.8 m → 30.6 m | | precise beam-shaping, polarisation |
| 37.8 m → 42.6 m | | |
| 49.8 m → 52.2 m | | before sample |
| **coating** | | |
| $m$ | 3.0 | critical edge |
| coated area | 4 m$^2$ | |
| material | Ni/Tisupermirror | |

The guide system for the presented reflectometer consist of two such *Selene* guide sections: The first has to create a virtual source with defined size and divergence, but twice out of line-of-sight from the moderator. This virtual source is in a low-radiation region so that sensitive mechanical equipment and optics can be used there. It is also possible to access this area for maintenance during operation (with the instrument shutter closed). At and around the virtual source point the beam is shaped according to the needs on the sample. The shape and orientation of the footprint of the beam on the sample can be defined by an adequate slit system. The second *Selene* guide has to map the shaped beam to the sample. The divergence (and eventually the incident angle) of the beam are defined by slits before or after the guide segments. This way spot-size and divergence are adjusted independently.

The use of two *Selene* guides has the consequence that each neutron is reflected exactly 8 times before it arrives at the sample. The resulting reduction in intensity is the price one has to pay for low radiation and convenient beam manipulation. [→2.5.1]

Table 2.2 gives the geometrical parameters of the ellipses, the measures of the guide and the coating.

## 2.3    beam extraction

**task: transport the requested phase space volume outside the target monolith, while reducing the radiation as much as possible**

Within the first 6 m the only *optics* needed is a pin-hole at $x = 4.2$ m acting as a virtual source for the first *Selene* guide section. The location is chosen to accept the required divergence of $\Delta\theta = 1.5°$ from the $120 \times 120$ mm$^2$ wide moderator. The extraction insert consists of some highly $\gamma$ and neutron absorbing material (e.g. copper).

There is no restriction for including a maintenance shutter in the monolith or in the extraction insert at any position.
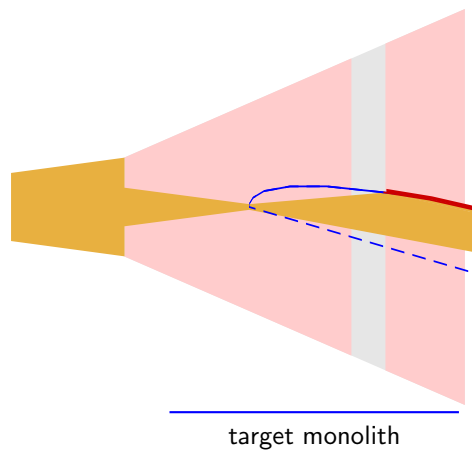
Figure 2.3: Sketch of the beam extraction section with a pin hole. A small ($10 \times 10\,\mathrm{mm}^2$) aperture 4.2 m from the source acts as virtual source and defines the initial focal point for the first *Selene* guide section. This position allows for a divergence of $\Delta\theta_{xy} = \Delta\theta_{xz} = 1.5°$. The openings of the flight path section are 68 mm / 58 mm at the entrance / exit of the target monolith.

target monolith

## 2.4    shielding

It is inherent to the *Selene* guide concept that neutrons are reflected on each reflector once, so that a shielding behind the first guide segment can stop all transmitted neutrons. An absorber opposing the centre of the reflector blocks all direct trajectories from the pin-hole to a space behind the first guide segment. The second guide segment repeats this scheme so that at the end of the shielding around and behind the first *Selene* guide section the view to the moderator is blocked twice, as is required by the ESS [→8.2]. There is space for a vacuum housing and mounting equipment around the guide. The guides' open construction (it forms an L, rather than a rectangle) allows for a tight shielding on two sides, the support mechanics can be mounted on the other sides.

Figure 2.4 shows the shielding concept for the first *Selene* guide section including the target monolith. Behind the monolith there is a gap of 600 mm until the first guide starts. Unless used for filters or a shutter, this gap can be filled by an extension of the insert.

The first and second guide elements ares enclosed in a heavy concrete block. In the sketch at least 50 mm free space between guide and shielding are assumed for support, alignment devices, and vacuum housing. Because the dimensions of the openings are about 3 times the actual guide width, additional shielding is needed before and after the concrete shielding. These masks are supposed to consist of copper (displayed in blue). The area directly irradiated from target and moderator ends at the exit of the first concrete block at $x = 13\,800$ mm. The indirectly irradiated area ends at $x = 25\,800$ mm, i.e. less than half way between source and detector. In the gap $x \in [14, 18]$ m optical elements, the instrument shutter and eventually a frame overlap chopper can be installed, again surrounded by a concrete shielding.

The support system for the guides needs more space than just the $160 \times 160\,\mathrm{mm}^2$ within the channel. Swiss-Neutronics suggested to use a granite beam to support the guide. This could also be part of the shielding, with appropriate shape to prevent straight holes parallel to the channel. If granite is suited for this purpose has to be investigated. On the other side one could use a heavy concrete beam as support, if it is stable enough also against thermal influences.

The second *Selene* guide section will need some shielding, too, but since neither thermal or fast neutrons, nor $\gamma$-radiation should reach this region, only a moderate boron-based absorber should be sufficient. To ensure the absence of fast neutrons, a sapphire filter can be inserted behind the concrete shielding.

### 2.4.1    MCNPX simulations

Based on the model given in figure 2.4 MCNPX simulations have been performed by U. Filges, PSI. The results are summarised in table 2.3. These tell that the proposed geometry and dimension of the *Selene* guide allows for a shielding which fulfils the requirements by the ESS. Just outside direct line of sight the dose rate is $37\,\mu\mathrm{Svh}^{-1}$, and it trops below the computational threshold at the end of the shielding. The simulations took 7 days on a cluster with $7 \times 24$ cores.

### 2.4.2    shutter

An instrument shutter can be placed in the gap between the first and the second guide segments. This region is already out of line of sight from the moderator, so that only secondary radiation and cold neutrons transported by the guide have to be blocked.
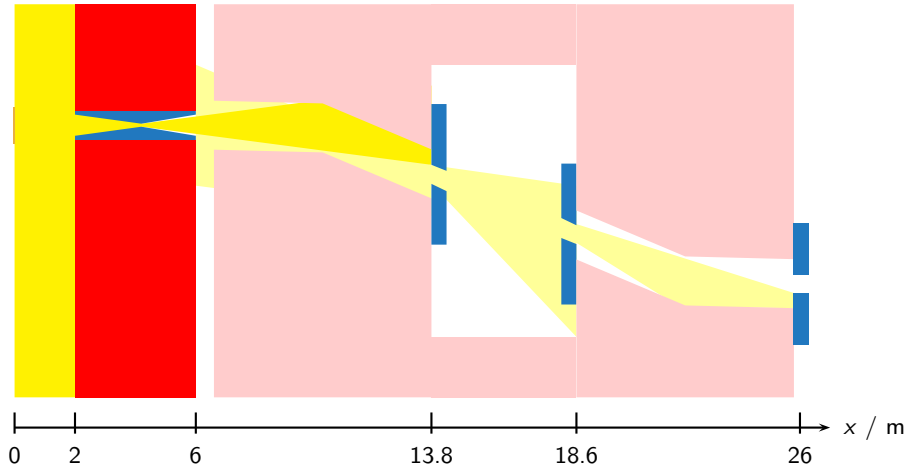
Figure 2.4: Sketch of the fast neutron and γ shielding concept. Here a vertical cut through the shielding is shown, following the beam in horizontal direction. The guide geometry and thus the shielding is the same horizontally and vertically. The source (moderator) is represented by the brown rectangle on the left. The red area stands for the monolith, the blue insert is the extraction unit. The pale red area represent heavy concrete shielding (or a sandwich of various moderators and absorbers), which hosts the guide elements. Additional masks (here blue) are needed to block the opening outside the neutron beam path. The area directly illuminated from the source is shaded yellow, the indirectly illuminated area is pale yellow. The neutron guides are not shown.

| position | $x\,/\,\mathrm{m}$ | $y/z$ position | dose rate / $\mu\mathrm{Sv\,h}^{-1}$ | | flux / $\mathrm{s}^{-1}\mathrm{cm}^{-2}$ | error |
|---|---|---|---|---|---|---|
| | | | $\gamma$ | neutron | neutron | |
| exit common shielding | 14.5 | in beam | 37 | 78 000 | $9.3 \cdot 10^4$ | 7% |
| | | off beam | 37 | 10 000 | $1.6 \cdot 10^4$ | 7% |
| entry instrument shielding | 18.1 | | 8 | 1 400 | $2.5 \cdot 10^3$ | 20% |
| exit instrument shielding | 26.5 | in beam | — | — | — | — |
| | | off beam | — | — | — | — |
| 5 m behind shielding | 31.5 | in beam | — | — | — | — |

Table 2.3: Dose rates and flux calculated with MCNPX for various positions along the guide. The source was assumed to be continious with a power of 5 MW. I.e. the peak dose and flux are a factor 30 higher. The computational statistics was too low for the positions marked with —.

## 2.5    energy- and time range

The time and energy characteristics of the ESS long-pulse source allows for a relatively wide λ range, while keeping the intrinsic instrument resolution below ≈ 4%, and avoiding the proton pulse time for measurements. A full reflectivity curve is thus achieved by piecing together (a few) measurements with varying ω, only. Further stitching due to complex chopped beam characteristics is not necessary.

### 2.5.1    flux and $\lambda_{\mathrm{min}}$

The experience with existing TOF reflectometers is, that the lower limit of the wavelength spectrum $\lambda_{\mathrm{min}}$ corresponds to the effective flux maximum at the sample position. The reason is that even smaller λ result in higher $q_z$ and thus in general in lower reflectivity, and at the same time in a lower incident intensity. Thus the accuracy of the data rapidly decreases and it is much more appropriate to measure at a higher angle of incidence to access the corresponding $q_z$ range.[1]

The effective flux at the sample can be estimated by reducing the initial flux $I_0(\lambda)$ by the losses due to reflections on the guide walls, and by taking into account that in the end one aims for $\Delta q/q = $ constant or something quite close.

---

[1]In case the width of the $q_z$-range covered within one pulse is essential, one might accept also a smaller $\lambda_{\mathrm{min}}$ for the cost of a dramatically increased measurement time.
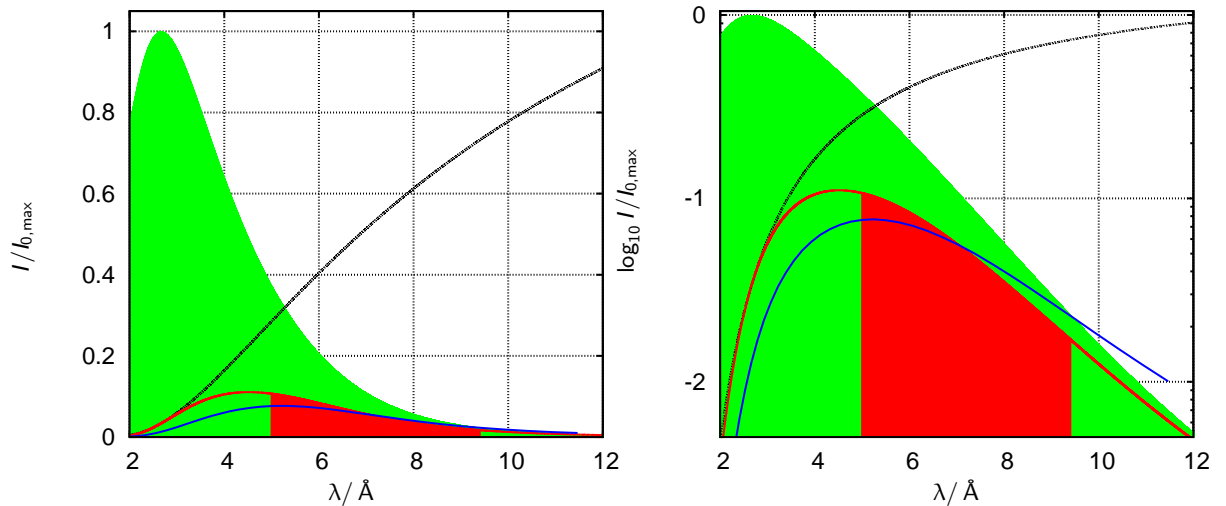
Figure 2.5: Spectra $I(\lambda)/I_0$ (left) and $\log_{10} I(\lambda)/I_0$ (right) as given by the source (green area), after attenuation according to eqn. (6.5.2) with 8 reflections (red line), and after re-binning it to $\Delta\lambda/\lambda = 2\%$ (blue line). The latter line is scaled by an arbitrary value. The black line is the transmission of the guide. The source spectrum $I_0(\lambda)$ is the one used by the McStas component ESS_moderator_long. The red area represents the neutrons actually arriving at the sample.

The double *Selene* guide concept involves 8 reflections for all neutrons on surfaces with a non-perfect reflectivity $R$. Since the angle of incidence on the guide surface hardly varies along the guide for the presented concept, one can assume an attenuation of [→6.5] $I(\lambda) \approx I_0(\lambda) \cdot R(\lambda)^8$.

A more prominent effect has the required $\Delta q/q = $ constant: effectively the time-bins, and thus the $\lambda$-bins necessary for $R(q_z)$ curves follow $\Delta\lambda/\lambda = $ const which shifts the spectral wight to the bins with large $\lambda$. This shift can be approximated by $I(\lambda)_{\Delta\lambda/\lambda = \text{const}} \propto \lambda \cdot I(\lambda)_{\Delta\lambda = \text{const}}$

This way the minimum wavelength $\lambda_{\min} = 5$ Å was determined as illustrated in figure 2.5.

### 2.5.2    time regime and $\lambda_{\max}$

In order to avoid a contamination of the measurement with background originating from the proton pulse and secondary processes, the instruments length was chosen so that the 5 Å neutrons arrive at the detector right after a pulse. This leads to a minimum length (moderator to detector) of 58 m. And the time between pulses sets the upper wavelength limit to $\lambda_{\max} = 9.4$ Å. Figure 2.6 shows the corresponding $t$-$x$-diagram.

If positioned at or before the virtual source, the monitor is also not affected by the background originating from the pulse.
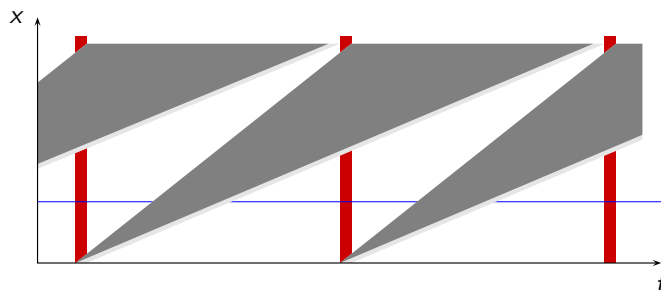


Figure 2.6: Sketch to illustrate how to avoid the influence of the $\gamma$ and fast neutron burst from the proton pulse hitting the target. The sketch is to scale with period $T = 70$ ms, pulse length $t = 3$ ms, and a sample detector distance of 58 m, i.e. $\lambda \in [5, 9.4]$ Å.

### 2.5.3    intrinsic $\lambda$ resolution

The time- and thus the $\lambda$-resolution is $\Delta\lambda \approx 0.2$ Å, given by $\lambda \in [5, 9.4]$ Å, the moderator-detector distance of $X = 58$ m, and the pulse length $\tau$. [→8.3.1] This leads to $\Delta\lambda/\lambda = 2.1\%$ at $\lambda = 9.4$ Å, and $\Delta\lambda/\lambda = 4.0\%$ at $\lambda = 5.0$ Å.

### 2.5.4 frame-overlap suppression

For neutrons with $\lambda < \lambda_{\min} = 5\,\text{Å}$ the coating of the guide acts as a filter. If necessary a Be-filter can be used to further suppress the range $\lambda < 4\,\text{Å}$.

Neutrons with $\lambda > \lambda_{\max} = 9.4\,\text{Å}$ will be suppressed by using a transmission filter. A silicon wafer with a Ni coating ($m = 1$) shaped like a logarithmic spiral [$\rightarrow$7.1] is installed before the virtual source. The shape assures that all trajectories pointing towards the virtual source hit the wafer at the same angle (here $0.95°$).

### 2.5.5 choppers

For this instrument and the operation schemes presented in section 2.10 no choppers are foreseen.

In case the frame-overlap suppression as described in 2.5.4 proves to be insufficient, it is possible to add a frame-overlap chopper later on close to the focal point at $x = 16.2\,\text{m}$ (blue line in figure 2.6). There the beam cross section is of the order $30 \times 30\,\text{mm}^2$. This leads to relaxed specifications for the chopper. Neglecting opening times for a first approximation the chopper should be open for $t \in [0.020, 0.040]\,\text{s}$ (for $\lambda \in [5, 9.4]\,\text{Å}$). The next higher order is transmitted for $t \in [0.090, 0.110]\,\text{s}$ and corresponds to $\lambda \in [22, 27]\,\text{Å}$.

For the moment, no chopper is foreseen there and the $\lambda$ filtering is meant to be realised with a reflecting mirror [$\rightarrow$7.1].

Since the *Selene* guide system in the end fulfils the same task as a *normal* guide, it can be combined with multi-chopper setups for Repetition Rate Multiplication or for Wavelength Frame Multiplication [26]. In the large free regions between the guide segments of the *Selene* guide this would not cause any modifications to the guide. A chopper within the reflecting part results in gap in the divergence distribution.

## 2.6 polarisation

Neutron spin polarisation and its analysis are key-features of the reflectometer for small samples. Based on the demands nowadays one can estimate at least 50% of the measurements will need a polarised beam, and at least 10% also polarisation analysis.

The concepts presented below are either well established, or under development so that there is no unknown risk connected. Besides for the permanent coating, the options can be altered later on.

### 2.6.1 permanent polarisation

A permanent polarisation can be achieved using an appropriate coating on (one side of) one guide segment. This has the advantages that off-specular scattering from the coating will not hit the sample, and that the distance from a high magnetic field at the sample position is sufficiently large to prevent depolarisation.

### 2.6.2 optional polarisation

In case the 50% loss due to polarisation is not accepted, there are several approaches possible:

**polarising (double bounce) reflector**      The ML monochromator used for $\lambda$-$\theta$ encoding or any reflector close to the initial focal point can have a polarising coating.

**polarising filter**      By using a transmission filter with the shape of a logarithmic spiral as discussed in section 7.1 it is possible to polarise a divergent beam emerging form a small source with a moderate $m$ of the SM coating (and thus a high polarisation efficiency).

E.g. a combined $\lambda$ low-pass and polariser for $\lambda \in [5, 10]\,\text{Å}$, $\Delta\theta = 1.5°$, and a distance of the polariser from the focal point of $300\,\text{mm}$ leads to a device of $\approx 1\,\text{m}$ length. The polarising coating has $m = 2$.

**$^3$He polariser**      The small beam size close to the initial (intermediate) focal point allows for the operation of a rather small $^3$He cell. Typically with a cross section of a few $\text{cm}^2$, only. In addition, the long distance from this point to the sample avoids depolarisation due to high magnetic fields, there.

### 2.6.3 analyser

The different beam geometry behind the sample demands for more complex and larger devices.

**analysing filter**      This is the analogue to the polarising filter, but it is not realistic to install it some $300\,\text{mm}$ behind the sample. Thus a larger multi-channel device directly in front of the detector has to be build. This is a new concept and has not been tested, yet.

**wide-angle analyser based on supermirrors**    A SM-based multi-channel bender can be installed directly in front of the detector. Similar devices are in operation at FOCUS@PSI and at HYSPEC@SNS.

[3]**He analyser**    The wide divergence and the needed distance from the sample (to avoid the influence of the sample magnetic field) mean that a large [3]He is needed.

### 2.6.4    flipper

**RF flipper**    The divergent polychromatic beam can be flipped by using a RF flipper.

**RSF flipper**    An alternative approach for monochromatic beams changing the wavelength with time is a Resonance Spin Flipper [27].

**switchable remanent coating**    For the devices based on SM coatings for polarisation / analysis one can use magnetically remanent coatings, allowing for flipping the polariser, rather than the beam.[28]

## 2.7    sample stage

The sample stage is the same as for conventional reflectometers. It either uses a hexapod or a classical tower of translation- rotation-, and tilting-stages.

The position of the stage on the floor might vary with the alignment and the operation mode of the instrument. I.e. a $x$-$y$ translation stage (or a platform on air-pads) forms the basis.

Since the sample environment can be quite heavy and voluminous, the sample stage should be able to handle wights of up to 1 t. The *free* space between the platform and the sample should be at least of the order of 300 mm. In table 9.1 a possible set-up of translation and rotation devices is listed. The complete sample stage should be non-magnetic, because one principle application of this instrument will be the measurements in high magnetic fields.

The guide ending 2.4 m before the sample leaves enough space for a fast slit system [→2.8.3] and even large sample environmental devices like troughs or cryomagnets. Also an equipment for complementary measurements like UV, or X-ray will find space.

## 2.8    beam shaping

### 2.8.1    beam definition

The beam shape at the sample position is essentially defined in between the two *Selene* guide sections, 24 m upstream. The symmetry of the problem tells that the same degree of freedom will be needed there as at the sample stage [→2.7], but with a much reduced demand concerning load.

Since the focal point position does only change due to misalignment of the first *Selene* guide section, the base-$x$-$y$ translation needs to cover only a small area, only.

### 2.8.2    apertures within guides

To block the direct line of sight through the *Selene* guide and to reduce the divergence, one-sided apertures are positioned close to the centres of the 2nd guide segment for both guide sections. The one in the first guide is rather heavy, but does not need to be very accurate, since it should just reduce the radiation level outside the shielding. The apertures in the second guide will be used for precise beam divergence definition and thus need to be very accurate. On the other side, the blades are much thinner and thus lighter.

### 2.8.3    fast aperture

Behind the *Selene* guides, some 2.2 m before the sample a precise and fast slit system might be used optionally. For the conventional operation mode it defines the angle of incidence and the divergence. *Fast* here means that position and opening of the slit can be varied between pulses within 10 ms.

If technically possible it could also be used in the λ-θ encoding mode, to cut down the unwanted off-specular intensity from the monochromator by scanning the slit across the beam during one pulse.

## 2.9    detector

### 2.9.1    area detector

For the reflectometry measurements one position sensitive detector is needed. The technology available today ($2\,mm$ resolution, area $400 \times 400\,mm^2$) would work. But higher resolution and a wider area would improve the instruments performance. In principle the instrument could be upgraded with a *better* detector once it is available without affecting the rest of the instrument. There is no preference for any detector technology from our side. Table 2.4 gives the (realistic) wish-list of the detector properties. [→9.2]

|                       | state-of-the-art | ideal parameters |
|-----------------------|------------------|------------------|
| size                  | $400 \times 400\,mm^2$ | $500 \times 170\,mm^2$ |
| resolution horizontal | $2\,mm$          | $< 0.5\,mm$      |
| resolution vertical   | $2\,mm$          | $2\,mm$          |
| rate at $5\,Å$        |                  | $5 \cdot 10^8\,s^{-1}Å^{-1}$ |
| rate at $9.4\,Å$      |                  | $2 \cdot 10^8\,s^{-1}Å^{-1}$ |

Table 2.4: Key parameters for the area detector. The numbers of the state-of-the-art detector were given by R. Hall-Wilton, ESS.

### 2.9.2    single detector

For diffraction measurements on the films or the substrates a second (single) detector on a shorter 2θ arm might be used. This possibility proved to be useful e.g. to check possible bending or twinning upon cooling.

### 2.9.3    CCD camera

To align the guide and monitor its performance, and for aligning the sample a CCD camera in front of the area detector can be used. This has the advantage that the resolution is much higher, while its draw-backs of high noise and low efficiency do not play a role for this purpose.

The active area should be some $150 \times 150\,mm^2$, the resolution about $0.1 \times 0.1\,mm^2$.

## 2.10    operation modes

In figure 2.7 the three principle operation modes are sketched, and the corresponding λ-θ detector diagrams are shown. A short description is given below, and an extensive discussion including data acquisition and reduction is given in the appendix [→10].



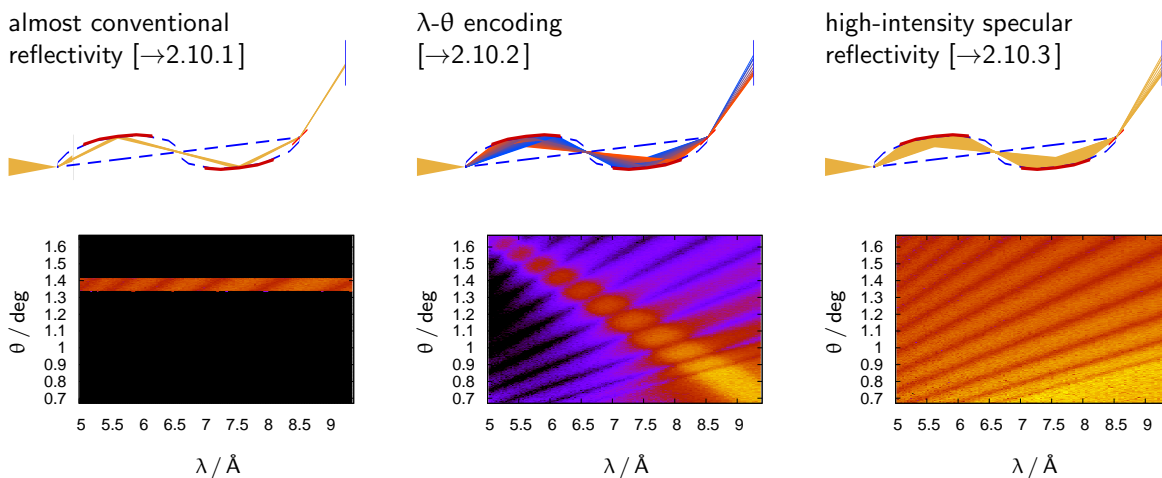Figure 2.7: Operation schemes and $I(θ, λ)$ maps obtained by simulation assuming a $1000\,Å$ thick Ni film on glass as sample: using a slit before the sample, using a multilayer monochromator for angle-wavelength encoding, and using full divergence and pulse.

### 2.10.1     almost conventional & off-specular reflectivity

[→10.1] Though still giving a convergent beam to the sample, this mode is quite close to the operation scheme of conventional TOF reflectometers. An aperture 2.2 m before the sample defines the divergence $\Delta\theta$, the wavelength is obtained by the time-of-flight, and $\theta$ is adjusted by rocking the sample. The $\lambda$ resolution is given by the pulse length and varies from 2.2% (9.4 Å) to 4% (5 Å).

Because of the disentanglement of beam spot size and divergence in the *Selene* guide, the footprint on the sample surface is defined by the aperture at $x = 28.2$ m. Over-illumination of the sample and illumination of the sample environment can be suppressed.

By moving the divergence-defining aperture within the divergence of the beam leaving the guide, one can change $\theta$ without tilting the sample.

Figure 2.8 shows intensity maps (left), and the reflectivity curve extracted therefrom (right). These data were obtained by simulation.
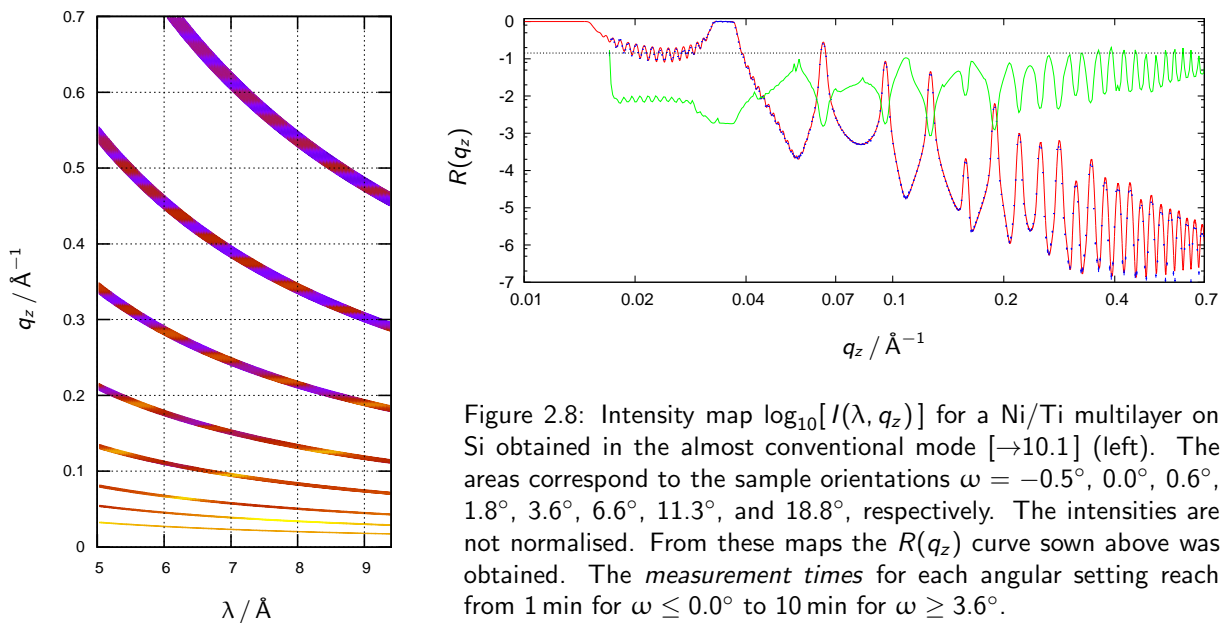


Figure 2.8: Intensity map $\log_{10}[I(\lambda, q_z)]$ for a Ni/Ti multilayer on Si obtained in the almost conventional mode [→10.1] (left). The areas correspond to the sample orientations $\omega = -0.5°$, $0.0°$, $0.6°$, $1.8°$, $3.6°$, $6.6°$, $11.3°$, and $18.8°$, respectively. The intensities are not normalised. From these maps the $R(q_z)$ curve sown above was obtained. The *measurement times* for each angular setting reach from 1 min for $\omega \leq 0.0°$ to 10 min for $\omega \geq 3.6°$.

This mode will be needed to align the sample, and for measuring (or discriminating) off-specular scattering.

**off-specular scattering**     In this mode off-specular scattering can be measured exactly in the same way as on conventional TOF reflectometers. Without using pulse shaping choppers the $q_z$ resolution is essentially given by $\Delta\lambda \propto \tau$. The $q_x$ resolution varies strongly as a function of $\lambda$ and $\theta_f$.

### 2.10.2     angle-energy encoding

[→10.2] Compared to the almost conventional mode there are two essential differences: It allows to cover a wider $q_z$ range in one shot by relating $\lambda_{max}$ to small $\theta$ and $\lambda_{min}$ to large $\theta$. And while $\lambda$ is encoded in $\theta$, it has the resolution $\Delta\lambda/\lambda = \Delta\theta/\theta$. This means that the resolution can be manipulated without pulse shaping, so no choppers are needed.

The encoding is achieved by using a (double bounce) multilayer monochromator before $x = 28.2$ m. To get a clean beam a fast slit system 2.2 m before the sample is necessary to scan $\theta$ within one pulse.

Figure 2.9 shows intensity maps obtained by simulation for this operation scheme.

This is the mode of choice if $\Delta q_z/q_z = 3\%, 5\%, \dots 20\%$, or a wide $q_z$ range are required.

**off-specular scattering**     Also in this mode off-specular scattering can be measured. Since the specular scattering occupies the diagonal of the $\lambda$-$\theta$ diagram, the off-specular *area* consist of tow triangles. The $q_z$ resolution is almost constant, the $q_x$ resolution varies strongly as a function of $\lambda$. Figure 2.10 compares the $q_x$-$q_z$ area covered by the almost conventional and the $\lambda$-$\theta$ encoding mode.
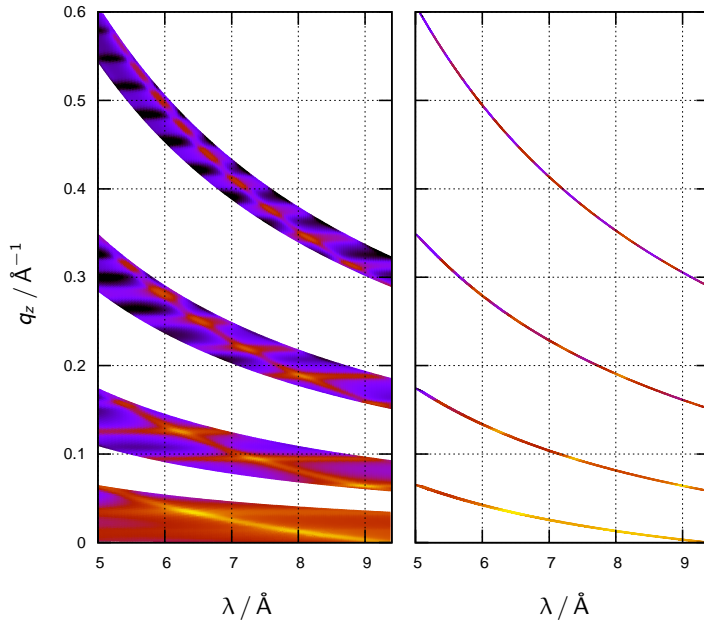
Figure 2.9: Intensity map $\log_{10}[\,I(\lambda, q_z)\,]$ for a Ni/Ti multilayer on Si obtained in the $\lambda/\theta$ encoding mode [→10.2]. The 4 areas correspond to the sample orientations $\omega = -0,5°$, $2°$, $6°$, and $12°$, respectively. The intensities are not normalised. The left maps shows the signal after transformation of $t$ to $\lambda$ and $\theta$ to $q_z$. In the maps on the right side the areas where only off-specular intensity is expected (assuming a perfect monochromator) are shaded.
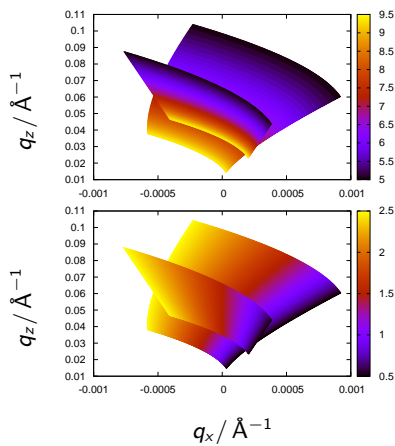


Figure 2.10: $q$-space covered by off-specular measurements in the $\lambda$-$\theta$ encoding mode (larger area) and in the almost conventional mode (smaller, more distorted area). In the top map $\lambda$ and in the bottom map $\theta$ is plotted as a function of $q_x$ and $q_z$. The detector was assumed to cover $\theta_f = 0.5°$ to $2.5°$, and $\theta_i = 1.5°$ in the conventional mode.

**accuracy**    In the $\lambda$-$\theta$ encoding mode it is essential that the angular error induced reduction of the $\lambda$ resolution is below the $\Delta\lambda/\lambda$ aimed for. The encoding is given by $\lambda = 4\pi \sin(\theta_s + \omega_m - \omega_s)/q_m$ with the coating of the monochromator having a Bragg peak at $q_m$, and the monochromator and sample angles $\omega_{m/s}$. An angular error $\Delta\alpha$ caused by a misaligned guide or by waviness leads to a wrong $\theta$ and thus to $\Delta\lambda \approx 4\pi \sin \Delta\alpha/q_m$. If the angular error is so large that the beam misses the sample, the error does not cause a reduction of the resolution, but it just leads to a reduction of the reflected intensity.

For a 10 mm long sample and $\omega_s = 10°$ the projected sample height is $\approx 2$ mm. This corresponds to angular errors of $0.006°$ to $0.025°$ along the last guide segment, and thus to $\Delta\lambda < 0.02$ Å. This can be neglected. So in most cases an imperfect guide will result in a reduced intensity on the detector (the dark lines seen with the prototype set-up), but the encoding is still valid.

### 2.10.3    high-intensity specular reflectometry

[→10.3] This is the operation mode which delivers the most flux to the sample. The full divergence and also the full wavelength band accepted by the instrument are used. The wavelength is encoded in the time of flight, and thus the resolution is given by the pulse length of the source. The angular resolution is determined by the detector resolution and the sample to detector distance.

The measured signal on the position sensitive detector is a $I(t, z)$ map which can be transformed into a $I(\lambda, \theta)$ map. Each row corresponds to a TOF measurement at a given $\theta$, and each column corresponds to an angle dispersive measurement for a given $\lambda$. I.e. one combines the two conventional reflectometry set-ups to increase the specularly reflected intensity. But a disentangling of an off-specular signal is almost impossible.

Figure 2.11 shows an intensity map obtained by simulation, which illustrates the principle and the flux gain of this mode.

Figure 2.11: Intensity map $\log_{10}[\,I(\lambda,\theta)\,]$ for a Ni/Ti multilayer on Si obtained in the high-intensity specular reflectivity mode [→10.3]. The 4 coloured area correspond to the sample orientations $\omega = -0, 5°, 2°, 6°$, and $12°$, respectively. The gray-scale area are just a lead for the eye. The intensities are already normalised.
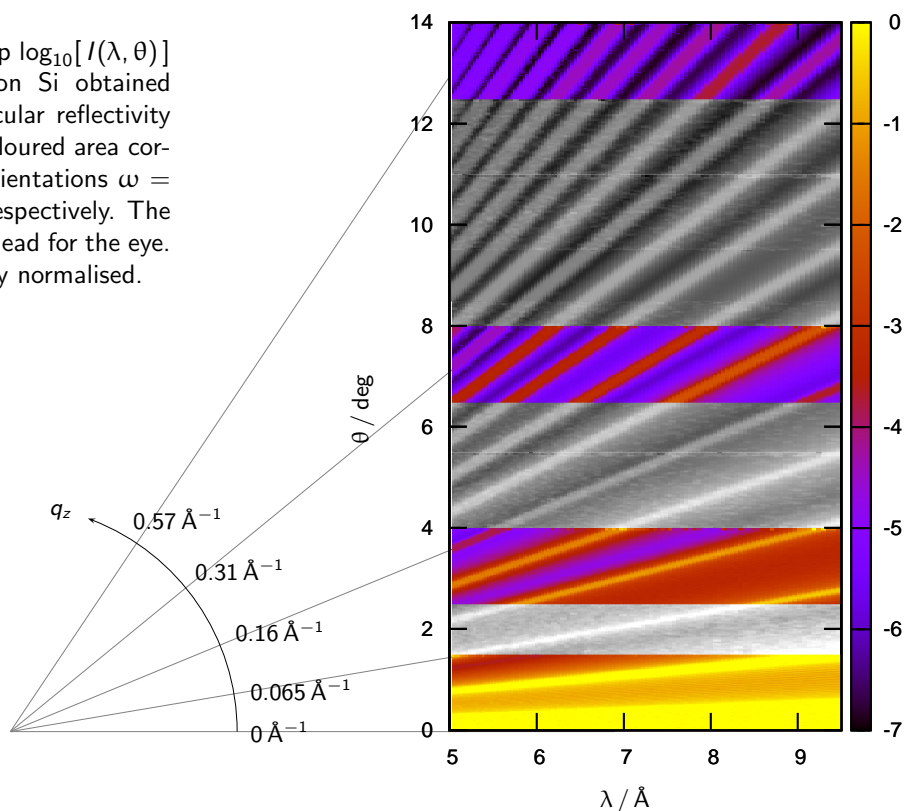
Thus this mode can be used
– on tiny samples where one is satisfied if some reflectivity curve can be obtained in a reasonable time,
– on samples with negligible off-specular or incoherent scattering,
– to screen the dependence of $R(q_z)$ on temperature, electric or magnetic fields, surface tension, or the like, and
– to perform time-resolved measurements on a s time-range.

There is no simple answer to the question of how much off-specular scattering from the sample itself, from the optical elements, or scattering from the sample environment affect the measurements. But it is no problem to check this whenever necessary: A comparison of $R(q_z)$ obtained in the almost conventional mode (achieved by just closing a slit) and in the high-intensity mode immediately tells how strong the influences are.

### 2.10.4    further options
The following options are not yet investigated in detail. If necessary analytical or numerical simulations will be made.

**focusing SANS**    The fact that the *Selene* guide gives a strongly focused beam can be directly used for setting up a focusing small angle scattering scheme. A detector has to be placed in the focal plane (where otherwise the sample is located), and the sample is positioned behind the guide end, some 2 m before the detector. This set-up gives an angular resolution of $\approx 0.03°$. The sample size can be up to $52 \times 52\,\text{mm}^2$ (using the full divergence of $1.5°$ and the minimum resolution).

**GISANS**    There are two principle modes of how GISANS could be realised. On can convert the focused beam into a parallel beam by using a parabolic reflector [→7.2]. This concept can be applied in the sample plane and in the specular scattering plane independently. The divergence of this beam is defined by the size of the virtual source. The width of the beam depends on the distance of the reflector form the focal point and can thus be tuned.

B. Hjörvarsson suggested an other approach: Using the convergent beam for GISANS results in a convolution of the detector image with the angular resolution function. While this is constant for all $\lambda$, the GISANS map

on the detector scales with $1/\lambda$. Using the TOF data and the known resolution function should thus allow for a rather precise deconvolution of the detector image. Since the divergence of the incoming beam can be modified in both directions independently, one can tune the resolution function.

**Rainbow**    The approach to spectrally analyse the reflected beam using a prism behind the sample [29, 30] can be realised if the beam is made parallel in one direction, e.g. by a parabolic reflector as described above. The detector resolution and distance allows for a high angular resolution needed for this method. The combination with TOF can be used for the measurement of inelastic processes. (The *rainbow* concept is mainly suited to reduce counting time on continuous sources.)

**MIEZE**    A group at TUM involving R. Georgii, W. Häußler and G. Brandl investigates the possibility to use a *Selene* type guide system for a dedicated MIEZE (Modulation of IntEnsity by Zero Effort) instrument. [R. Georgii, et al.:APL, **98**, 073505, (2011)] Their know-how can be used to develop an add-on MIEZE set-up for the proposed instrument. The coils can be located before the third or fourth guide segment, and before the sample. The elliptic shape of the guide guarantees the same length for all trajectories. Figure 2.12 illustrates the short version of the MIEZE set-up.
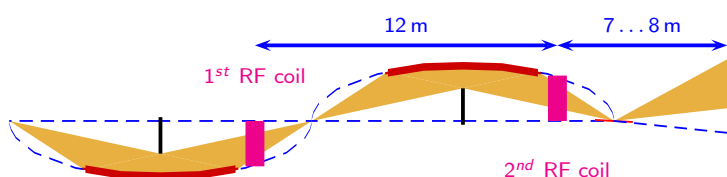


Figure 2.12: Sketch to illustrate the combination of MIEZE and a *Selene* guide.

## 2.11    simulations

Based on the parameters given in the previous section an instrument file for McStas was developed (T. Panzner) and a serious of simulations were performed.

Figure 2.7 shows sketches of the selected operation modes and the corresponding $I(\lambda, \theta)$ maps as detected with a 1000 Å Ni film on Si as a sample. The sample size was $5 \times 5\,\mathrm{mm}^2$. From these and a second set of maps obtained at a higher angle the reflectivity curves shown in figure 2.13 are obtained.

a) $\lambda$-$\theta$ encoding [$\rightarrow$2.10.2] by using a ML monochromator after the beam extraction.

This results in a diagonal streak in the $\lambda/\theta$ space, where $\Delta\lambda/\lambda = \Delta\theta/\theta = $ const. In the off-diagonal region the finite reflectivity of the ML monochromator leads to some structured background. This does not affect the specular reflectivity, but it might prohibit off-specular measurements.

b) High-intensity specular reflectometry [$\rightarrow$2.10.3] by substituting the ML monochromator by a supermirror.

Here all of the available $\lambda/\theta$ space is used for specular reflectometry. Off-specular and incoherent scattering leads to an enhanced background. This mode allows for a fast (and dirty) screening of external parameters as e.g. temperature or magnetic field strength, and for time-resolved studies.

c) Almost conventional reflectometry [$\rightarrow$2.10.1] by using a slit to cut down the divergence given by the set-up (b).

The specular reflectivity concentrates on one line, while the rest of the $\lambda/\theta$ space is available for off-specular measurements. The $q_z$ range accessible this way is reduced. A movement of the slit between pulses can be used to vary $\theta$ without tilting the sample.

Form these maps the reflectivity curves shown in figure 2.13 were obtained by integrating the $\lambda/\theta$ maps along constant $q_z$. The binning was done with $\Delta q_z/q_z = 1\%$. The error-bars shown were obtained by assuming $\Delta I/I = \sqrt{I}$ where $I$ is the flux given by the simulation, multiplied by a *measurement time* $t$. For the high-intensity specular reflectivity at the lowest angle $t = 1\,\mathrm{s}$ was chosen, the other values were adjusted to get comparable accuracy.
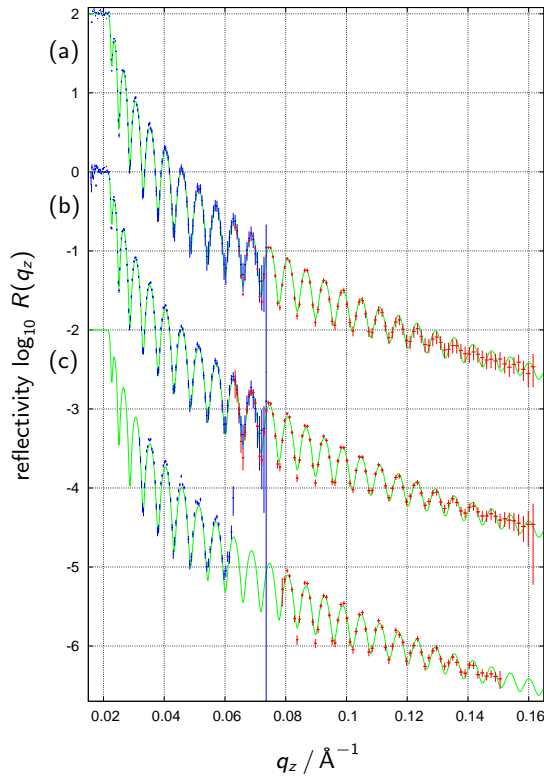
Figure 2.13: Reflectivities $R(q_z)$ extracted from the maps shown in figure 2.7 ($\omega = 2°$, blue) and from the corresponding maps for a higher angle ($\omega = 4°$, red). The corresponding modes are: (a) $\lambda$-$\theta$ encoding with $\Delta\lambda/\lambda = 3.5\%$, (b) high-intensity specular reflectivity, (c) almost conventional set up with $\Delta\theta/\theta = 4\%$. The curves are scaled by $10^2, 10^0, 10^{-2}$ for clarity. The green lines corresponds to the initial reflectivity with $\Delta q/q = 2.4\%$. The covered $q_z$ range and the resolution functions depend on the measurement scheme. The *measurement times t* used to obtain the error bars are

| mode | $\omega$ | $t$ |
|------|------|------|
| (a) | 2° | 60 s |
|  | 4° | 900 s |
| (b) | 2° | 1 s |
|  | 4° | 10 s |
| (c) | 2° | 10 s |
|  | 4° | 100 s |

## 2.12    performance

<span style="color:red">This has to be replaced by a comparison of the performance to the criteria mentioned in the science case.</span>

The following list is a comparison of the instrument's performance to the specifications of the STAP

- sample size: $= 5 \times 5\,\text{mm}^2$ taking into account sample environments

$\rightarrow$ The complete instrument is optimised for sample sizes below $10 \times 10\,\text{mm}^2$, down to below $1 \times 1\,\text{mm}^2$. It is possible to define an accurate footprint on the sample surface without penumbra.

  Samples wider than 10 mm and longer than 40 mm can not be homogeneously illuminated.

- wavelength resolution: up to 10% $\Delta\lambda/\lambda$ with options to increase to 1%, 3% or 5%.

$\rightarrow$ The intrinsic $\lambda$-resolution gives $\Delta\lambda/\lambda = 2\%$ to $4\%$ without beam manipulation. The requested resolution of 10% can thus not be realised via TOF. In the $\lambda$-$\theta$ encoding mode, this is possible.

  A resolution $\Delta\lambda/\lambda = 1\%$ for small $q_z$ is not possible due to the expected detector resolution.

  A constant $\Delta\lambda/\lambda$ ranging from 2% to 20% will be realised in the $\lambda$-$\theta$ encoding mode, only.

- Minimum $q$range:$0.005\,\text{Å}^{-1} < q < 0.5\,\text{Å}^{-1}$ measurable in 3 to 4 angles of incidence

$\rightarrow$ This requirement is easily matched. The upper limit is $q_z = 2\,\text{Å}^{-1}$ given by the highest reasonable detector angle.

  For $q_z \approx 0\,\text{Å}^{-1}$ the resolution requirements can not be fulfilled. Otherwise this region is accessible.

- low background: reflectivities $= 109$ measurable

$\rightarrow$ One big advantage of the *Selene* guide system is that it transports much less neutrons compared to other guides. This and the focusing to the sample should lead to a lower background and to a reduced illumination of the sample environment.

  A quantitative discussion is almost impossible.

- polarisation/polarisation analysis

$\rightarrow$ Full polarisation is a key-feature of the proposed instrument. There are various ways to polarise and to analyse the beam, all are well established so that there is no risk related.

  High magnetic fields at the sample position are possible. There is free space with a radius of more that 2 m available without any optical or mechanical component. Polariser and analyser can be located 12 m, and 6 m from the sample, so that an interaction with the sample field can be avoided.

- a GISANS collimation option and variable detector distance up to 15 m.

$\rightarrow$ This requirement is not matched. And it is ill-defined. The 15 m are needed for using a collimation system to *focus* the beam. For the proposed instrument this is already (and better) realised by the guide. Though not optimised for GISANS, one can in principle perform such measurements using a detector at the focal plane and by positioning the sample at the guide exit. This has not yet been studied in detail.

An important feature, not mentioned in this list is the minimum counting time, so that time-resolved measurements are possible. In the high-intensity mode a *blurred* resolution and an eventually complex background (off-specular and incoherent scattering) are accepted to increase the flux by at least one order of magnitude. This allows for measurements in the sub-second range for moderate $q_z$. counting time

# 3   Technical Maturity

[3 pages] [Identify key components that define the instruments performance and whether the functional requirements can be met with existing technology. If additional development is required, present a plan for the development and the technological risks associated. Present an appropriate risk mitigation strategy.]

## 3.1    guide system

The biggest challenge of the presented instrument is the long-term stability of the *Selene* guide alignment. It is relatively straight forward to set up and align the individual components, as long as one has full access. Once burrowed under concrete and activated, this is no longer the case for the 1$^{st}$ guide section.

A misalignment of the 1$^{st}$ guide section as a whole can be accepted if the pin-hole in the extraction unit is large enough to act as a virtual source also for the tilted or shifted guide. The misalignment of individual components is easy to trace, but not so easy to correct. A solution would be to put all components on actuators. But this would result in $\approx$ 150 degrees of freedom — which is essentially a costing problem. The realignment with these actuators is possible by using light optics or interferometry and an adapted computer algorithm. Tests to align the prototype elements with an interferometer were performed successfully at the SLS metrology lab.

P. Böni, SwissNeutronics, sugessted to mount all individual mirror elements of one guide segment (7.2 m long) on a rigid support (steel or granite beam). He claims that no realignment would be needed within this unit lateron. The 4 guide segments then have to be adjustable with regard to the source and pin-hole, and relative to each other. This results in 24 degrees of freedom (position and orientation of each segment).

A comparison with the accuracy and stability required for the elements of the ESS linear accelerator, or at a synchrotron beam line tells that the technology to keep the *Selene* guide aligned is available.

**guide accuracy**    The angular accuracy needed for the guide alignment can be estimated by looking at the longest free flight path before the sample. I.e. the trajectory from the entrance of the last guide segment to the sample. A beam off-set of 0.1 mm at the sample position corresponds to an angular error of 0.1 mm/9600 mm $\approx$ 10$^{-5}$ rad. The waviness of a state-of-the-art float glass guide is of the order 5·10$^{-5}$ rad.[1] A $yz$ position accuracy better than 0.1 mm can be achieved, so that this can be neglected compared to the influence of waviness. An orientation error of 10$^{-5}$ rad corresponds to an displacement of the 500 mm long guide element of 5 µm. This is a manageable quantity.

!!! reference to Panos' simulations

**monitoring**    The geometry of the *Selene* guide allows for a relative simple monitoring of the guide alignment. A point-like white light source (e.g. a LED) at the initial focal point of one segment should ideally produce a homogeneous rectangular image on a screen behind the final focal point. Any deviation of the guide surface from the exact elliptic profile leads to a redistribution of the intensity on the screen. Since there is a unique relation of any point on the screen to certain beam trajectory, it is possible to trace a intensity drop back to the part of the guide which is misaligned.

By coupling in/out the light by optical mirrors (e.g. Si wafers), this monitoring set-up can be installed permanently, allowing for a fast feedback.

The open questions are to find a radiation-resistand actuator, and to develop (or copy) the feedback system.

---

[1]This value was obtained by interferrometry measurements on the *Selene* guide prototype [→**??**].

## 3.2    optical components, polarisation

A prototype of a frame-overlap-filter / polariser working in transmission [→7.1] was successfully be tested in 5. 2013 at PSI. The double bonce monochromator was already successfully tested [→11.2.4].

Spin analysers using supermirror technology to cover a wide angular range or a large window are operational, e.g. at FOCUS, PSI, or at HYSPEC, SNS.

## 3.3    mechanics, sample stage

The mechanical support system for the sample and sample environment, and the analog support for the virtual source are standard components. The same is true for slow slit systems, and for stages to exchange optics or insert a CCD camera.

A challenge is the support system for the 2$^{nd}$ *Selene* guide section. This is some 20 m long, but it has to be adjusted with respect to the virtual source with an accuracy in the sub-mm range and an angular error well below 0.1°. Since it is expected that the heavy shielding leads to a drop of the monolith area with time, it is necessary that the guide can be realigned as a whole, without too much effort.

## 3.4    fast slit system

For all operation modes a slit behind the last guide segment is needed. For the almost conventional mode it defines the beam divergence and the angle of incidence, for all modes it helps aligning the sample. Such a slit is a standard component.

If one wants to switch the slit position and opening in between pulses, it must be able to change the blade positions by up to 60 mm within 10 ms. If this high speed (20 km s$^{-1}$) can not be reached, one looses several pulses during repositioning and thus time-resolved measurements might suffer.

When used to scan the beam during one pulse, both blades must move independently and very accurate over ≈ 60 mm within 60 ms and reset within 10 ms. This would allow to cut down unwanted scattering from the monochromator in the λ-θ encoding mode. If such a device is possible to realise is not clear. It was discussed with T. Gahl, ESS, but yet there is no clear conclusion so that further clarification is needed.[2]

## 3.5    detector

The detector technology available nowadays can be used in principle, so that even when new detector concepts fail, the operation of the instrument is guaranteed. The limitations of present days detectors are the resolution, the size and the accepted count rate.

In section 9.2 a wish-list of the detector properties is given together with the motivations.

<span style="color:red">This wish-list was sent to R. Hall Wilton and to H. Wacklin, both ESS, on February 2013 with the request to comment on it (reminder in May). There is no feed back up to now.</span>

Besides the additional costs for a new detector, there are no principle obstacles to replace the *day one* detector for a better one later.

## 3.6    computing, data analysis

The raw data will have a format of the type $I(t, y, z)$ (or the single event analog). Simple perl scripts to normalise, integrate and re-bin the data are written for the analysis of the prototype measurements. This means that the algorithms for data analysis are available.

The situation changes when one wants to conserve all information contained in the raw data for fitting. The re-binning and integration (especially in the high-intensity mode) leads to a reduction and mixing of resolution. To overcome this, one can compare measured and simulated intensity maps, rather than curves. The challenge is then to modify the output of a simulation program (eventually supported by reference measurements), and to implement a good fitting algorithm. The fitting *by eye* is no longer possible.

---

[2]State-of-the-art CNC laser-cutter mashines allow for positioning speeds of 20 mm/10 ms with heavy loads over large distances with 4 degrees of freedom. The position accuracy is 10 μm. Industry robots non-stop sorting pralins (4 axis, ≈ 1 m distance) realise up to 4 pics per second.

# 4  Costing

This is just a collection of cost estimates we got up to now. No man-power is included. No scheduling. We will take care of the ESS costing guidelines in the future.

The costs given below for some selected components of the instrument are based on requests to the manufacturer, on price lists and on feedback by the ESS. They display the situation beginning 2013.

## 4.1  insert in the extraction unit and instrument shielding

The measures and materials used for this estimate are based on input by P. Bentley, ESS, 10. 04. 2013.

The insert within the target monolith is assumed to consist of copper. Its measures are: $0.2 \times 0.2 \times 4.0 \, \mathrm{m}^3 = 0.16 \, \mathrm{m}^3 \stackrel{\wedge}{=} 1.4 \, \mathrm{t}$ (the free space of the beam can be neglected, here).

The masks at $18.6 \, \mathrm{m}$ and at $26 \, \mathrm{m}$ and between monolith and common shielding are assumed to use $1 \, \mathrm{m}^3$ copper, each. This corresponds to $27 \, \mathrm{t}$.

Assuming a copper price (04. 2013) of $6 \, \mathrm{k€}/t$ this gives $170 \, \mathrm{k€}$.

The instrument shielding (without the common shielding) from $x = 15 \, \mathrm{m}$ to $x = 25.8 \, \mathrm{m}$ is assumed to have a heavy concrete core with a cross section of $2 \times 2 \, \mathrm{m}^2$ (with the guide in the centre), and an outer shell of light concrete with a cross section of $5 \times 5 \, \mathrm{m}^2$. This corresponds to $44 \, \mathrm{m}^3$ of heavy concrete, and $226 \, \mathrm{m}^3$ of light concrete. A recent (01. 2013) offer to PSI for $200 \, \mathrm{m}^3$ light concrete and $50 \, \mathrm{m}^3$ heavy concrete summed up to $2\,000 \, \mathrm{k€}$ (without form factor or reinforcement).

The common shielding up to $x = 15 \, \mathrm{m}$ is not taken into account.

|  |  |
|---|---|
| insert and instrument shielding | 2 200 k€ |

## 4.2  guide

SwissNeutronics made an offer for the *Selene* neutron guide and the support system on January 2013. This offer fits the parameters for the double-*Selene* guide system as discussed in section 2.2.

The offer covers the neutron guide on glass or aluminium, the alignment frames, granite beams as a base and an aluminium housing to contain the vacuum. This does not exactly match the requirements by the ESS, since shielding issues most likely will not allow for the offered wide and straight vacuum housing and the alignment system with frames. But it still gives an idea of the actual costs to be expected. For the guides the offer covers the curved substrates with a $m = 2.5$ Ni/Ti coating. In detail there are 4 guide sections of $7.2 \, \mathrm{m}$, each, consisting of 15 elements, made up of 2 truly curved mirrors.

|  |  |
|---|---|
| double-*Selene* guide system | 550 k€ |

## 4.3  guide support

The support consists of 4 granite beams on kinematic mounts, the alignment frames, the vacuum housing, and vacuum windows. No shielding is included. Mounting is due to the customer.

|  |  |
|---|---|
| guide support | 520 k€ |

## 4.4    mechanics (sample stage and the like)

<span style="color:red">Request to Peter Keller, LDM mechanics, PSI, on 26. 03. 2013.</span>

<div align="center">

motion mechanics        ??? k€
</div>

## 4.5    motion control

(discussed with T. Gahl, ESS, 18. 03. 2013) For the *standard* components (i.e. without fast aperture [→**??**]) an approximate price per freedom of 4 k€ is assumed, including motor controller, encoder, motor, and cabling. This leads to

<div align="center">

motion control        150 k€
</div>

## 4.6    detector

<span style="color:red">Request to Richard Hall-Wilton, ESS, on 20. 02. and on 19. 03. 2013.</span>

monitor <span style="color:red">[to be done]</span>

A CCD camera with scintillator and housing for instrument and sample alignment (based on a similar system purchased for BOA at PSI) costs $\approx 60$ k€.

<div align="center">

detectors        ??? k€
</div>

## 4.7    filter / polariser

Based on the costs of a prototype of the bent frame-overlap and polarisation filter, a similar but longer device will cost some 25 k€.

The price for one RF flipper (electronics, coils, magnets and housing) is approximately 30 k€ (private communication with P. Hautle, PSI).

analyser (Uwe) <span style="color:red">[to be done]</span>

<div align="center">

polarisation equipment        ??? k€
</div>

# 5   List of abbreviations

| physical quantities | |
|---|---|
| $x$ | lab-system: horizontal scale, *along the main neutron path* |
| $y$ | lab-system: horizontal scale, normal to $x$ |
| $z$ | lab-system: vertical scale |
| $t$ | time, with $t = 0$ at the beginning of a neutron pulse |
| $\tau$ | ($\approx 2.8\,\mathrm{ms}$) length of the proton pulse |
| $T$ | ($= 70\,\mathrm{ms}$) pulse repetition time |
| $\lambda_{\mathrm{min}}$ | shortest wavelength used for measurements |
| $\lambda_{\mathrm{max}}$ | longest wavelength used for measurements |

| ellipse parameters describing the guide geometry | |
|---|---|
| $a$ | long half-axis |
| $b$ | short half axis |
| $c$ | ($= a^2 - b^2$) distance from focal point to center |
| $b/a$ | asymetry of ellipse |
| $\alpha$ | angle between long axis and end of guide seen from the first focal point |
| $\beta$ | angle between long axis and beginning of guide seen from the first focal point |
| $\Delta\theta$ | ($= \beta - \alpha$) accepted divergence of the guide |
| $\epsilon$ | ($= \beta/2 + \alpha/2$) inclination of the long axis relative to the mean beam direction |
| $\xi$ | length of the guide relative to the distance between focal points |



| nomenclature for positions along the guide | |
|---|---|
| $P_i$ | first focal point of guide section $i$ |
| $P_{i+1}$ | second focal point of guide section $i$, and first focal point of guide section $i + 1$ |
| $P_5$ | ..., and sample position |

| sample coordinate system | |
|---|---|
| $\omega$ | inclination of the sample surface relative to the long axis of the last guide, in the scattering plane<br>this is a pure instrument parameter and is only indirectly connected to the angle of incidence! |
| $\theta_i$ | actual angle of incidence of a neutron on the sample surface |
| $\theta_f$ | final angle of a neutron leaving the sample surface |

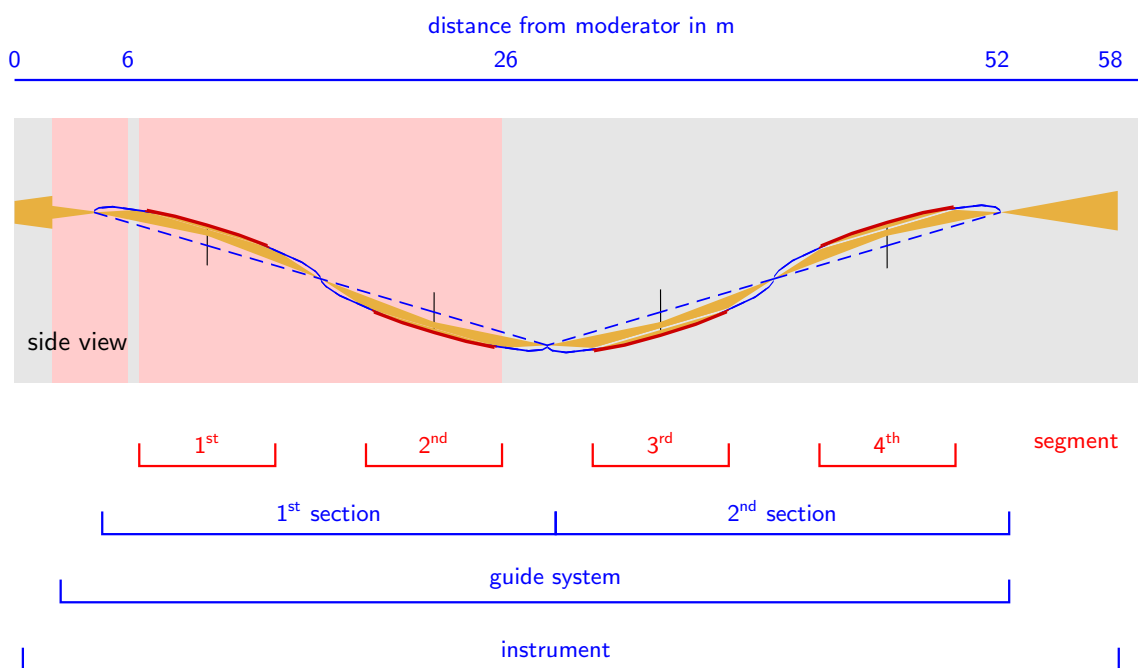Figure 5.1: Nomenclature used in this script to adress the various items and measures of the double *Selene* guide. The sketch is taken from figure 2.1. The guide segments are the elliptically curved and SM coated guides. The distance between the initial and final focal point of one *Selene* guide is called section. Here, two sections and the extraction unit make up the guide system, ending at the sample position.

# 6  the Selene guide system

We chose two subsequent elliptically shaped reflectors to focus the beam to the sample. The reason is that this set-up allows for

- independent definition of the divergence $\Delta\theta$, and of the beam spot size at the sample;

- a three-dimensional definition of the footprint;

- convenient beam manipulation;

- early reduction of the phase space, i.e. low background and radiation in the sample and detector region.

At the same time all trajectories have the same length. In the following subsections several aspects of the *Selene* guide system are presented.

The design and a large part of the optimisation of the *Selene* guide system was performed analytically. This is possible because of the rather straight-forward and clear mathematical description of the possible beam trajectories. As a consequence one can relate allmost all geometrical parameters of the guide system, the coating and the transmission. The rather large number of parameters collapses this way to essentially three which can be chosen freely. All the rest is then determined. In the following sections these relations are derived and discussed.

Figure **??** illustrates the approach chosen here for the design the instrument, starting with some guess for the desired divergences and wavelength-range at the sample position. The second set of input parameters are the given source brightness $I_0(\lambda)$ and a reasonable length of the guide, described by the ration of the actual guide segment length to the focal ponit distance, $\xi$. As figure of merit the measurement time $t$ is used. The physical parameters of the guide ($b/a$ and $\epsilon$) are deduced from the starting parameters and they determine the coating ($m$), reflectivity ($R$) and thus the transmission $T$ of the guide. Togther with the divergence and $I_0(\lambda)$ this determines the counting time.

The *optimisation problem* can be illustrated at the example of $\Delta\theta$, which enters the counting time quadratically (for high-intensity specular reflectivity), but which also affects $m$ linearly. Since high $m$ leads to a lower transmission $T$ with a more complicated dependence, one has to iteratively find the best $\Delta\theta$.

### history

The idea for the *Selene* guide is based on concepts of F. Ott to use a focused beam with a wide divergence, and in combination a $\lambda$-$\theta$ encoding obtained by a graded monochromator of half-elliptic shape.[22, 23] First experiments with a graded multilayer coating [31] revealed conceptual problems and led to the approach to use a flat multilayer monochromator for $\lambda$-$\theta$ encoding, followed by the elliptic reflector. And attempts to correct for coma aberration finally led to the *Selene* guide geometry with two subsequent elliptic reflectors. This way, neutron guide and encoding are decoupled. I.e. encoding is optional and might be also achieved by other approaches like the *rainbow* concept by R. Cubitt.[29, 30]

Though developed for a reflectometer, the *Selene* guide concept can in principle used also for other instruments. The limiting factors are the transported divergence, the minimum wavelength, and the sample size.
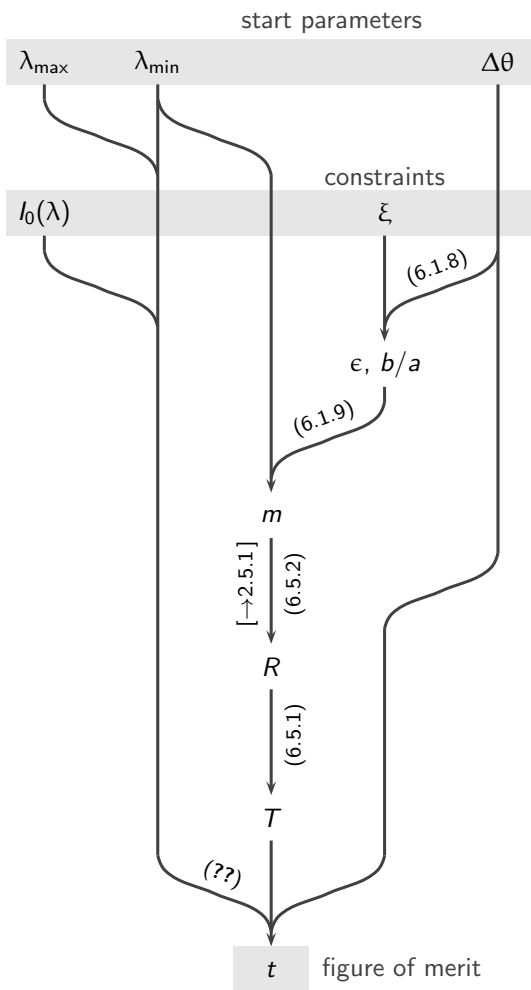
Figure 6.1: Flow diagram used to estimate the counting time $t$ as a figure of merit from chosen ($\lambda$-range, $\Delta\theta$) and given ($I_0(\lambda)$, $\xi$) start parameters.

The meaning of the other symbols is: $\epsilon$, $b/a$ orientation and shape of the ellipses, $m$ coating of guides, $R$ reflectivity of the guide, and $T$ transmission of the guide system.

The diagram is simplifyed since it is based on the ideal assumption of a point-like sample, perfect guides and coatings, and some external constraints as the exclusion of the prompt time for data collection [→**??**] are not taken into account.

## 6.1 geometrical considerations for an elliptic reflector

The geometry of the elliptic guides (i.e. the ratio of the half axes $b/a$), their length and coating should be defined starting by the requirements at the sample position. The limitations are the maximum curvature of the guide, the available coating, $I_0(\lambda)$, and the space available.

The following formulae can be used to estimate the optimum geometry of a *Selene*-type guide for given parameters like expected divergence $\Delta\theta$, and wavelength range $\lambda_{min} \ldots \lambda_{max}$.

Theses formulae are based on the small-angle approximation $\tan\alpha \approx \alpha$, $\tan\beta \approx \beta$, a strong asymmetry of the ellipse $a \gg b \Rightarrow c \approx a$, and a symmetric guide.

ellipse relation:

$$\frac{x^2}{a^2} + \frac{y^2}{b^2} = 1$$

$$y = \pm\frac{b}{a}\sqrt{a^2 - x^2}$$

$$c = \sqrt{a^2 - b^2} \qquad \text{half distance between focal points}$$

minimum acceptance angle (relative to long axis):

$$\alpha \approx \frac{b}{a}\frac{\sqrt{a^2 - (\xi a)^2}}{(\xi + 1)a}$$

$$\approx \frac{b}{a}\sqrt{\frac{(1 - \xi)(1 + \xi)}{(1 + \xi)^2}}$$

$$\approx \frac{b}{a}\sqrt{\frac{1 - \xi}{1 + \xi}}$$

$$\approx \frac{b}{a}\frac{1 - \xi}{\sqrt{1 - \xi^2}} \tag{6.1.1}$$

maximum acceptance angle (relative to long axis):

$$\beta \approx \frac{b}{a}\frac{\sqrt{a^2 - (\xi a)^2}}{(\xi - 1)a}$$

$$\approx \frac{b}{a}\sqrt{\frac{(1 - \xi)(1 + \xi)}{(1 - \xi)^2}}$$

$$\approx \frac{b}{a}\sqrt{\frac{1 + \xi}{1 - \xi}}$$

$$\approx \frac{b}{a}\frac{1 + \xi}{\sqrt{1 - \xi^2}} \tag{6.1.2}$$

accepted / delivered divergence:

$$\Delta\theta = \beta - \alpha$$

$$\approx \frac{b}{a}\left(\frac{1 + \xi}{\sqrt{1 - \xi^2}} - \frac{1 - \xi}{\sqrt{1 - \xi^2}}\right)$$

$$\approx \frac{b}{a}\frac{2\xi}{\sqrt{1 - \xi^2}} \tag{6.1.3}$$

inclination of the center of the beam relative to the long half axis:

$$\epsilon = \frac{1}{2}(\alpha + \beta) \tag{6.1.4}$$

$$\approx \frac{1}{2}\frac{b}{a}\left(\frac{1 + \xi}{\sqrt{1 - \xi^2}} + \frac{1 - \xi}{\sqrt{1 - \xi^2}}\right)$$

$$\approx \frac{1}{2}\frac{b}{a}\frac{2}{\sqrt{1 - \xi^2}}$$

$$= \frac{\Delta\theta}{2\xi} \tag{6.1.5}$$

minimum coating of the guide surface:

$$m = \frac{4\pi \frac{\alpha + \beta}{2}}{\lambda_{\min} q^c_{Ni}} \quad \text{with (6.1.4):}$$

$$= \frac{4\pi \epsilon}{\lambda_{\min} q^c_{Ni}} \tag{6.1.6}$$

Starting with input parameters $\lambda_{\min}$ and $\Delta\theta$ required at the sample, and with $\xi$, it is possible to deduce all other paramters:

$$\frac{b}{a} \approx \frac{\Delta\theta}{2}\sqrt{\frac{1}{\xi^2} - 1} \tag{6.1.7}$$

$$\epsilon \approx \frac{\Delta\theta}{2\xi} \qquad \text{inclination of the guide, and} \atop \text{maximum angle of incidence on the guide} \tag{6.1.8}$$

$$m = \frac{4\pi \epsilon}{\lambda_{\min} q^c_{Ni}} \qquad \text{for a finite source, the angular error has to be} \atop \text{taken into account to calculate the \textit{real} m} \tag{6.1.9}$$

and

$$\alpha \approx \epsilon \cdot (1 - \xi) \qquad (6.1.10)$$
$$\beta \approx \epsilon \cdot (1 + \xi) \qquad (6.1.11)$$

For $\Delta\theta \approx 2\epsilon$ the pre-assumptions are no longer fulfilled! A reasonable upper limit for $\xi$ is about 80%.

Example:
$m = 5$ and $\lambda_{min} = 3\,\text{Å}$ gives $\epsilon = 1.5°$ and

| $\Delta\theta$ | $\xi$ | $b/a$ |
|---|---|---|
| 1.0° | 33% | 0.025 |
| 1.5° | 50% | 0.023 |
| 2.0° | 66% | 0.020 |
| 2.5° | 83% | 0.014 |
| 3.0° | 100% | 0.000 |

Figure 6.2 shows the iso-lines for constant $m$ and for constant $\Delta\theta$ on a map of $b/a$ vs. $\xi$, obtained for $\lambda = 4\,\text{Å}$. E.g. if a divergence of $\Delta\theta > 3°$ is required, but the coating is limited to $m = 6$ the possible values for $b/a$ and the relative length $\xi$ are within the (light gray) area below the blue iso-line for $m = 6$ and above the red iso-line for $\Delta\theta = 3°$. So the smallest $xi$ is $\approx 0.62$ with the strong curvature $b/a \approx 0.033$. Relaxing the latter value leads to a longer guide and allows for a coating with lower $m$.
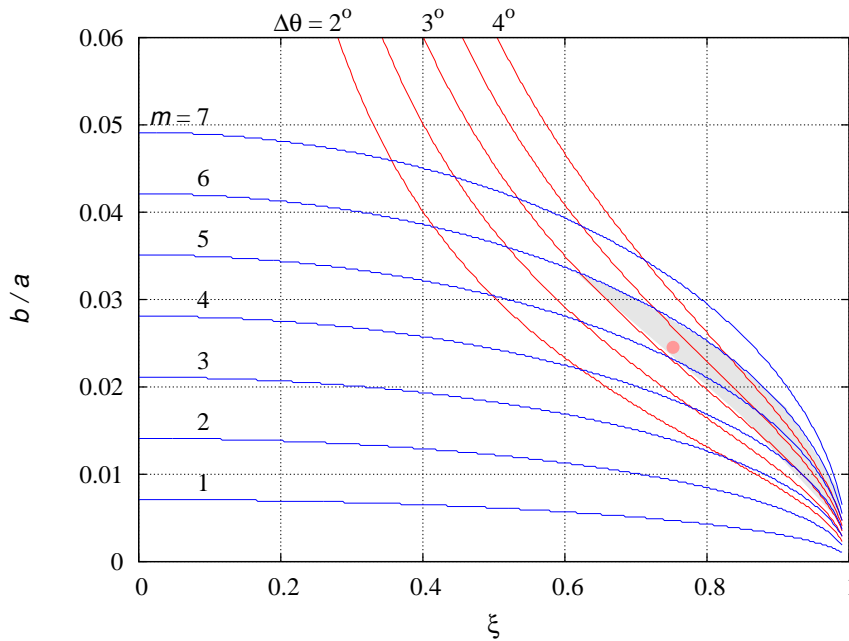


Figure 6.2: Iso-line for constant $m$ (blue) and for constant divergence $\Delta\theta$ (red) for $\lambda = 4\,\text{Å}$ as a function of the length of the guide and the ratio of the half axes parameters $b/a$.

Reducing the wavelength e.g. from $4\,\text{Å}$ to $2\,\text{Å}$ does not affect the red iso-line, but the blue ones are scaled down by 0.5 along $b/a$. There is no intersection left (for reasonable guide lengths) with the $\Delta\theta = 3°$ criterion, so that there is no guide geometry possible fulfilling the requirements.

For $\Delta\theta = 3°$ and $\lambda = 4\,\text{Å}$ a reasonable choice would be $b/a \approx 0.025$ and $\xi = 0.75$ (marked by a red dot). The coating then should be $m \approx 5.5$.

## 6.2    angular acceptance

We are often confronted with the remark that a full ellipse could transport twice the divergence of half an elliptic guide. The point is that the divergence should be defined by the needs on the sample, or it is given by geometrical limitations. In this case one has to ask for the most efficient way to transport this divergence.

And if this can be realised with one branch of an ellipse, there is no need to accept the disadvantages of the full ellipse.

For a given $\lambda_{min}$ and $\Delta\theta$ there is only one degree of freedom left to define all geometrical parameters of the ellipses and the coating For a reflectometer one can obtain approximately an optimum set of $\Delta\theta$ and $m$ when optimising for brilliance transfer. The characteristic measures of the guide then are

$$\text{maximum incident angle on guide} = \text{inclination of the ellipse} \quad \epsilon \quad \approx \quad \frac{\lambda_{min}\, m q_{Ni}^c}{4\pi} \tag{6.2.1}$$

$$\text{length of the reflector relative to } 2a \quad \xi, \quad \approx \quad \frac{\Delta\theta}{2\epsilon} \tag{6.2.2}$$

$$\text{asymmetry of the ellipse} \quad \frac{b}{a} \quad \approx \quad \sqrt{\epsilon^2 - \Delta\theta^2/4} \tag{6.2.3}$$

So besides for the length $4c$, the guide system is defined.

## 6.3 coma aberration — and correction

Elliptic reflectors show coma aberration. This means two things: radiation emitted from (close to) the first focal point into a solid angle $\Omega$ and reflected before the mid of the ellipse reaches the second focal point under a smaller solid angle. Radiation emitted in $\Omega$ but reflected behind the mid of the ellipse result in a large solid angle. I.e. The focusing / de-focusing property of the reflector varies along its length.

At the same time the position of the image of an off–axis pre-image point depends on the position where along the reflector the beam is reflected. For an early reflection the distance of the image from the long axis increases, for a late reflection it decreases.

In total the phase space density is conserved, but the distribution intensity vs. angle and beam-height $I(\theta, z)$ is distorted.

For geometries and reflection angles typical for neutron guides one can estimate the image size as a function of the initial slit size $z_1$ and the angle $\alpha_2$ between the reflected beam and the long axis of the ellipse:

$$z_2(\alpha) \quad \approx \quad z_1 \frac{(b/a)^2}{\alpha_2^2} \tag{6.3.1}$$

An identical second collinear reflector, sharing one focal point with the first one shows the same aberration, but since early reflection in the first reflector leads to a late reflection in the second one, the distortion is almost cancelled.

Analytically this can be shown by using eqn. 6.3.1 and $\alpha_2\alpha_1' = \alpha_3\alpha_2' = (b/a)^2$, $\alpha_2 = \alpha_2'$. For the final image $z_3$ one gets

$$z_3(\alpha_3) \quad \approx \quad z_2(\alpha_2) \frac{(b/a)^2}{\alpha_3^2} \quad \approx \quad z_1 \frac{(b/a)^2}{\alpha_2^2} \frac{(b/a)^2}{\alpha_3^2} \quad \approx \quad z_1 \tag{6.3.2}$$

This is illustrated in figure 6.3. The maps show $I(\theta, z)$ as accepted by the elliptic reflectometer (left), the corresponding intermediate image with the distorted shape (middle) and the almost restored shape at the image (source) position. The deviations still visible originate from the final length of the second reflectometer, and from the quite large pre-image chosen to emphasise the effect of coma aberration.

It is not always useful to correct for coma aberration: If e.g. a small beam is required, on can reach this by using the beam reflected at the end of the reflector. For the presented case its height is 30% of the initial slit, only. On the other side one can get a wide beam of low divergence by using the beginning of the reflector, only. This is what at synchrotron sources is achieved with a Kirkpatrick-Baez optics (which consists of two elliptically shaped reflectors, one for each direction).
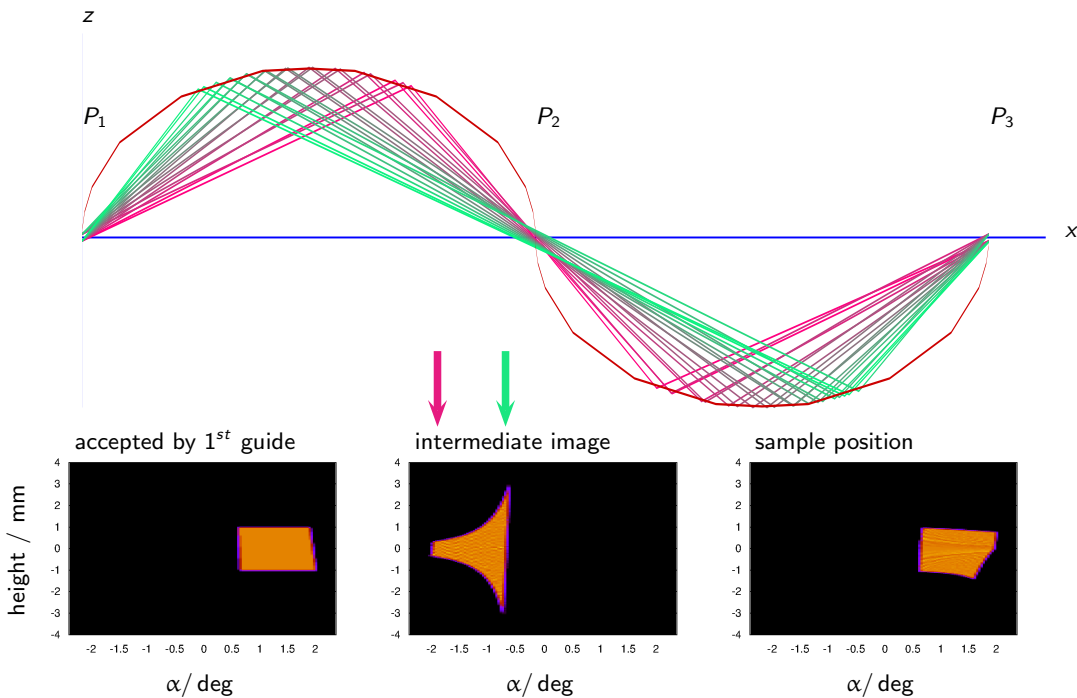
Figure 6.3: Sketch to illustrate the effect of coma aberration. The pre-image consists of 2 point-sources, located at $z = \pm 1\,$mm. The half-axis parameters used here are $a = 2000\,$mm, $b = 50\,$mm, the sketch is stretched by 30 normal to the long axis. The take-off angle $\alpha$ is encoded in the colour of the beam. At the intermediate position a clear separation of the colours can be seen. High $\alpha$ result in an almost parallel wide beam, while low $\alpha$ result on a beam focused to the second focal point. Behind the second ellipse, the initial image is almost restored. The $I(\alpha, z)$ maps illustrate the shape of the phase space as accepted by the ellipse and defined by a 2 mm slit at $P_1$ (left), at the intermediate position $P_2$ (middle), and finally after correction at $P_3$ (right). The arrows atop the middle map denote for which $\alpha$ the beam is compressed (red) or expanded (green).

## 6.4    chromatic aberration due to gravity

P. Korelis, E. Rantsiou

While the focusing properties of reflecting optics are achromatic (besides the $\lambda$ dependent reflectivity) for straight trajectories, there are chromatic effects induced by gravity. Its influence on the spot size and divergence is not immediately apparent because there are amplifying and compensating aspects for reflections on an elliptic guide. E.g. if one assumes the first reflection pointing downwards, gravity leads to a longer free flight path before the neutron hits the reflector. But it will hit it at a smaller angle.

The drop of the neutrons due to gravity is given by

$$\Delta z = -\frac{1}{2}\,g\,t^2$$
$$g \approx 9.81\,\text{m/s}^2$$
$$t \approx 2.52 \cdot 10^{-4}\,\text{s m}^{-1}\,\text{Å}^{-1} \times \lambda$$
$$\Rightarrow \frac{\Delta z}{\text{m}} \approx 3.07 \cdot 10^{-7}\left(\frac{x}{\text{m}}\frac{\lambda}{\text{Å}}\right)^2$$

So $\Delta z$ scales with distance and wavelength squared.

| $\Delta z$ | $x = 2400\,$mm | $9600\,$mm | $19200\,$mm |
|---|---|---|---|
| $\lambda = 5.0\,$Å | $-0.04\,$mm | $-0.7\,$mm | $-2.8\,$mm |
| $9.4\,$Å | $-0.16\,$mm | $-2.5\,$mm | $-10\,$mm |

The main question to be answered then is whether or not gravity sets limitations to the focusing performance of a *Selene* guide at the sample position. To elucidate the effect of gravity, virtual studies using the McStas simulation software package have been performed.
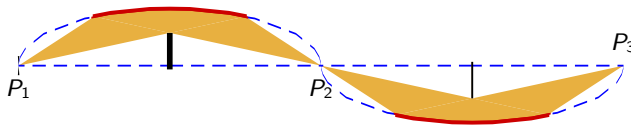
Figure 6.4: Sketch of the setup used for simulations including gravity. The guide parameters are $c = 10\,000$ mm, $b/a = 0.0228$ and $\xi = 0.5$. The initial slit has a height of 1 mm and is centred at the focal point.

The model instrument is comprised of a single *Selene* guide with the first element reflecting downwards and the second reflecting upwards as shown in figure 6.4. The geometrical parameters are the same for the horizontal ($xy$ plane) and vertical ($xz$ plane) elliptic reflectors: $b/a = 0.0228$, $\xi = 0.5$, and length of the focusing section $4c = 40$ m. The resulting angular acceptance is $\Delta\theta = 1.5°$.

To single out the effect of gravity and to better illustrate that, certain simplifications have been added to the model. Regarding reflector performance, the reflectors are constructed from ideal supermirrors, disregarding changes in supermirror reflectivity as a function of momentum transfer and effects such as absorption. A virtual source is used, with a uniform wavelength distribution extending from 2 to 10 Å, and it is located at the entrance focal point of the *Selene* guide. The size of the source is $1 \times 1$ mm$^2$ and its divergence is adjusted to compensate for the crooked neutron trajectories that might result in some of the long-wavelength neutrons missing the far end of the reflector. As a result, the entirety of the reflecting surface of the first *Selene* element is illuminated by neutrons of all wavelengths.

Figure 6.5 shows the intensity maps at the intermediate focal point $P_2$, simulated with and without including gravity (bottom and top row, respectively). To single out with which trajectory certain features in the intensity maps are related, the first and second half of the first guide element were interchangeably switched to be vertically absorbing. The horizontal reflection element was fully reflecting in all cases.

The coma aberration, inherent to the elliptical shape of the reflectors, is evident in the intensity maps in the top row. Reflecting on the first half of the vertical elliptical reflector (left image) contributes a broad beam



Figure 6.5: Intensity maps $\log_{10}[I(y, z)]$ at the intermediate focal point $P_2$ of a *Selene* guide system with a total length of 40 m. The upper row was simulated without gravity, the lower one with gravity. For the left/right column only the first/second half of the vertically reflecting guide element was actually reflecting. The middle column was obtained with reflection along the full guide element. The incident slit was $1 \times 1$ mm$^2$, the wavelength range was $\lambda \in [2, 10]$ Å.

profile at $P_2$. In an inverse manner, reflecting on the second half of the vertical elliptical reflector (right image) results in a highly focused beam profile. As expected, the centre image in the top row, generated by reflecting on the complete first element, shows no difference in the intensity profile between the vertical and horizontal direction.

Gravity is included in the simulations shown in the bottom row. While no change in focusing is observed in the horizontal direction, a tail becomes visible in the vertical direction. Gravity does little to improve the focusing of neutrons reflected on the first half of the vertical elliptical reflector. The vertical tail is also shown to originate almost exclusively from reflections on the first half of the reflector. Reflections on the second half of the vertical elliptical reflector (bottom right image), are found to result in some smearing out of the bright focused spot, along the positive direction of the vertical axis. It was further clarified, through simulations using a single wavelength, that the vertical position of the focusing spot at $P_2$ shifts upwards, scaling with neutron wavelength. On one hand, the height of the focusing position for longer wavelengths is shifted upwards, and on the other hand, the long-wavelength neutrons are also more heavily influenced by gravity on their way to the second *Selene* element.

The intensity maps of the beam spot at the exit focal point $P_3$ are shown in figure 6.6, simulated with and without gravity. In the graph to the right, the intensity is integrated along the horizontal direction and the distribution of intensity as a function of the vertical position is shown for selected wavelengths.

Comparing the intensity maps, the beam profile appears to be close to fully restored. It becomes apparent that a compensating mechanism exists for the effect of gravity for small $\lambda$, once the neutrons have travelled through and interacted with the full length of the *Selene* guide. The integrated intensity as a function of vertical position indicates that for small wavelengths, e.g., 3 Å, the effect of gravity is negligible. For wavelengths near the upper end of the range that is expected at ESS for a *Selene* type reflectometer, there is an observable change, manifested by a vertical shift of the centre of the focused spot by approximately 0.3 mm, broadening at the base by nearly the same amount and a corresponding reduction in the intensity of the maximum plateau by about 15%.

The $I_\lambda(z)$ graph illustrates that there is only a week chromatic aberration up to at least 6 Å and a moderate effect at 9 Å. Above that the picture changes, the intensity for $\lambda = 15$ Å, for example, is distributed over 4.5 mm with a bimodal distribution. Obviously there is an upper limit for $x^2 \lambda^2$, up to which the *Selene* guide has low chromatic aberration due to gravity.

In a further set of simulations the geometry shown in figure 6.4 was turned upside down, i.e. the first guide element reflecting downwards and the second upwards. The essential difference is, that for longer wavelengths the intensity is reduced (some 10% at $\lambda = 9$ Å), while the spot size is slightly smaller.
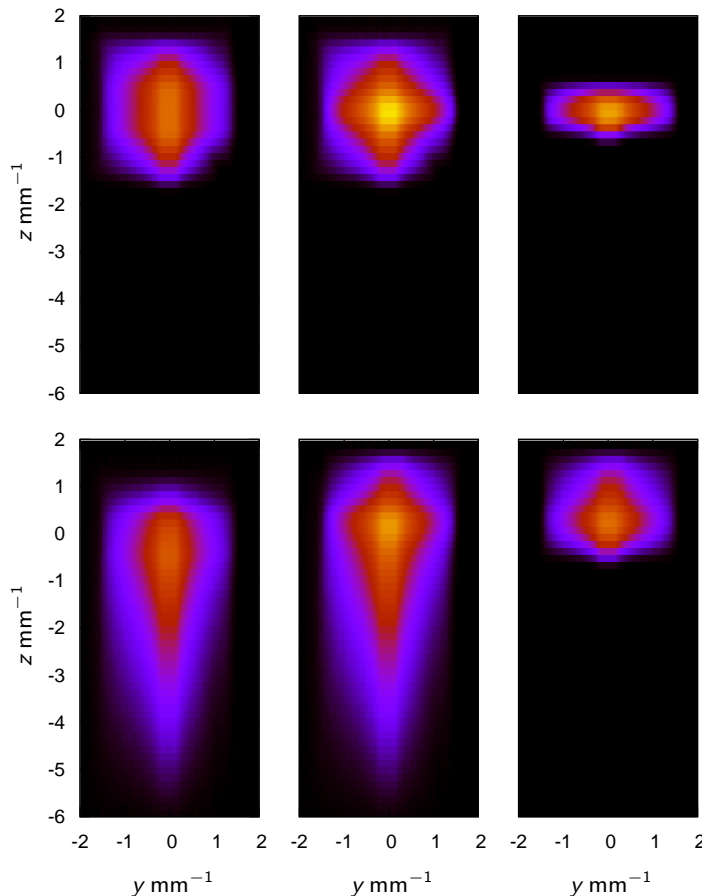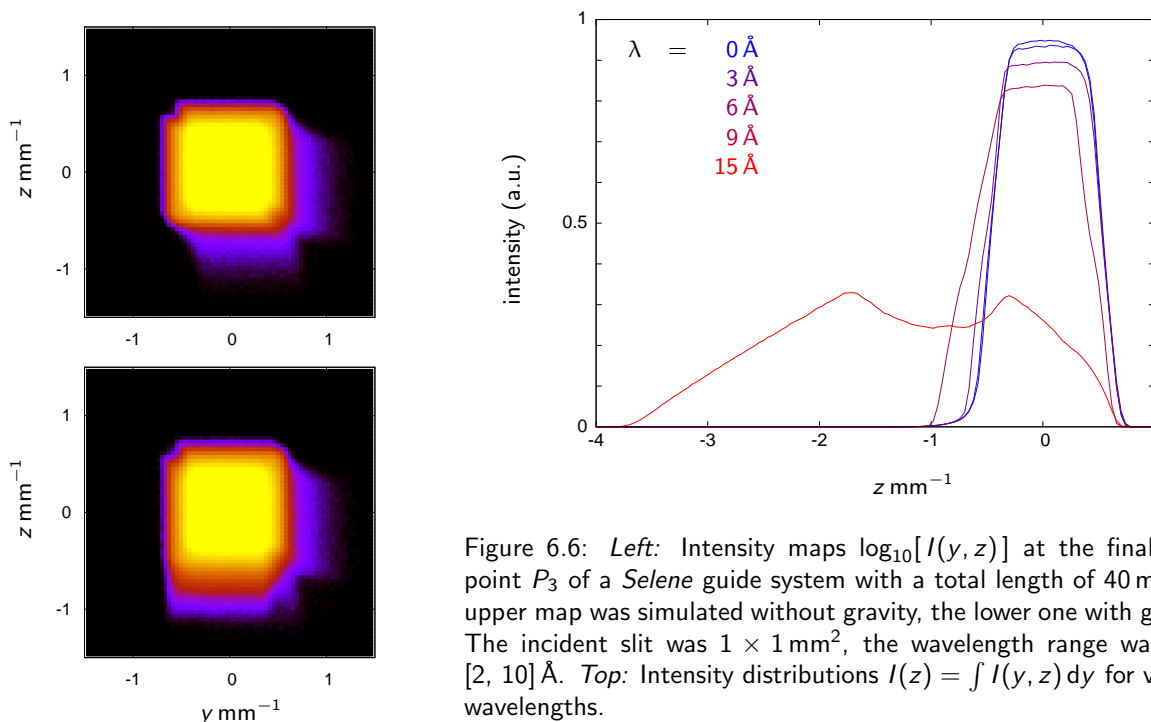


Figure 6.6: *Left:* Intensity maps $\log_{10}[I(y, z)]$ at the final focal point $P_3$ of a *Selene* guide system with a total length of 40 m. The upper map was simulated without gravity, the lower one with gravity. The incident slit was $1 \times 1$ mm², the wavelength range was $\lambda \in [2, 10]$ Å. *Top:* Intensity distributions $I(z) = \int I(y, z)\,dy$ for various wavelengths.

**discussion**    Taking into account that the actual length of one *Selene* section will be 24 m instead of the 40 m used here, while keeping the $\lambda$ range, one can assume that the chromatic aberration plays in the sub-mm range for the proposed reflectometer with two *Selene* sections.In addition, it affects only the spot size normal to the scattering plane.

## 6.5    transmission

The effective flux at the sample can be estimated by reducing the initial flux $I_0(\lambda)$ by the losses due to reflections on the guide walls. The double *Selene* guide concept involves 8 reflections for all neutrons on surfaces with a non-perfect reflectivity $R$ (plus further reflections in the extraction unit). The angle of incidence on the guide surface hardly varies along the guide for the presented concept: $\theta \approx \epsilon = \Delta\theta/2\xi$. One can thus assume $R(q_z) = R(\lambda, m)$, with the optimised coating $m$ [$\rightarrow$6.1.9]. This leads to and an attenuation of

$$I(\lambda) \quad = \quad I_0(\lambda) \cdot \prod_{i=1}^{n} R(\lambda, m_i) \tag{6.5.1}$$

$n$ is the number of reflections,. This pushes the flux maximum to higher $\lambda$. For the example given in figure **??** a linear decrease of $R$ with $\lambda$ was chosen:

$$R(\lambda, m) \quad = \quad \begin{cases} 1 & \text{for } \lambda > m\,\lambda_{\min} \\ 0 & \text{for } \lambda < \lambda_{\min} \\ \frac{13}{12} - \frac{1}{12}\frac{m\,\lambda_{\min}}{\lambda} & \text{else (i.e. 50\% reflectivity at } m = 7 \text{ and 100\% at } m = 1) \end{cases} \tag{6.5.2}$$

The coating was characterised by $m = 2.5$.

# 7 Optics and Beam Shaping

## 7.1 frame-overlap and polarisation filter

An optical element used for polarising a beam or for frame-overlap supression (i.e. used as a low-pass for $\lambda$) should ideally intersect the beam at the same optimised angle $\gamma$ everywhere within the beam. For a parallel beam this is fulfilled by a flat surface, inclined relative to the beam by $\gamma$. For a beam emerging from a point the corresponding surface has the shape of a logarithmic spiral. For a small $\gamma$ and a rather low divergence $\Delta\alpha \ll 10°$ the spiral can be approximated by a function $f(x)$. A trajectory passing through the origin has the function

$$y_\alpha(x) \;=\; x\tan\alpha \tag{7.1.1}$$

It intersects $f(x)$ at the point where $f(x) = y_\alpha(x)$. At this point the slope of $f(x)$ has to be $\tan(\alpha + \gamma)$, where $\tan\alpha$ is the slope of the trajectory. Thus

$$
\begin{aligned}
\tan\alpha &= \frac{f(x)}{x} \\
f'(x) &= \tan(\alpha + \gamma) \\
&= \frac{\tan\alpha + \tan\gamma}{1 - \tan\alpha\tan\gamma} \\
&= \frac{f(x)/x + \tan\gamma}{1 - f(x)/x\tan\gamma} \tag{7.1.2} \\
&\approx \frac{f(x)}{x} + \gamma \qquad \text{for small } \gamma \text{ and } \alpha \tag{7.1.3}
\end{aligned}
$$

It is assumed here that all angles are small. The solution for the simplified differential equation (7.1.3) is

$$f(x) \;=\; \gamma\, x \, \ln\left[\frac{x}{x_h}\right] \tag{7.1.4}$$

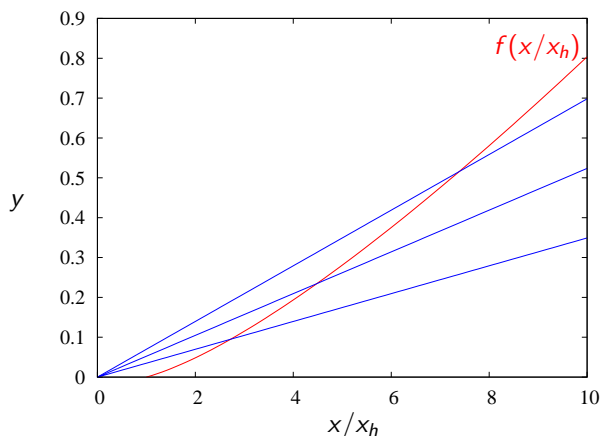where $x_h$ is a scaling factor given by the intersection of $f(x)$ with the horizon $f(x_h) = 0$.



Figure 7.1: Sketch of the geometry of a surface $f(x)$ which is hit by all trajectories $y = x\tan\alpha \,(\forall\alpha)$ at the same angle $\gamma$. Here $\gamma = 2°$ and $\alpha = 2°, 3°, 4°$ are displayed.

Since the problem is centrosymmetric, one can rotate $f$ around the origin (which is the same as changing $x_h$).

The intersecting point is obtained by

$$
\begin{aligned}
\gamma x \ln\left[\frac{x}{x_h}\right] &= x \tan\alpha \\
\gamma \ln\left[\frac{x}{x_h}\right] &\approx \alpha \\
x(\alpha) &= x_h \exp\left[\frac{\alpha}{\gamma}\right]
\end{aligned}
$$

A possible application is the *simultaneous* use of such a device as frame overlap filter and polariser. For the **low-pass for** $\lambda$ the ideal coating is Ni with $R = 1$ for $q < q_{Ni}$. The (idealised) cut-off angle is then given by

$$
\sin\gamma = q_{Ni}\,\frac{\lambda_{max}}{4\pi}
$$

Below the Ni coating a polarising SM can be deposited with

$$
m = 4\pi\,\frac{\sin\gamma}{\lambda_{min}\,q_{Ni}} = \frac{\lambda_{max}}{\lambda_{min}}
$$

For the present parameters $\lambda \in [5, 9.4]\,\text{Å}$ one gets $\gamma \approx 1°$, and $m_{SC} < 2$. Assuming $\Delta\theta = 1.5°$ and a minimum distance of the device from the point-source of 300 mm the total length is $300\,\text{mm} \cdot \exp[1.5°/1°] \approx 1\,400\,\text{mm}$. These numbers are obtained for a point source. For a finite source they increase.

**prototype**      A polarised based on the principle mentioned above was designed and build for the test-*Selene* set-up at PSI. The rather short distances and the relatively large virtual source with a height of 1 mm resulted in a split assembly.

The device was designed at the Laboratory for Neutron Scattering, PSI, and manufactored by SwissNeutronics.

The technical parameters are $\lambda \in [4, 16]\,\text{Å}$, and $x \in [170, 395]\,\text{mm}$, with $x$ the distance from the focal point. The upper limit is given by the entrance of the prototype *Selene* guide at $x = 400\,\text{mm}$. The divergence to be covered is $\Delta\theta = 1.8°$. The polarising coating is a $m = 4.2$ FeCoV / Ti:N supermirror, covered with Ni to act as a low-pass for $\lambda < 16.8\,\text{Å}$, simultaneously.
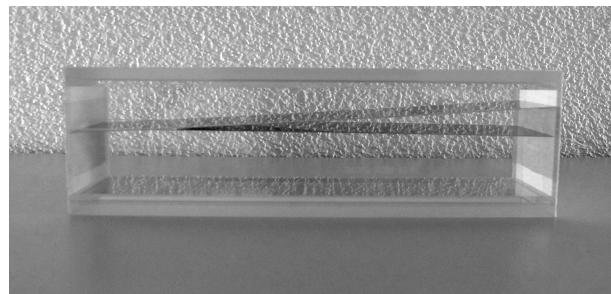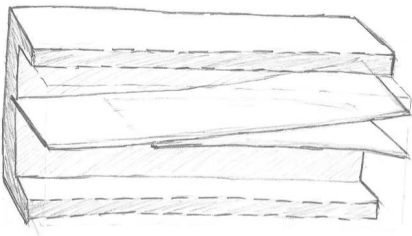


Figure 7.2: Left: First sketch for a frame-overlap filter and polariser for the *Selene* prototype set-up, based on transmission/reflection throgh/at spiral-curved surfaces. Right: Final device, produced by SwissNeutronics. The glass tube is 215 mm long and has an inner height and width of $50 \times 50\,\text{mm}^2$. The virtual source is to be 170 mm before the entrance (to the left).
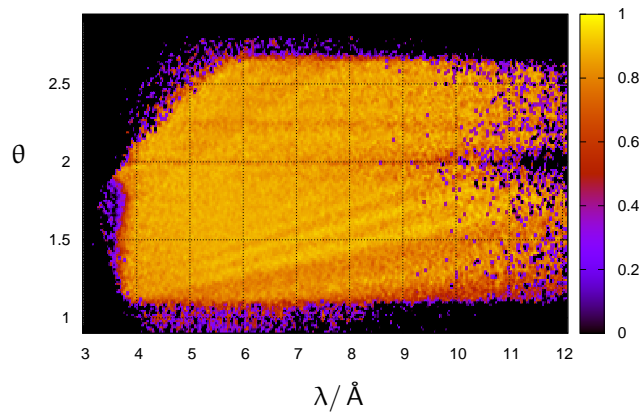
Figure 7.3: Measured polarisation efficiency of the beam filtered by the transmission polariser, transmittet throgh the *Selene* guide, and *analysed* by a remanent FeCoV/Ti:N supermirror on glass ($10 \times 10\,\text{mm}^2$, $m = 3$). The magnetisation of the analyser was performed with a permanent magnet by hand, i.e. not under optimal conditions. No spin-flipper was available for this test. The brighter diagonal lines in the map reveal inperfections in the analyser coating. The cut-off at $\lambda \approx 4\,\text{Å}$, $\theta \approx 2.5°$ corresponds to the critical edge of the analyser coating. Imperfections of the polariser should result in horizontal lines, so they can not be distinguished from imperfections of the guide. This map tells that the polariser has an efficiency of at least 90% over an angular range of $1.6°$ for a source opening of $1\,\text{mm}$.

## 7.2 condenser

A convergent beam can be transformed into a parallel beam by deflection on the outer side of a parabolically shaped surface, where the foci coincide. In analogy with light optics this device is called *condenser*, here.

The function for a parabola with the focal point at (0,0), a horizontal axis, and the opening to negative $x$ is

$$y = \sqrt{p^2 - 2px} \tag{7.2.1}$$

$p$ defines the curvature of the parabola, $p/2$ is the distance of the apex from the focal point. The incoming neutron trajectories (pointing to the focal point) are

$$y = x \tan\alpha \tag{7.2.2}$$

with $-90° < \alpha < 0°$. Both functions intersect at

$$
\begin{aligned}
\sqrt{p^2 - 2px} &= x \tan\alpha \\
x^2 \tan^2\alpha + 2px - p^2 &= 0 \\
x &= \frac{-2p \pm \sqrt{4p^2 + 4p^2 \tan^2\alpha}}{2\tan^2\alpha} \\
&= \frac{p}{\tan^2\alpha}\left(-1 \pm \sqrt{1 + \tan^2\alpha}\right) \\
&= \frac{p}{\tan^2\alpha}\left(-1 - \frac{1}{\cos\alpha}\right) \tag{7.2.3} \\
y &= \frac{p}{\tan\alpha}\left(-1 - \frac{1}{\cos\alpha}\right) \tag{7.2.4}
\end{aligned}
$$
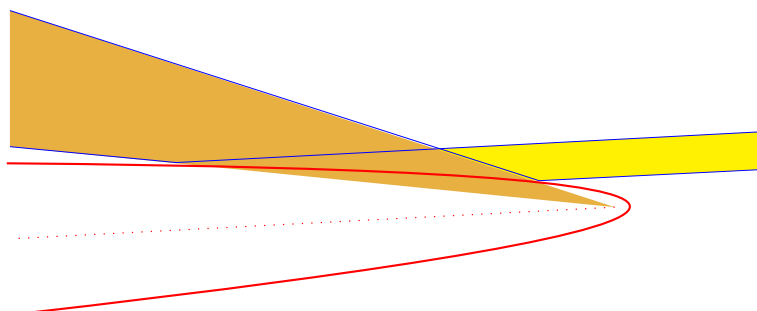


Figure 7.4: Sketch to illustrate the path of rays for a condenser-like optics based on a parabolically bent, reflecting surface. The incoming convergent beam (gold) is deflected on the surface (red) and forms a parallel beam (yellow).

It was used that only intersections before the focal point ($x < 0$) are of interest. For a given distance $x$ and angle $\alpha$ the parameter $p$ can be obtained from eqn. 7.2.3:

$$p = \frac{x \tan^2 \alpha}{-1 - 1/\cos \alpha} \tag{7.2.5}$$

The direction of the parallelised beam is given py the parabola axis. The width can be tuned by changeing $p$ and thus the distance from the focal point where the deflection occurs.

**example**      To make a convergent beam with $\Delta\theta = 1.5°$ parallel with a beam width of 26 mm the deflector extends from $x = -2\,000$ mm to $x = -500$ mm, and it has a shape defined by $p = 0.686$. The angle of incidence on the deflector varies from $0.75°$ to $1.50°$. This corresponds to a SM coating of $m = 3$ for $\lambda \geq 5$ Å.

**GISANS**      Such a condenser can be used for GISANS measurements, where a low-divergent beam is needed. The actual divergence of the beam behind the condenser depends on the spot size at the focal position, and on the degree of compression. The latter is a result of Liouville's theorem which states $\Delta y \times \Delta\theta = $ constant.

To make the beam parallel in both directions, two subsequent devices (analogue to a Kirkpatrick-Baez mirror), or a nested device (Montel Optics) can be used. The first approach allows to used individually tunable surfaces (adaptive optics) so that beam width and divergence can be adjusted to the sample.

# 8   Boundary Conditions and Consequences

Based on information distributed at IKON3, and on private communications with P. Bentley, K. Anderson, and H. Wacklin, 11. 2012, there are the following boundary conditions to be expected for a *short* reflectometer. Short means of the order of 50 m long or less, i.e. situated in one of the inner guide halls at the ESS.

## 8.1   space

- The first 2 m around the moderator are free of any elements.

- Within the target monolith shielding (2 to 6 m) an insert of horizontally a 5° wedge, but less that 210 mm, and vertically of 210 mm can be freely shaped. Optical elements are allowed in the insert. Since there will be a cooled He atmosphere (from moderator up to the end of the monolith) also free-standing Si-wavers can be used.

    The last 500 mm of the monolith might be occupied by a shutter (which can host optical elements).

- Behind the monolith there might be a chopper or other moving parts.

- From the monolith up to a radius of 15 m a common shielding for all instruments will be build. The beam guide can be of any shape and size. There is the option to insert choppers and other devices (most likely accessible from top).

- At a distance larger than 15 m to the moderator, the individual instrument guide shielding starts. Its length depends on the dose rate caused mainly by fast neutrons (also by secondary processes).

- The *short* instruments will have a 10° wedge-shaped space available. This is necessary to allow for sufficient shielding to prevent cross-talk of background.

- The height differences from moderator to floor are 3 m and 2 m. The hall allowing for high magnetic fields will have the 2 m distance. If needed it is possible to get a lower floor locally.
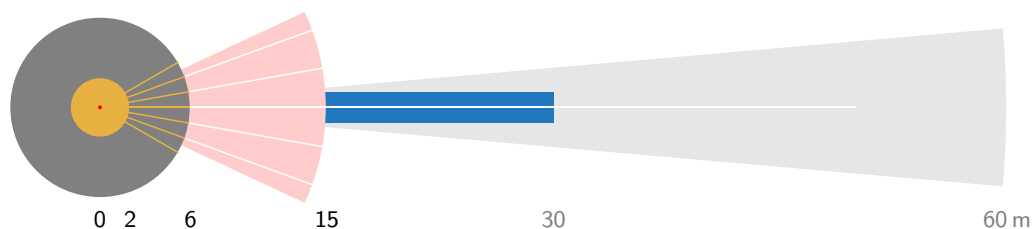


Figure 8.1: Sketch to illustrate the various shielding jackets intended for the source and the instrument. The colours mean: red–moderator, yellow–He-atmosphere, gray–target-shielding, light red–common instrument shielding, blue–individual guide-shielding (as far as possible), light gray–10° wedge available for a short instrument.

## 8.2    shielding and background

- The target monolith (for the moment) is intended to consist of steel.

- The common instrument shielding will be made of various materials to moderate fast neutrons, convert muons and neutrons, and absorb $\gamma$ and neutrons.

- The effective direct line of sight from any point of the instrument area to the moderator and target is to be avoided. This means at least 12 m material in the direct line.

  At most half of the length of the guide (shielding) is to have direct line of sight.

- Indirect line of sight has to be avoided. I.e. from outside the shielding no area directly illuminated by the source (moderator and target) is visible. Here the thickness of the shielding material is about 2 m?

Based on these constrains it might be favourable to substitute the one *Selene* guide section as presented in section 2.2 for two identical sections of half the lengths. Direct line of sight is blocked much earlier and the joining focal point is in an environment of low radiation allowing for easy access.

## 8.3    exclusion of proton prompt

At ISIS second target station and at the SNS the fast neutrons and hard x-rays produced during the proton pulses (or by secondary processes in the shielding) cause problems in the data acquisition. The corresponding STAP members R. Dalgliesh and J. Ankner suggest not to collect data during these times. So it is favourable to tune the instrument length and $\lambda$-range in a way to exclude the pulse times without creating holes in the $q$-range.

For the time being all reflectometers should be developed in a way that the time interval of high fast neutron background is excluded from the measurements.

Following the argumentation of section 2.5.1 the usable wavelength range for reflectometry starts at about 4 Å to 5 Å for *Selene* guides. An instrument length of some 60 m results in a wavelength range of e.g. $\lambda \in [5, 10]$ Å. For the ESS baseline parameters this has the consequence that the background burst from the proton pulse appears at the be beginning or the end of the used wavelength range. Further optimisation leads to the situation that the bursts are just outside the required $\lambda$ range, as is sketched in figure 8.2.
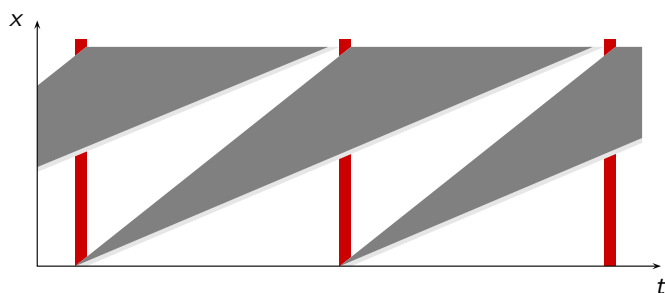


Figure 8.2: Sketch to illustrate how to avoid the influence of the $\gamma$ and fast neutron burst from the proton pulse hitting the target. The sketch is to scale with period $T = 70$ ms, pulse length $t = 3$ ms, and a sample detector distance of 58 m, i.e. $\lambda \in [5, 9.3]$ Å.

For this scheme, the flight times for the shortest / longest wavelength are $t = 73$ ms / 137 ms (assuming a burst time of 3 ms and a period of 70 ms). For $\lambda_{\mathrm{min}} = 5.00$ Å this leads to an instrument length of $\overline{SD} = 58'400$ mm, and this in turn to $\lambda_{\mathrm{max}} = 9.38$ Å.

### 8.3.1    intrinsic resolution

The intrinsic $\lambda$ resolution for this instrument is given by the length of the flight path $X$, and the pulse length $\tau$ via

$$
\begin{aligned}
\frac{\Delta\lambda}{\lambda} &= \frac{\Delta t}{t} \\
&= \frac{\tau}{2.53 \cdot 10^{-4}\,\mathrm{s\,m^{-2}}\,X\,\lambda} \\
\Delta\lambda &= 3\,956\,\mathrm{m^2\,s^{-1}}\,\frac{\tau}{X} \\
&\approx 0.2\,\text{Å} \qquad \text{for } X = 58.4\,\mathrm{m},\ \tau = 2.85\,\mathrm{ms}
\end{aligned}
$$

This leads to

$$\frac{\Delta\lambda}{\lambda} \quad = \quad 4.0\% \ldots 2.1\% \quad \text{for} \quad \lambda = 5\,\text{Å} \ldots 9.4\,\text{Å}.$$

# 9   Technical Details

## 9.1   moving elements

This section gives a preliminary list of translation and rotation stages, sorted by location and purpose. All motion devices besides the guide positioning and alignment are also listed in table 9.1 with estimated ranges, accuracy, and load.

| | motion | range | accuracy | load | moment |
|---|---|---|---|---|---|
| apertures | $y$ translation | $0 - 80\,\text{mm}$ | $< 1\,\text{mm}$ | 20 kg | |
| within ellipses | $z$ translation | $0 - 80\,\text{mm}$ | $< 1\,\text{mm}$ | 20 kg | |
| | $y$ translation | $0 - 80\,\text{mm}$ | $< 0.1\,\text{mm}$ | 2.0 kg | |
| | $z$ translation | $0 - 80\,\text{mm}$ | $< 0.1\,\text{mm}$ | 2.0 kg | |
| beam definition | $x$ translation | $0 \ldots 40\,\text{mm}$ | $< 0.1\,\text{mm}$ | 2 kg | |
| | $z$ translation | $\pm 20\,\text{mm}$ | $< 0.1\,\text{mm}$ | 5 kg | |
| | tilt | $\pm 5°$ | $< 0.01°$ | 10 kg | |
| | roll | $\pm 5°$ | $< 0.01°$ | 15 kg | |
| | $x$ translation | $\pm 20\,\text{mm}$ | $< 0.01\,\text{mm}$ | 20 kg | |
| | $y$ translation | $\pm 20\,\text{mm}$ | $< 0.01\,\text{mm}$ | 25 kg | |
| | $\omega$ | $0° \ldots 360°$ | $< 0.002°$ | 30 kg | |
| | $2\theta$ | $\pm 2°$ | $< 0.01°$ | | $10^6\,\text{Nm}$ |
| | $x$ translation | $\pm 100\,\text{mm}$ | $< 0.1\,\text{mm}$ | 0.5 t | |
| | $y$ translation | $\pm 100\,\text{mm}$ | $< 0.1\,\text{mm}$ | 0.5 t | |
| fast aperture | $y^+$ translation | $0 \ldots 80\,\text{mm}$ | $< 0.01\,\text{mm}$ | 1.0 kg | |
| | $y^-$ translation | $0 \ldots 80\,\text{mm}$ | $< 0.01\,\text{mm}$ | 1.0 kg | |
| | $z^+$ translation | $0 \ldots 80\,\text{mm}$ | $< 0.1\,\text{mm}$ | 1.0 kg | |
| | $z^-$ translation | $0 \ldots 80\,\text{mm}$ | $< 0.1\,\text{mm}$ | 1.0 kg | |
| sample stage | $z$ translation | $\pm 20\,\text{mm}$ | $< 0.1\,\text{mm}$ | 0.6 t | |
| | tilt | $\pm 5°$ | $< 0.01°$ | 0.7 t | |
| | roll | $\pm 5°$ | $< 0.01°$ | 0.7 t | |
| | $x$ translation | $\pm 20\,\text{mm}$ | $< 0.01\,\text{mm}$ | 0.8 t | |
| | $y$ translation | $\pm 20\,\text{mm}$ | $< 0.01\,\text{mm}$ | 0.8 t | |
| | $\omega$ | $0° \ldots 360°$ | $< 0.002°$ | 1.0 t | |
| | $2\theta$ | $-5° \ldots 140°$ | $< 0.01°$ | | $2 \cdot 10^5\,\text{Nm}$ |
| | $x$ translation | $\pm 500\,\text{mm}$ | $< 0.1\,\text{mm}$ | 1.5 t | |
| | $y$ translation | $\pm 500\,\text{mm}$ | $< 0.1\,\text{mm}$ | 1.5 t | |
| CCD camera | $z$ translation | $0 \ldots 400\,\text{mm}$ | † $< 0.01\,\text{mm}$ | 10 kg | |

Table 9.1: Parameters for motion control, sorted by locations and purpose., For beam manipulation and sample stage a classical set-up using rotation and translation stages was assumed. † only end-position.

## 9.2    detector characteristics

According to Richard Hall-Wilton, ESS, it is realistic to expect the following parameters:

| resolution: | $0.5 \times 0.5\,\text{mm}^2$ | minimum |
|---|---|---|
| size: | $500 \times 500\,\text{mm}^2$ | maximum |

As consequence the highest resolution at $q = 0.01\,\text{Å}^{-1}$ with a sample-detector distance of 6.2 m, limited by the detector is

$$
\begin{aligned}
\Delta\theta &= \text{arctan}[0.5/6200] \\
&\approx 0.005° \\
\theta &= 0.43° \quad \text{for } \lambda_{\text{max}} = 9.4\,\text{Å} \\
\Delta\theta/\theta &= 1.1\%
\end{aligned}
$$

Since the length of the flight path is optimised to avoid the proton pulse time it is not advisable to change the sample-detector distance. So it could be mounted on a $2\theta$ arm of fixed length, with a evacuated, frustum-shaped nozzle pointing towards the sample.

**size** A width of 500 mm results in an angle range of 4.6°. This is three times the maximum divergence of the beam incident on the sample. The excess area in the scattering plane is needed for off-specular measurements: When using $\lambda$-$\theta$ encoding, the specular beam scans over the inner 1.5°, so that effectively only another $\pm 1.5°$ are available.

Normal to the scattering plane the maximum area of interest is 170 mm wide, only. So the expected minimum detector size is

$$
\begin{aligned}
\text{width} \quad y &= 500\,\text{mm} \\
\text{height} \quad z &= 170\,\text{mm}
\end{aligned}
$$

**resolution** In the scattering direction (i.e. horizontally) a high resolution is required. Ideal would be a pixel-size of 0.5 mm or less. The lower limit is given by the effective sample size of a fraction of a mm.

Normal to the scattering plane (vertical) a much coarser resolution can be accepted. In an ideal case no position sensitivity is needed at all. A real effect that might still require some resolution are the suppression of background *outside* the region of interest. And also to align the *roll* of the sample (tilt around the *x*-axis) a 2-dimensional detector would be favourable. But this task could also be performed with an optional CCD-camera.

$$
\begin{aligned}
\text{horizontal} \quad \Delta y &\leq 0.5\,\text{mm} \\
\text{vertical} \quad \Delta z &\in [\Delta y, \infty]
\end{aligned}
$$

**rate per pixel** Since the pixel size is not defined, here the maximum rate per mm² is given. It was obtained by assuming a perfectly reflecting reference sample of $10 \times 10\,\text{mm}^2$ and full beam divergence (i.e. the reference for normalisation as discussed in section **??**). The rate per pixel varies in the range

$$
\begin{aligned}
10^5\,\text{s}^{-1}\text{Å}^{-1}\text{mm}^{-1} &\quad \text{for} \quad \lambda = 5\,\text{Å} \\
3 \cdot 10^4\,\text{s}^{-1}\text{Å}^{-1}\text{mm}^{-1} &\quad \text{for} \quad \lambda = 9.4\,\text{Å}
\end{aligned}
$$

**total rate** This quantity was obtained by simulation with the same setting as mentioned above, but by integrating over the full detector. The maximum specularly illuminated area is $2.7 \cdot 10^4\,\text{mm}^2$, but the illumination is not homogeneous. The maximum integral rates are

$$
\begin{aligned}
5 \cdot 10^8\,\text{s}^{-1}\text{Å}^{-1} &\quad \text{for} \quad \lambda = 5\,\text{Å} \\
2 \cdot 10^8\,\text{s}^{-1}\text{Å}^{-1} &\quad \text{for} \quad \lambda = 9.4\,\text{Å}
\end{aligned}
$$

**homogeneity**The detector images are normalised by division by a reference measurement. Already a relative mis-alignment of $0.005°$ leads to a shift of one ($0.5\,$mm) pixel. It is thus crucial that the detector area is homogeneous (if necessary after pixel-wise normalisation) on the order of 1%.

**stability**The intended measurement scheme requires a reference for each detector image obtained with a sample. To save measurement time, there will be a set of reference sample sizes and orientations available, obtained with standard samples. This requires that the homogeneity of the detector does not change with time (over months), and that the total sensitivity can be detected continuously, so that a renormalisation of the reference is possible.

**dynamic range**The dynamic range of the detector must be quite high since at the same time one can expect maximum flux on some area of the detector, while it drops by 6 orders of magnitude (or more) for high-$q_z$ or off-specular regions. This can be seen in figure 2.7.

A signal of $10^{-8}$ relative to the full intensity given by a *small* sample should be measurable. Small here means 2 orders of magnitude smaller than the reference mentioned above. The signal will then be of the order $5 \cdot 10^8 \times 10^{-2}\,10^{-8}$. Thus the integral noise of the detector should be below $10^{-2}\,\mathrm{s}^{-1}$.

# 10 Measurement Schemes and Data Reduction

This chapter is in a fragmentary state. The samples are not yet completely defined (suggestions are welcome!) — and thus there are no definite simulations.

The process of data acquisition and processing described below is based on experience with measurements using the prototype set-up on BOA and on Amor, both at PSI. Where these are not available, the description states what is intended to be done.

This chapter gives a more detailed description of the data collection and processing for the three principle operation modes and three types of samples.

[→10.1] An organic film at the $Si/D_2O$ interface in a solid/liquid cell, measured in the almost conventional mode.

[→10.2] A NiTi multilayer with (artificial) off-specular scattering, measured with $\lambda$-$\theta$ encoding.

[→10.3] A small ferromagnetic sample, measured in the high-intensity specular mode.

## 10.1    conventional mode, solid-liquid cell

Liquid samples typically show a high diffuse scattering. This means that one has to choose an operation mode where diffuse scattering does not strongly affect the specular signal, and where it can be measured to some extend to allow for correction. This is why the combination liquid cell / almost conventional mode is chosen, here.

Measurements using a sold-liquid cell imply the constraint that the footprint has to avoid the sealing regions of the cell.

### 10.1.1    the sample
The sample is an organic film on Si, measured against $D_2O/H_2O$.

|  |  |  |
|---:|:---|:---|
| Si | $\infty$ | SLD |
| $SiO_2$ | 20 Å | |
| $\sigma$ | 2 Å | |
| film | 50 Å | |
| $\sigma$ | 2 Å | |
| $D_2O/H_2O$ (9:1) | 0.2 mm | |

The incoherent scattering from H in film and solvent is taken into account.

### 10.1.2    the measurement scheme
This mode corresponds to the conventional TOF reflectometry, where the beam divergence and footprint size are defined by slits. The angle of incidence and the divergence are constant over the pulse. Using the *Selene* guide the footprint defined by the slit system at the virtual source point. For adjusting the divergence one slit behind the last guide element is sufficient. The still convergent beam avoids illumination of the sample environment.

Due to the analogy, the data collection, normalisation and further treatment for one angle of incidence exactly follow the procedure used with conventional TOF reflectometers.

An additional feature when using a wide divergence cut down by the slit is, that by scanning the slit in between measurements, one can change $\theta$ without rotating the sample.
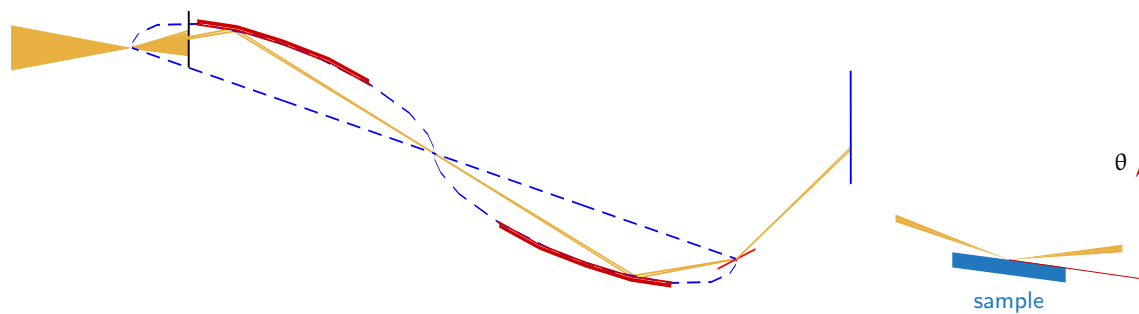
### 10.1.3    sample alignment

. The low-divergent beam caused by the slit allows to align the sample by alternating rocking scans and $z$-scans. The accuracy is given by the divergence and for larger samples by the footprint. The only difference to conventional TOF reflectometers is that the beam converging at the centre of rotation should not have any parallel components. A $z$ scan at $2\theta = 0°$ to find the absorbing substrate at the half-shaded beam is thus modified. At $\theta = 0°$ one has the end of the substrate leading to half the intensity, and not the sample centre. For small samples this can be neglected, for large samples one still gets the approximate position.

For a high precision of the alignment an additional CCD-based detector can be used. It has much higher resolution and fast feed-back (no TOF analysis is necessary).

One can use divergent white light coupled into the beam before the virtual source point. Besides gravity effects this follows the same trajectories as the neutrons, creating a spot where the centre of rotation should be. Depending on the (transparency of) the sample environment one can thus use the light to pre-align the sample. This method is used on Amor and on the *Selene* prototype with large success.

### 10.1.4    data acquisition

For the ... sample measured through Si the critical edge is at $q_z^c = ?\,\text{Å}^{-1}$. This leads to the lowest angular setting $\omega = ?°$. The corresponding $q_z$ range, slit-opening (centred in the middle of the beam), and counting times are given in table 10.1.

| $\omega$ | $q_z/\,\text{Å}^{-1}$ | $s/\,\text{mm}$ | $t/\,\text{s}$ |
|---|---|---|---|

Table 10.1: Angular settings $\omega$, the related $q_z$ range, the slit-width $s$, and the estimated counting time $t$.

The criterion for the counting time is that the highest statistical error per $\Delta q/q = 4\%$ bin is below ?%.

The measurements each lead to an array $I(y, z, t)$. In most cases (as here), there is no information expected in $y$ direction so that one can project the array to $I(z, t)$. The uncertainties are $\Delta z$ given by the detector resolution, and $\Delta t = \tau$.

### 10.1.5    reference measurement

The best normalisation can be obtained using a reference sample cell, where the film (and solvent) are replaced by a supermirror coating of known reflectivity. It is realistic to assume a $m = 10$ coating with a moderate reflectivity.

So for up to $q_z = 0.22\,\text{Å}^{-1}$ one gets the reference arrays $I_r(y, z, t)$ or $I_r(z, t)$. Correction for the known reflectivity gives $I_{rc}(z, t)$.

### 10.1.6    normalisation and integration

If required, the not specularly illuminated area of the $I(z, t)$ map can be used to estimate the diffuse background, which can then be subtracted from $I(z, t)$.

A division of $I(z, t)$ by the reference $I_{rc}(z, t)$ pixel-by-pixel gives the reflectivity of the film $R(z, t)$. This can be transferred to $R(q_x, q_z)$, or if the off-specular region can be ignored, the corresponding region of $R(z, t)$ can be projected on a $q_z$ grid with $\Delta q_z/q_z = $ const. The new $q_z$ grid should have a lower resolution compared to $R(z, t)$, which is defined by the detector resolution $\Delta z$ and by $\tau$. Here $\Delta q_z/q_z = 7\%$ is used.

### 10.1.7  discussion

...

A limiting factor for using the proposed instrument for solid-liquid-cells is the maximum footprint of $10 \times 40\,\text{mm}^2$. Larger samples will profit from an other geometry, or from a non-focusing instrument.

Within these limitations the intensities and measurement times should be almost the same on all reflectometer types, because the maximum intensity (as allowed by Liouville) is reduced by the guide transmission, only.

The diffuse background scales roughly as $A^2 \times \Delta\theta_y^2 \times \Delta\theta_z^2$, ($A$ is the sample surface) while the specular intensity scales with $A \times \Delta\theta_y \times \Delta\theta_z$. It is thus possible to increase the signal-to-background ratio by reducing any of these quantities. It has to be analysed how far this can be taken — or if the small sample surface can be compensated for by using a higher divergence.

## 10.2  $\lambda$-$\theta$ encoding, off-specular measurements

The strengths of the $\lambda$-$\theta$-encoding are the wider $q_z$ range accessible with one angular setting, the constant $\Delta\lambda/\lambda$, and eventually the *nicer* off-specular area, compared to the almost conventional mode.

This is illustrated at the example of a Ni/Ti multilayer sample with (artificial) Bragg-sheet scattering.

The high resolution $\Delta q_z/q_z = 2\%$ aimed for *here* results in much longer counting times.

### 10.2.1  the sample

The sample is a multilayer of the composition

$$[\,\text{Ni}\,(?\,\text{Å})\,/\,\text{Ti}\,(?\,\text{Å})\,]_?/\text{Si}$$

with a constant interface roughness $\sigma = 4\,\text{Å}$. The off-specular signal is *generated* using the specular reflectivity $R(q_z)$

$$R(q_x, q_z) \quad = \quad R(q_z) \cdot \exp\left[-\frac{q_x^2}{2?^2}\right]$$

with a cut-off at the sample horizon. A bending of the Bragg sheets, Youneda wings and the low-intensity region between Youneda and horizon are not produced this way. Within McStas this folding is achieved by randomly adding a $q_{xy}$ component, but with a Gaussian probability distribution centred at $q_{xy} = 0$.

### 10.2.2  the measurement scheme

A ML monochromator at or before the virtual source point encodes the wavelengths of the neutrons in the final angle of the monochromator. For small $\theta$ one gets $\theta \propto \lambda$. The specular reflectivity from the sample then leads to a diagonal streak in $I(\lambda, 2\theta)$ on the detector, so that off-specular scattering can be measured. Figure 10.1 shows *snap-shots* of the beam-distribution within the guide an at the sample.

The resolution in $q_z$ is essentially given by the ML monochromator and can reach 2%, while the TOF resolution influences $\Delta q_x$ (this has to be verified). So this mode could be realised without any chopper. The losses one gets by using a monochromator are (partly) compensated by the quasi-simultaneous measurement on a wide $\theta$-range.

For a ML with a Bragg peak at $m \cdot 0.022\,\text{Å}^{-1}$ one gets the proportionality (with $[\theta] = \text{deg}$)

$$\theta \approx 0.1\,m\,\lambda/\,\text{Å} \tag{10.2.1}$$

The guide geometry, its coating and the wavelength range define $\Delta\theta$ [$\rightarrow$6.1]. I.e. for $\lambda \in [5, 9.4]\,\text{Å}$ and $\Delta\theta = 1.5°$ one gets $m \approx 3.4$ with $\theta \in [1.7°, 3.2°]$. A plateau of total reflection ($m \leq 1$) results in $\theta \leq 1°$ for the same $\lambda$ range. Thus totally reflected neutrons do not reach the guide.

**fast moving slit**    A ML monochromator leads to an illumination of the *off-specular region* on the detector by diffuse and and off-specular scattering at the multilayer, but also by specular scattering off the Bragg condition!. This can be seen in figure 2.7. A fast moving slit before the sample can be used to filter this unwanted intensity from the monochromator. The slit scans across the beam for each pulse and thus also creates a $\lambda$-$\theta$ encoding, but without the constant resolution. In combination with the monochromator the slit keeps the off-specular region clean.
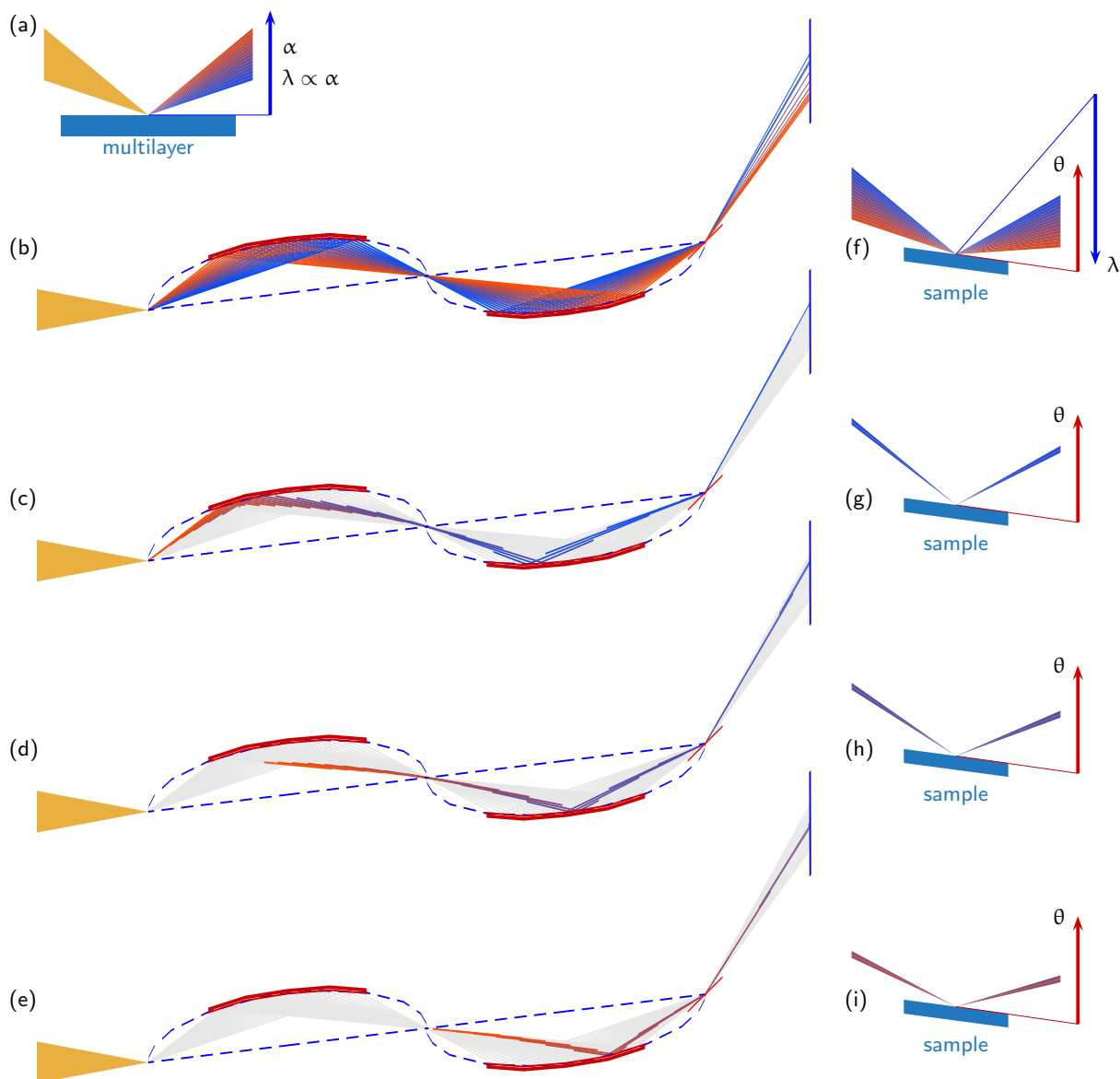
Figure 10.1: Illustration of the principle of the λ-θ encoding. A convergent white (pulsed) beam is spectrally analysed by a ML monochromator (a). The beam then propagates to the sample keeping the relation between λ and θ (b). For a pulsed beam at any time an almost monochromatic beam is impinging on the sample, where θ and λ ∼ θ vary with time. The sketches (c) to (e) show snap-shots of the beam within the *Selene* guide system and after the sample. In (f) to (i) the corresponding situation on the sample is shown.

### 10.2.3     sample alignment

The sample can be aligned by keeping the otherwise scanning slit behind the guide at a fixed position with small opening. The beam transmitted there is then well-defined, but almost monochromatic. The further procedure follows the one described above [→10.1.3].

### 10.2.4     data acquisition

Also the data acquisition follows the scheme of the almost conventional reflectometry. Only the number of $q_z$-ranges is reduced, and the counting times are increased.

table

### 10.2.5 reference measurement

For $q_z < 0.2\,\text{Å}^{-1}$ a high-$m$ supermirror with known reflectivity and same shape as the sample can be used for normalisation. For higher $q_z$ it is possible to correct the reference measurements for the footprint size. To avoid problems with detector inhomogeneities, the same detector area should be illuminated for all measurements.

### 10.2.6 normalisation and integration

The normalisation here is a bit more complicated because there is no reference sample with a well-known high-intensity off-specular scattering.

...

### 10.2.7 discussion

...

It is not yet clear if a fast slit system is available. In the worst case one could use a pair of choppers for this purpose, but they would be located quite close to the sample.

## 10.3 high-intensity specular mode, small magnetic sample

### 10.3.1 the sample

### 10.3.2 the measurement scheme

Figure 10.2: text !!!

Measurements performed on Amor with one guide, only, are shown in figure 10.3



Figure 10.3: text

### 10.3.3 sample alignment

The sample can be aligned by using the slit behind the guide at a fixed position with small opening. This is identical to the situation in the almost conventional mode and thus the scheme described there can be used [→10.1.3].

### 10.3.4 data acquisition

### 10.3.5 reference measurement

To normalise the $I(t, y, z)$ data set the best choice is to use a reference sample with the same measures (to guarantee the same footprint) and a high reflectivity over a wide $q_z$ range. As long as $R_r(q_z)$ of this reference is known, one can correct the reference $I_r(t, y, z)$ to $I_{rc}(t, y, z) = I_r(t, y, z)/R_r(t, y, z)$.

One can think of using a supermirror with $m = 10$, and reflectivity $R > 1\%$ as a reference. This would allow direct corrections up to $q_z = 0.22\,\text{Å}^{-1}$. Since each reference measurement takes some time, a set of standard sample sizes should be defined, for which the corresponding reference measurements are available. This applies also to liquid-solid cells.

### 10.3.6    normalisation and integration

In case a reference reference measurement is available (i.e. $q_z \approx 0.22\,\text{Å}^{-1}$) it s possible to normalise the measurement pixel-by-pixel to get

$$R(t, y, z) \quad = \quad I(t, y, z)/I_{\text{rc}}(t, y, z) \tag{10.3.1}$$

Summation over $y$, transformation of $t$ to $\lambda$ with $\Delta t = \tau$, and $z$ to $2\theta$ with the detector resolution $\Delta z$ gives a $R(\lambda, \theta)$ map with corresponding error-map. Each line (one $\theta$) corresponds to a reflectivity $R_\theta(\lambda)$ obtained in TOF mode, and each column (one $\lambda$) corresponds to a reflectivity $R_\lambda(\theta)$ obtained in an angle-dispersive mode.

There are various schemes to collapse the $R(\lambda, \theta)$ to $R(q_z)$. The approach we followed up to now is the define a $q_z$ grid (with $\Delta q_z/q_z =$ constant) and to fill in all entries of the $R(\lambda, \theta)$ array according to their $q_z$. This can be done with full error handling so that at the end each $R(q_z, i)$ has its own error. Since the resolution varies over the $R(\lambda, \theta)$ array, one gets a non-trivial but known resolution function for $R(q_z)$.

For higher $q_z$, where no reference is available, or its measurement would take too long, it proved to be possible to take a low-$\omega$ measurement and eventually correct for the different footprint or projected sample height. In case the detector is not sufficiently homogeneous, one has to take care to illuminate the same area on the detector for all $\omega$.

### 10.3.7    discussion

## 10.4    data reduction

### 10.4.1    raw-data and intensity maps

Each neutron detected on the position sensitive detector has the associated parameters $t$, $y$ and $z$ for the time-of-flight and the position on the detector. The detector spatial resolution gives the constant values $\Delta y$ and $\Delta z$, the pulse length sets an upper limit for $\Delta t <= \tau$. The latter one might be reduced by choppers.

From theses basic parameters and the instrument parameters $X$ (source detector distance) and $\theta_{\text{detector}}$ one can calculate the neutron wavelength [→**??**]

$$\lambda \quad = \quad \frac{h}{m_{\text{n}}} \frac{t}{X} \tag{10.4.1}$$

and the final angle after reflection

$$\theta_{\text{f}} \quad = \quad \epsilon + \omega - \arctan z \tag{10.4.2}$$

where $\omega$ is the inclination of the sample surface relative to the long axis of the last ellipse of the *Selene* guide, $z$ is the position on the detector if that one is located at $\theta_{\text{detector}} = \epsilon + 2\omega$.

Discretisation in $\lambda$ and $\theta_{\text{f}}$ of a large ensemble of events gives the intensity map $I(\lambda, \theta_{\text{f}})$ with the error-map $E(\lambda, \theta_{\text{f}}) \approx \sqrt{I(\lambda, \theta_{\text{f}})}$. The approximation is valid for more than 10 counts per bin. For less counts a correcting factor has to be taken into account. Zero counts is also a measured quantity and has to have an error. This topic has to be investigated further!

It is also possible to extract $I(q_z)$, $E(q_z)$ or $I(q_z, q_x)$, $E(q_z, q_x)$, instead. ...

### 10.4.2    normalisation

The measured intensity map $I(\lambda, \theta)$ is not only a function of $R(q_z)$ of the sample, but also of the intensity $I_{\text{sample in}}(\lambda, \theta, x, y)$. incident on it. This quantity could ideally be measured with a reference sample with $R(q) = 1$ and exactly the same shape and position as the sample. Non-perfect reflectivity can be corrected for as long as $R_{\text{reference}}(q)$ is known and homogeneous. One could e.g. use a supermirror-coated reference with $m = 10$ (and low reflectivity) to correct up to $q_z = 0.22\,\text{Å}^{-1}$.

For higher $q_z$ this approach is unrealistic. On the other side the projected sample height is larger, which leads to an averaging over beam inhomogeneities. So it might be possible to use a calculated or simulated reference. The quality of the calculation or simulation can be checked by comparison to the reference below $q_z = 0.22\,\text{Å}^{-1}$.

**integration normal to the scattering plane**The normalisation can be performed after integrating in $y$ direction on the detector, i.e. normal to the scattering plane. This is justified by

$$
\begin{aligned}
I(t, y, z) &= I(t, z) \cdot g(y) \\
\frac{\int I(t, y, z)\,\mathrm{d}y}{\int I_0(t, y, z)\,\mathrm{d}y} &= \frac{\int I(t, z)\,g(y)\,\mathrm{d}y}{\int I_0(t, z)\,g(y)\,\mathrm{d}y} \\
&= \frac{I(t, z)\int g(y)\,\mathrm{d}y}{I_0(t, z)\int g(y)\,\mathrm{d}y} \\
&= R(t, z)
\end{aligned}
$$

where $g(y)$ gives the intensity distribution in $y$ direction. By using a single detector or a 1D position sensitive detector this integration is already realised. This is the case in many conventional reflectometers.

### 10.4.3 resolution

In most cases the resolution function $f(q_z)$ with $R_e(q_z) = R(q_z) * f(q_z)$ will neither be constant nor proportional to $q_z$. It is thus dangerous to add several data sets, e.g. obtained with various $\omega$.

### 10.4.4 summation of data sets with different resolution

The summation of data sets $R_i(q_z)$ with different resolution $f_i(q_z)$ is possible, but it leads to a complicated (i.e. not single-Gaussian) resolution function:

$$
\begin{aligned}
R_\Sigma &= \sum_i a_i R_i \quad , \quad \sum_i a_i = 1 \\
&= \sum_i a_i R * f_i \\
\mathcal{F}[R_\Sigma] &= \mathcal{F}\left[\sum_i a_i R * f_i\right] \\
&= \sum_i a_i \mathcal{F}[R * f_i] \\
&= \sum_i a_i \mathcal{F}[R] \cdot \mathcal{F}[f_i] \\
&= \mathcal{F}[R] \cdot \sum_i \left(a_i \mathcal{F}[f_i]\right) \\
&= \mathcal{F}[R] \cdot \mathcal{F}\left[\sum_i a_i f_i\right] \\
&= \mathcal{F}\left[R * \left(\sum_i a_i f_i\right)\right] \\
R_\Sigma &= R * \left(\sum_i a_i f_i\right) \\
&:= R * f_\Sigma
\end{aligned}
$$

Simulation or fitting of $R(q_z)$ is possible when $f_\Sigma(q_z)$ can be estimated, and when is taken into account in the simulation software.

For publication such a reflectivity profile might not be suited because the abrupt changes in $f_\Sigma(q_z)$ at the joints can lead to peaks or dips in $R_\Sigma$.

### 10.4.5 convolution to $\Delta q/q = \text{const}$

In cases when the experimental resolution function $f_e(q)$ of one data set $R_e(q) = R(q) * f_e(q)$ is known, one can convolve $R_e(q)$ with a resolution $f_c(q)$ in a way to get $R_p(q)$ with $\sigma_p \propto q$, i.e. $\Delta q/q = \text{const} := p$. For Gaussian the relation

$$
\begin{aligned}
f_{e/c}(q) &= \frac{1}{\sqrt{2\pi}\,\sigma_{f/c}} \exp\left[-\frac{(q - q_{f/c})^2}{2\sigma_{f/c}^2}\right] \\
f_p(q) &= f_e(q) * g_c(q) \\
&= \frac{1}{\sqrt{2\pi}\,\sigma_p} \exp\left[-\frac{(q - q_p)^2}{2\sigma_p^2}\right] \qquad \text{with} \quad \sigma_p^2 = \sigma_e^2 + \sigma_c^2, \quad q_p = q_e + q_c \qquad (10.4.3)
\end{aligned}
$$

holds. For the present case $q_{e/c} = 0$. So when $\sigma^e(q)$ is known one can get the *correcting Gaussian* with

$$
\sigma_c(q) = \sqrt{p^2\,q^2 - \sigma_e^2(q)} \tag{10.4.4}
$$

with $\sigma_p = p\,q$. Avoiding $\sigma_c <= 0$ leads to the constraint

$$
p > \frac{\sigma_e(q)}{q} \quad \forall q
$$

The resulting *corrected* reflectivity curve is then

$$
\begin{aligned}
R_p(q) &= R_e(q) * f_c(q) \\
&= \int_{\bar{q}=q_{\min}}^{q_{\max}} R_e(q - \bar{q}) \cdot \frac{1}{\sqrt{2\pi}\,\sigma_c(\bar{q})} \exp\left[-\frac{\bar{q}^2}{2\sigma_c(\bar{q})^2}\right]\,d\bar{q}
\end{aligned} \tag{10.4.5}
$$

This now allows to merge several data sets after bringing them the the same resolution for each $q$ in the overlapping region. Of cause information is lost by lowering the resolution, but the resulting $R_e(q)$ and eventually a merged $R_\sigma(q)$ have the appearance expected by standard software, most of the users, and almost all readers of publications.

!!! Besides the resolution of the data imposed by the experiment and the data analysis, there is the resolution of the representation of the data, I.e. the spacing of the nodes. To be able to distinguish peaks in $R(q_z)$, already convoluted with the final resolution function $f(q)$, one has to .....

From $\delta q$ (FWHM) to $\sigma$:

$$
\exp\left[\frac{q_{1/2}^2}{2\sigma^2}\right] = 0.5 \tag{10.4.6}
$$

$$
\begin{aligned}
q_{1/2} &= \sqrt{2\ln 2}\,\sigma \tag{10.4.7} \\
\Delta q &= 2\,q_{1/2} \tag{10.4.8} \\
&\approx 2.3548\,\sigma \tag{10.4.9}
\end{aligned}
$$

## off-specular and incoherent scattering

If the $I(\lambda, 2\theta)$ map obtained with a beam of large divergence is to be converted into $R(q_z)$ one assumes that all non-specularly reflected intensity can be neglected. Depending on the sample, the $q_z$ range, and the dynamic range one measures, this might not be the case.

The specular intensity measured at a certain $2\theta$ does not depend on the beam divergence (provided it is sufficiently large to illuminate the sample at an angle $\theta$). The diffuse scattering for a given angle of incidence $\theta$ spreads over all $2\theta$ so that the *incoherent background* for a certain $2\theta$ is proportional to $\Delta\theta$. Off-specular scattering leads also to background, but with a different characteristics. Figure 10.4 illustrates this effect.

A consequence is that samples with a high contribution of incoherent background can not be measured with a wide divergence. Or more general, whenever crosstalk of the incoherent scattering attributed to $\theta$ into a
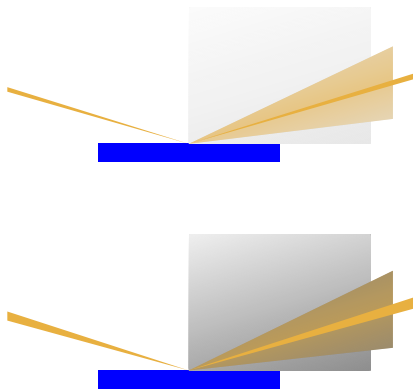
Figure 10.4: *Top*: A convergent beam with divergence $\Delta\theta$ impinging the surface under $\theta$ leads to specular scattering around $2\theta$ with the same divergence. In addition a fan of off-specular scattering and a (non-flat) background from incoherent scattering is created. *Bottom*: A doubling of $\Delta\theta$ also doubles the total intensity of the specular contribution, but the incoherent background scales with 4 (2 times the incoming divergence and 2 times the detector angle). The off-specular contribution scales somewhere in between 2 and 4, depending on how fast it fades off away from the specular condition.

detection channel occurs, where specular scattering form an other $\theta$ is expected. This also holds for all kinds of multi-beam approaches.

The question is now, if one can use the *Selene*-type guide also for (almost) conventional measurements. We have performed test measurements with a liquid/solid sample cell, where the interface is illuminated through a thick Si-block of 100 mm length. Due to the insufficient quality of the reference measurement for normalisation, it is not possible to extract high-quality $R(q_z)$ curves from these measurements. But it is still possible to estimate the reduction of the incoherent background by using a slit behind the elliptic guide.

Figure 10.5: Maps of $\log_{10}[I(\lambda, \theta)]$ taken with the liquid/solid interface cell with Si vs. $D_2O$. *Left*: with a beam of $\Delta\theta = 1.1°$ for 2 orientations $\omega = -0.7°$ and $\omega = 0.3°$. *Right*: The same geometries, but with a beam reduced to $\Delta\theta = 0.11°$ by a diaphragm behind the guide.

Figure 10.5 shows $I(\lambda, \theta)$ maps for the cell filled with $D_2O$ with a divergence of $\Delta\theta = 1.1°$, and of $\Delta\theta = 0.11°$, respectively. The incoherent scattering can be clearly seen for $\Delta\theta = 1.1°$ in the range $\lambda \approx 3\ldots8\,\text{Å}$, fading for longer $\lambda$. The reason for the fading is the width of the time-bin varying with $\lambda$. The bright triangle in the upper left map corresponds to the total reflection plateau, the streaks in the maps on the left are the specularly reflected beams. The maps for the low-divergent beam shows a strongly reduced background, which hardly affects the specular signal.

# 11   Prototype

## 11.1    design considerations

The prototype was designed to operate in a λ- and θ-range close to what can be expected for a reflectometer at the ESS, paying respect to the beam characteristics and spacial constraints at BOA (**??**) and Amor (11.4.1).

- length of the focusing section ($= 4c$): The available space at BOA is some 9 m. About 3 m are needed to get an acceptable angular resolution on the detector ($\Delta\theta \approx 0.04°$). Another 1.5 m before the first focal point are required for the ml-monochromator, the chopper and eventually further equipment. This led to $4c = 4$ m.

- divergence: The divergence was chosen to be slightly larger than what is available at BOA or Amor, i.e. $\Delta\theta = 1.8°$.

- ellipse parameters: The effective length was defined to $\xi = 0.60$, leading to $b/a = 0.021480$.

- λ-range: The λ-range was selected based on the considerations made in (**??**) to be $\lambda \in [3.8, 12]$ Å. This results in a coating with $m = 4$.

- sample size: For $c = 1$ m and the typical $b/a \approx 0.02$ the maximum spot size with only small influence of coma aberration is $1 \times 1$ mm$^2$. Larger spots are possible, but the footprint the is no longer homogeneous.

- chopper speed and pulse length: To cover the required λ-range in time-of-flight with a possible chopper-detector distance of some 8 m one needs a frequency of $\approx 60$ s$^{-1}$. The chopper opening-to closing time ratio is the same as for the ESS pulses, i.e. 0.04.

## 11.2    devices

Most of the following devices were designed, constructed and fabricated at PSI. The exceptions are the X95 elements, the precision slit and the guide elements.

### 11.2.1    pulse chopper

The reduced length of the set-up compared to the ESS dimensions with about the same λ range leads to shorter repetition rate and pulse length for the test set-up. The pulse chopper will operates with up to 60 Hz, its open/closed time ratio is about 5% (to be determined exactly). The chopper disc has 2 openings.

The much reduced dimension of the beam relative to conventional set-ups leads to a disc diameter of $\varnothing = 160$ mm. The absorbing material is 2.2 mm of an Al :$^{10}$B alloy, followed by 2 mm Cd. The absorbing region is 10 mm wide. Figure 11.1 shows on the left side the pulse chopper after assembling, before testing.

The pulse chopper is equipped with a !!! to trigger the TOF data acquisition. Since this system detects each gap opening of the chopper, no correction for the second gap and eventually an phase error is needed.

### 11.2.2    frame-overlap chopper

The frame overlap chopper has similar dimensions as the pulse chopper, but a open/close time ratio of 50%. Its position is at or close to the intermediate focal point of the *Selene* guide system. The frequencies and phases of pulse- and frame-overlap-choppers can be locked. The frame overlap chopper is the left device in figure 11.1.
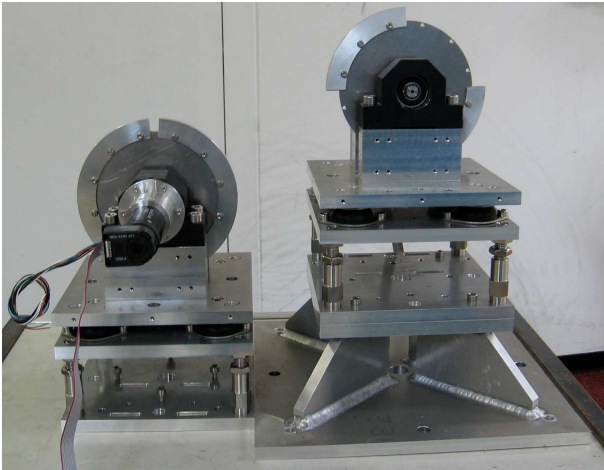
Figure 11.1: Pulse chopper (left) and frame overlap chopper (right) for the *Selene* prototype.

### 11.2.3    precision slit

The small dimensions of the prototype results in a down-scaling of the sample and thus of the slit at the first focal point. The beam cross section is of the order $0.1 \times 1\,\text{mm}^2$. This will be realised with a precision x-ray slit system, equipped with BorAl and Cd absorbers. The slit is custom made by ACS and based on their system STT-100-20.

During the experiments on BOA the slit failed several times. In the end it could not be used other than for defining a fix opening of approximately $0.5 \times 1\,\text{mm}^2$.

### 11.2.4    double multilayer monochromator

The double multilayer monochromator consists of 2 borcron glass substrates, coated with a Ni/Ti multilayer with a first order peak at $m = 3$ with $\Delta q/q = 7\%$. The surfaces are mounted parallel face to face with a gap of 6.5 mm. The first substrate is 305 mm long, the second 119 mm. In $x$ direction there is a 5 mm gap in between both. The design is optimised for a slit positioned 43 mm behind the end of the device. The acceptance is $\Delta\theta = 1.8°$ for $\lambda \in [4, 10]\,\text{Å}$.

The device was tested and characterised on Amor. Since the divergence available for this test was only of the order of $0.3°$, the full angular range was reached by tilting the monochromator in discrete steps. Figure 11.2 shows the resulting $I(\theta, \lambda)$ map. The width of the intensity streak shown here is limited by the measurement range, not by the device.

To characterise $\Delta\lambda/\lambda$ and the off-specular scattering, also measurements were performed with a well collimated beam (slits of 1 mm opening, 100 mm and 2200 mm from the entrance of the device). The $I(\lambda)$ curves for various $\theta$ is shown in figure 11.3.

Figure 11.4 shows the off-specular scattering for $\lambda = 6.3\,\text{Å}$ with various slit positions and openings behind the device. The slits before the ml-monochromator are 1 mm each. Surprisingly there is the same broad diffuse background with an exponential decay for all measurements. The origin is unclear yet, but eventually this is a feature of the detector.

### 11.2.5    sample holder

The sample holder is simply an Al cuboid with grooves and slits to insert (glue) the sample and some absorbing sheets. It is mounted on a $y$ and $z$ translation stage.

### 11.2.6    guide support

The guide support system is assembled from X95 profiles and joints, motorised and manual translation tables and manual tilting stages. Figure 11.5 shows the mounting frames for the single guide elements (figure 11.7), the height and tilt-adjustments and the X95 bar where upon the guide elements are mounted. This bar is positioned on tilting- and translation stages, which are to be mounted to the lower rotation stages of the BOA tables 3 and 4, respectively.
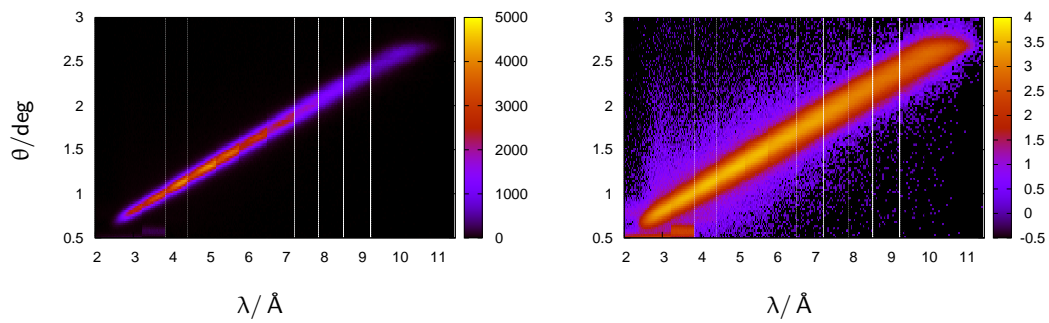
Figure 11.2: $I(\lambda, \theta)$ on linear (left) and logarithmic scale (right) obtained with the ml-monochromator on Amor. The maps are stitched together from 11 measurements since the incoming divergence was limited to $0.3°$.
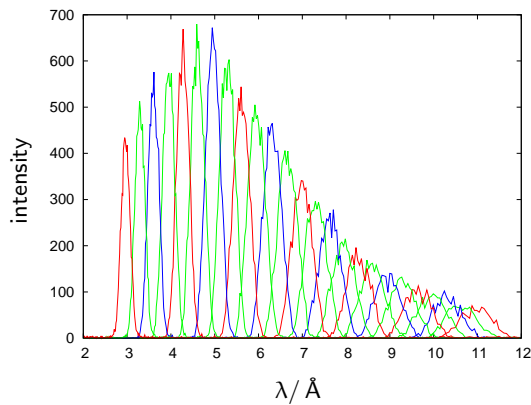


Figure 11.3: $I(\lambda)$ for $\theta = 0.5°, 0.6°, \ldots 3.0°$. The varying height of the individual scans reflects the $\lambda$-dependence of the intensity of the incoming beam.
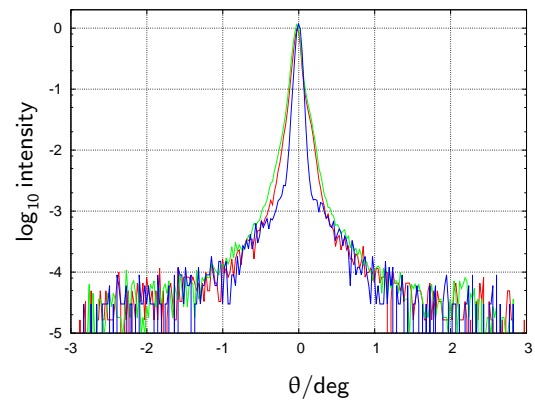
Figure 11.4: $\log_{10}[I(\theta)]$ without aperture behind the device (green), with a $0.5\,mm$ aperture at $50\,mm$ (red), and with a $1\,mm$ aperture at $1300\,mm$ (blue).

### 11.2.7     guide system

The *Selene* guide system in this case consists of 2 sections focusing elliptically in two dimensions (i.e. in $y$ and in $z$), where each section consists of 2 mirror-inverted elements of $600\,mm$ length. Figure 11.7 shows one guide element before mounting.

The device was constructed and build by SwissNeutronics according to the measures $c = 1000\,mm$, $b/a = 0.021480$, $\xi = 0.60$, coating Ni/Ti with $m = 4$. The horizontally reflecting glass substrate has a constant height of $46\,mm$. The vertically reflecting glass has one straight edge along the optical axis, and one elliptically curved edge, fitting the horizontal reflectors shape. The vertical reflector has a minimum width of $21\,mm$.
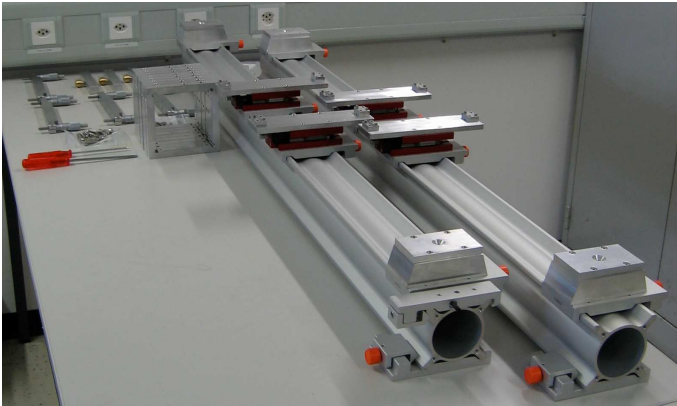
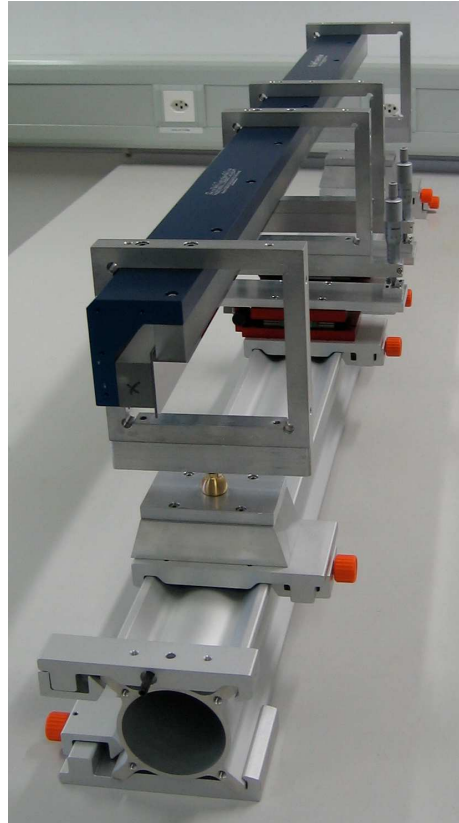Figure 11.5: Parts of the guide support before mounting the guide elements.



Figure 11.6: Guide support with 2 guide elements mounted. Shown is the second guide of the *Selene* set-up, reflecting left and downwards. The guides are not yet adjusted, the knife blade slit is missing.



Figure 11.7: Single guide element (half a guide section). The blue part is an L-shaped Al bar on which the glass substrates are screwed. The Al frames are for mounting the elements on the support and alignment system.

## 11.3    experiments on BOA

The *Selene* prototype was first set up and tested on the beamline BOA at SINQ, PSI, in August and September 2012. The team members for this campaign were U. B. Hansen, T. Panzner, and J. Stahn.

The intensity available at BOA together with the high background limited strongly what could be measured. Since both, chopper and ML-monochromator have a transmission of ca. 5%, only, it was not possible to operate them simultaneously for TOF λ-θ-encoding.

In the meantime (11. 2012) the background could be reduced by almost 2 orders of magnitude, so further tests on BOA are scheduled for December 2012 and for 2013.

### 11.3.1    BOA

(by U. Filges)

BOA stands for "*b*eam line for neutron *o*ptics and other *a*pplications" and is operated by the Neutron Optics group within the Laboratory for Development and Methods at PSI. [U. Filges, Swiss Neutron News, **40**, 4 (2012)] The beam line is a 18 m long instrument located at beam-channel 51 looking at the SINQ cold source which delivers a neutron spectrum from 1.5 Å to 20 Å. The guide section contains a supermirror bender unit inside the SINQ biological shielding. Thus the beam is permanently polarised in vertical direction.

The flexible space is 12.5 m long (n-flight path) and 3.5 m wide. Where the first part is occupied by an anti-trumped within a concrete shielding. The instrument is equipped with 5 $x$-translation tables on an optical bench, where the 3 latter are motorised and hold each a $y$-translation stage. On theses platforms optional $\omega$ and $2\theta$ rotation stages, goniometers, and further translation stages can be mounted. An area sensitive CCD camera system, a $^3$He neutron counter system, and a $^3$He area detector (EMBL) are used for data acquisition. Figure 11.8 shows the essential components of the beamline with the *Selene* prototype set-up in place.

### 11.3.2    set-up

All components were mechanically ready by mid August 2012. The installation on BOA started on 13. August. In parallel the motorised components were commissioned and integrated into the instrument control system (translation devices, slit system) or operated as stand-alone solutions (choppers).

First the complete set-up was realised using the instruments LASER for the mean beam direction and the instruments light source giving a white divergent light to align the guide elements. *Figure of merit* at the beginning was to achieve a symmetric, small light spot at the focal points, and a homogeneous, gap-free light distribution on the detector. The first requirement could be fulfilled rather easily (the spot at the sample
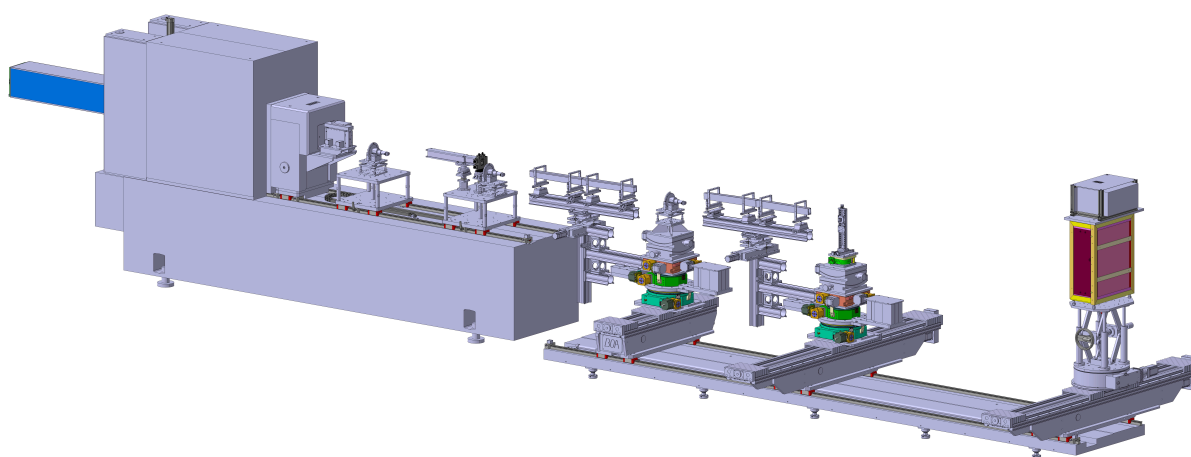


Figure 11.8: Assembly drawing of the construction of the *Selene* prototype set-up on the test facility BOA at PSI. The elements/devices from left to right:  n-guide of BOA; pulse chopper on table 2; double ml monochromator, precision slit, pulse chopper (alternative position) on table 3; first guide section on support system, attached to table 4; frame overlap chopper on table 4; second guide section on support system, attached to table 5; sample holder on $yz$ translation stage on table 5; and area detector on table 6.

position is almost identical to the one defined by a pin-hole). The second task proved to be more complicated since the light source produced a highly structured beam, covering mis-alignments. Thus in a later stage a high-power LED with a reflector (bicycle front light) was used in front of the pin-hole.

### 11.3.3 experiments in TOF mode

The choppers were operated at $1800\,\mathrm{min^{-1}}$, i.e. with a pulse rate of $60\,\mathrm{s^{-1}}$. The phase of the frame-overlap chopper was chosen to select $\lambda \in [2, 13]\,\text{Å}$.

**characterisation of the beam**

The beam characteristics behind the precision slit was measured with the area detector $5100\,\mathrm{mm}$ behind the slit in TOF mode. Due to the bender section in the BOA neutron guide the divergence is strongly patterned in horizontal direction. Reflections on sidewalls (anti-trumpet) and on roof and bottom lead to the higher divergence contributions. In between there is a low-intensity gap. Figure 11.9 (a) and (b) shows the intensity
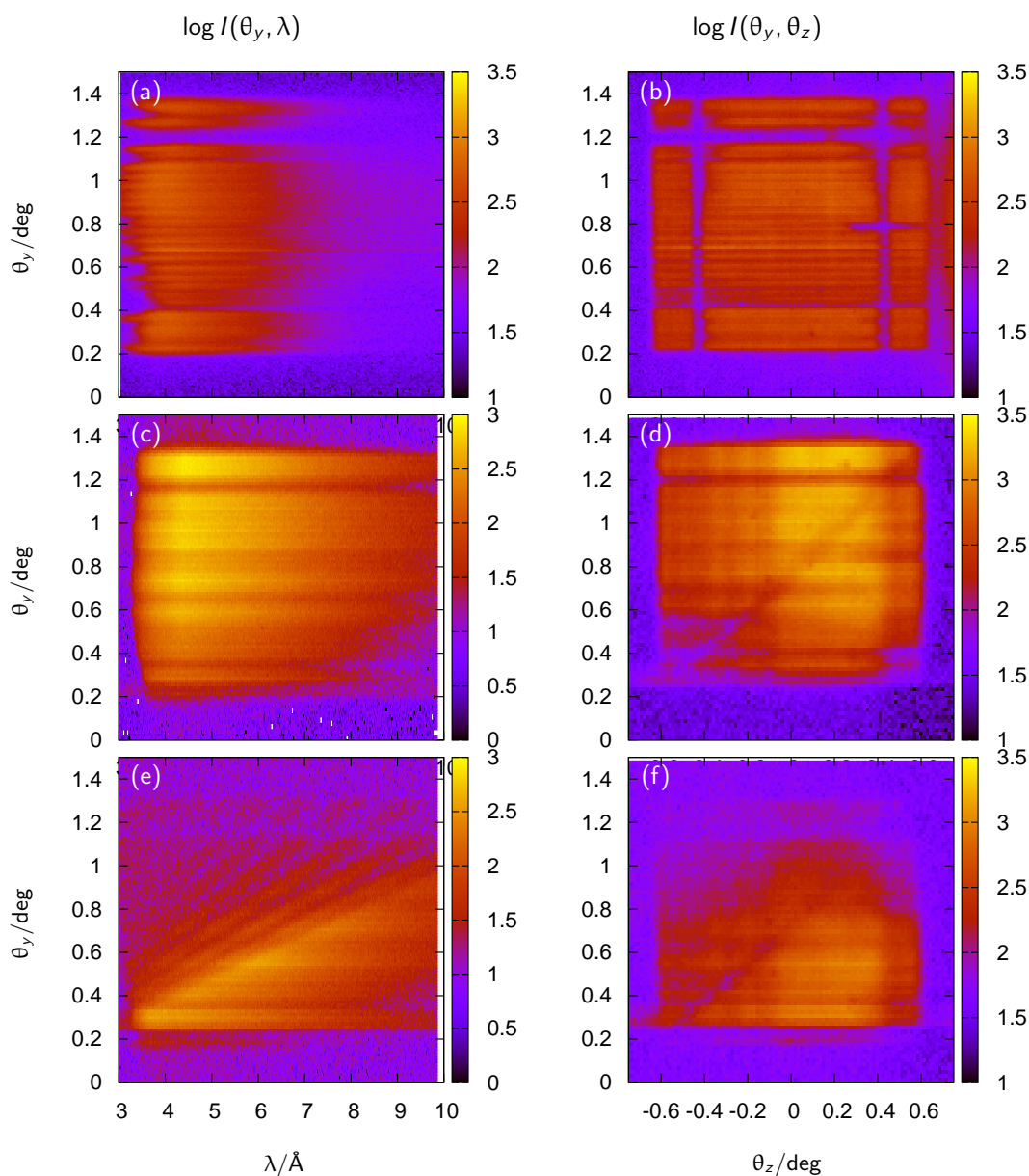


Figure 11.9: Intensity maps $\log I(\theta_y, \lambda)$ and $\log I(\theta_y, \theta_z)$ for the beam emerging from the precision slit (a) and (b), after the *Selene* guide being reflected by a $m = 5$ Ni/Ti supermirror (c) and (d), and being reflected by a $1000\,\text{Å}$ thick Ni film on glass (e) and (f).

maps $I(\theta_y, \lambda)$ and $I(\theta_y, \theta_z)$, obtained from the TOF data by integrating horizontally, or over time. The dark horizontal area in (b) on the right side results from a mechanical damage in the bender section. The horizontal high intensity streak at $\theta_y \approx 0.7°$ is a feature of the area detector.

Map (a) shows the strong $\lambda$ dependence of the primary intensity. The $I(\lambda)$ depends also on where the individual channels of the bender point towards the moderator.

The large dynamic range of $I(\lambda)$ here is attenuated by the 4 reflections in the *Selene* guide, which mainly affect short wavelengths.

**reflection of a $m = 5$ supermirror**

For normalisation of the beam reflected off a sample, a similar measurement using a supermirror can be used. Available are such references with a Ni/Ti supermirror coating of $m = 5$ with area $1 \times 2\,mm^2$, $3 \times 3\,mm^2$, and $10 \times 10\,mm^2$.

Figures 11.9 (c) and (d) show intensity maps similar to the ones mentioned above, but this time measured using the *Selene*-guide. The sample was the $10 \times 10\,mm^2$ SM, the beam size was 1 mm high and 0.5 mm wide. This means that the sample was illuminated completely along the neutron beam direction. The diagonal dark streak visible in figure 11.9 (d) originates from the areas of the *Selene* guide elements where the horizontal and the vertical reflector join. Tiny errors in the surface quality and the shape of the substrates (caused by the cutting process) leads to a lower reflectivity there. This is inherent to the Montel-type optics. For larger guide systems this feature will be much weaker since the absolute width of the distorted area stays the same, while the guide dimensions get much larger.

The stripe pattern visible in both maps has several origins: besides the inhomogeneities imposed by the beam characteristics of BOA, there are imperfections of the guides (waviness) and more severe, inhomogeneities of the area detector.

The low-intensity region in 11.9 (d) in the lower left corner is a feature of the *Selene* optics: the coma aberration is corrected for in space, but in momentum space some inhomogeneities remain.

**reflection of a $1000\,Å$ thick Ni film on glass**

As a sample the reference for characterising and adjusting the TOF reflectometer Amor was used: a $1000\,Å$ thick Ni film on glass. Figures 11.9 (e) and (f) show the corresponding intensity maps. The *triangle* below the diagonal in map (e) is caused by total reflection off the Ni film. Thus it looks similar to the same region in map (c). The fan-like structure corresponds to the Kiessig fringes. Each horizontal line can be seen as a TOF measurement of a range of the reflectivity curve, where $\theta_y$ acts as a scaling factor. But also each vertical line represents a reflectivity measurement, this time in angle-dispersive mode for a given $\lambda$.

To obtain a reflectivity curve, the intensity map from the sample has to be divided pixel-by-pixel by the reference measurement (here with the SM). The result is shown in figure 11.10 (a). Then $I(\theta_y, \lambda)$ is transferred to $I(\theta_y, q_z)$ on an (here) equidistant $q_z$ grid to give map (b). Then each horizontal line is normalised so that the total reflection plateau is at $I = 1$. The horizontal stripes still visible in map (c) have 2 origins: e.g. the prominent line at $\theta_y \approx 1.2°$ results from the division of noise by noise in the angular region where (nearly) no intensity is available. The sharper lines result from inhomogeneities of the detector. The maps have not been measured on exactly the same area of the detector, but were shifted by some pixels. Thus the normalisation did not correct for different efficiencies of the detector.

The reflectivity curve in Figure 11.10 (d) was obtained by a wighted summation over the $\theta_y$-channels. No error-handling was applied so far with the consequence that the noise form the region $\theta_y \approx 1.2°$ dominates the curve at high $q_z$. In this graph only 5 Kiessig fringes are clearly visible, while in the maps on can count 7. This means a more accurate data analysis will provide a better $R(q_z)$ curve. But still the background sets a limits at about $10^{-3}$. This is why the experiment is going to be repeated on the TOF reflectometer Amor, which reaches $10^{-5}$ for small samples ($5 \times 5\,mm^2$) in a reasonable time in *normal* operation.

### 11.3.4 experiments with angle-wavelength encoding

For these measurements the chopper was stopped (in the open position), and the double ML-monochromator was installed before the precision slit. Measurements analogue to the ones discussed in 11.3.3 were performed. But in this case the inhomogeneities of the detector prevent the calculation of $R(q_z)$, thus a repetition is planned where it is made sure that both maps, from the sample and from the reference, are collected on exactly the same area on the detector.
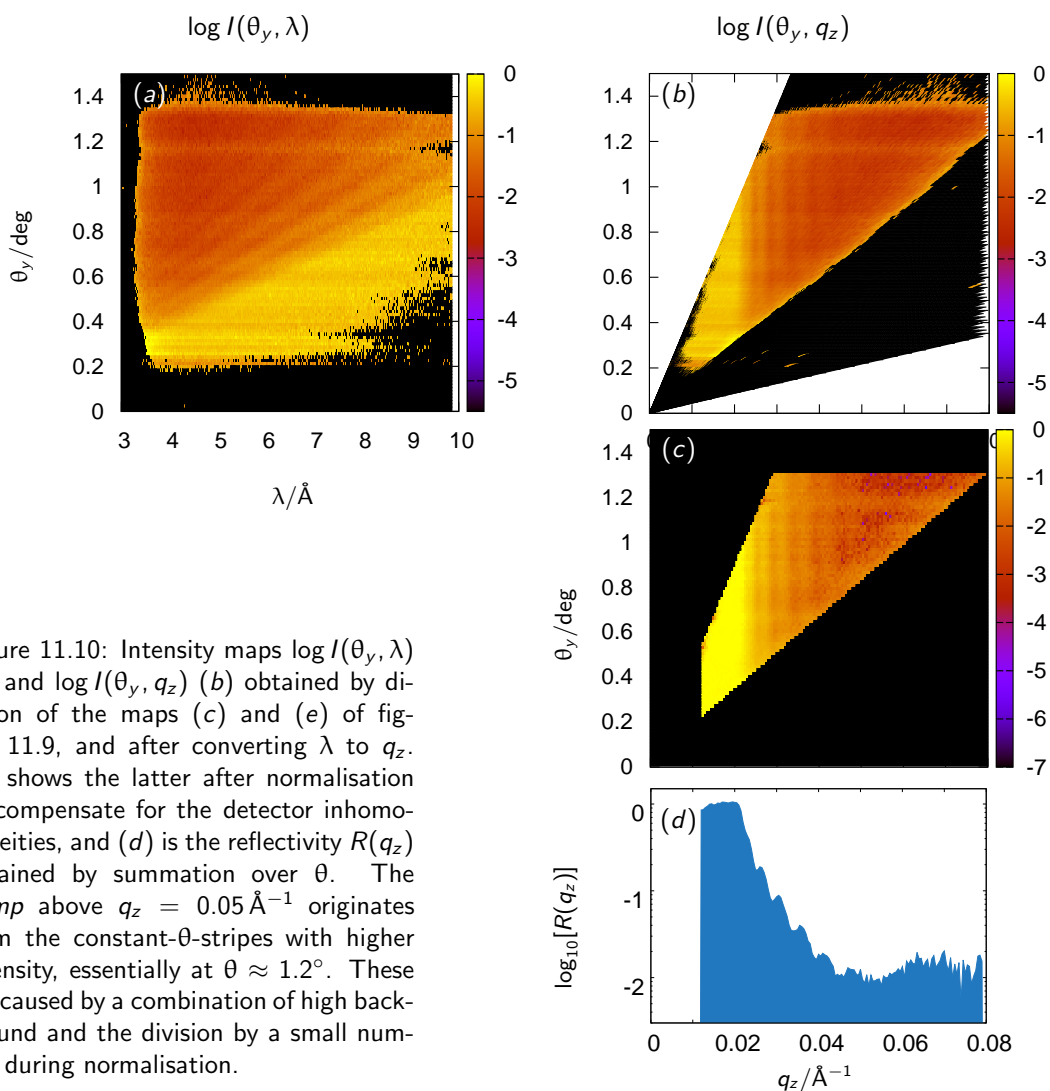
log $I(\theta_y, \lambda)$                 log $I(\theta_y, q_z)$

Figure 11.10: Intensity maps log $I(\theta_y, \lambda)$ (a) and log $I(\theta_y, q_z)$ (b) obtained by division of the maps (c) and (e) of figure 11.9, and after converting $\lambda$ to $q_z$. (c) shows the latter after normalisation to compensate for the detector inhomogeneities, and (d) is the reflectivity $R(q_z)$ obtained by summation over $\theta$. The *bump* above $q_z = 0.05\,\text{Å}^{-1}$ originates from the constant-$\theta$-stripes with higher intensity, essentially at $\theta \approx 1.2°$. These are caused by a combination of high background and the division by a small number during normalisation.

**reflection of a** $m = 5$ **supermirror** data analysis not completed

**reflection of a** $1000\,\text{Å}$ **thick Ni film on glass** data analysis not completed

### 11.3.5  use of a diffusor

One can use the *Selene* guide to create a small virtual source far from the moderator. This might be of interest e.g. for an imaging beam line. In this case the beam emerging from the last focal point should have a homogeneous $I(\theta_x, \theta_y)$ distribution. Since in the present case the source is inhomogeneous (see figure 11.9 (b)) also the divergence after the *Selene* guide is. For the intensity map shown in figure 11.11 a $2\,\text{mm}$ thick graphite plate was positioned at the focal point instead of the sample.

data analysis not completed

### 11.3.6  discussion

The intended program for the first beamtime on BOA was too ambitious. Instead of the measurement of $R(q_z)$ of a reference sample in all principle operation modes (with chopper, with ML monochromator, using both), only the chopper mode was at least partly completed.

The main problems are not connected to the *Selene* guide but result from the experimental environment and the equipment:

- High background caused by fast neutrons coming down the guide, and by thermal neutrons from the neighbouring imaging beamline ICON.
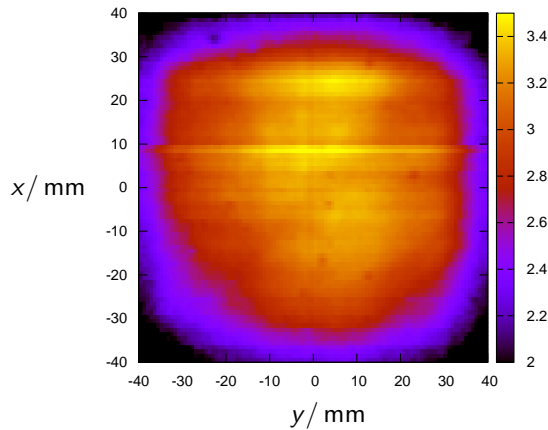
Figure 11.11: Intensity map $I(x, y)$ measured in direct view to the *Selene* guide with a 2 mm thick graphite plate at the sample position, acting as a diffusor. The distance from the graphite to the detector was 3200 mm. The bright horizontal stripe at $x \approx 9$ mm originates from a defect of the detector (electronics?).

$\rightarrow$ In the meantime the background could be lowered by 2 orders of magnitude. The improvements on shielding are based on the measurements within this campaign.

• Inhomogeneous sensitivity of the $^3$He area detector.

• Inhomogeneous beam profile and divergence of the beam leaving the BOA guide.

$\rightarrow$ This can be reduced by installing a graphite diffusor before the initial slit.

• Surprisingly low intensity.

On the other side it proved to be quite simple to align the guide elements using a (homogeneous) white light source before the initial focal point.

**guide quality**The overall quality of the guide is very good. Compared to the first elliptically focusing guide produced for Amor there is a huge progress made by SwissNeutronics.

• Still there is some waviness visible, where the *propagation of the waves* is parallel to the neutron beam direction.

$\rightarrow$ The effect is so small that it hardly affects the data analysis.

• The two substrates for the horizontal and the vertical reflecting part of one guide element do not form exactly a 90° angle.

$\rightarrow$ This prohibits a simultaneous perfect alignment of the guide elements in both directions. An improvement is possible.

• At the region where two elements join the reflectors do not exactly follow an elliptic shape, leading to a reduced intensity coming from there.

$\rightarrow$ This should be improved. Off-situ analysis using light is planned to identify the real shape.

**measurements**

• For the chopper-only mode the inhomogeneities mentioned above play a minor role. Essentially they just lead to a reduction of the intensity. So in this case the measurements have been successful in a sense that a reflectivity curve could be measured. Limitations were imposed by the long counting time and the high background limiting the dynamic range.

- Using both, chopper and ML-monochromator was not successful: The much too low intensity even prohibited to align the sample.

- The data obtained with a ML-monochromator only, are not yet analysed completely. But since there the inhomogeneities of the beam and the detector directly influence the resolution and the λ-θ encoding, it will be no surprise if the data analysis fails.

**outlook**Further tests of the *Selene* prototype on BOA are planned beginning of December.

SwissNeutronics will improve the alignment of the reflectors within one guide element.

## 11.4    experiments on Amor

### 11.4.1    Amor

Amor is a neutron reflectometer at SINQ, PSI [32], which allows for a wide range of set-ups The scattering geometry is vertical so that liquid surfaces are accessible. Most components are positioned on an optical bench which allows to play with the resolution, or to test exotic set-ups like the prism approach by R. Cubitt [29] or the *Selene* concept. In general Amor is operated in time-of-flight mode (realised by a double chopper), but it is also possible to run it with a monochromator.

The ML-monochromator is placed on the frame-overlap mirror stage and can be driven out of the beam.

The chopper is positioned in a housing, some cm behind the end of the neutron guide. It consists of 2 discs, 490 mm apart, each with 2 openings of 13.6°. In general it is operated in a way to give $\Delta\lambda/\lambda = \text{const}.$[33] For the tests we used a pulse frequency of $23.\bar{3}$ Hz (corresponding to 700 rpm).

The chopper housing limits the maximum incoming divergence because it leads to a minimum distance between the end of the guide to the first diaphragm of 1500 mm, and to the first place where to put a monochromator (on the frame overlap filter stage) it is some 1800 mm.

Behind the chopper housing and the 1$^{st}$ diaphragm a frame overlap filter is mounted. It consists of Si-wafers of 0.6 mm thickness, coated with a Ni/Ti $m^f = 2$ SM. If placed in the beam with an inclination of $\theta^f$ it reflects all neutrons with $\lambda > 4\pi \sin\theta^f / m^f q_{Ni}^c$. In the case of the strongly divergent beam the deviation of $\alpha^f$ from $\theta^f$ has to be taken into account. The cut-off wavelength is then $\lambda^f = 4\pi \sin(\theta^f - \theta)/m^f q_{Ni}^c$.

In TOF mode (without monochromator) the situation is more complicated: All neutrons trajectories accepted by the elliptic guide should provide all required wavelengths. But the flat frame-overlap filter acts angle dependent. A possible solution is to build a filter bent accordingly [→**??**]. This then is optimised for one specific cut-off wavelength.

### 11.4.2    high intensity specular reflectometry

A principle sketch of this mode is given in **??**. The standard disc choppers of Amor were used, operated at 750 rpm, giving a pulse rate of $25\,\text{s}^{-1}$. The first slit after the chopper housing was used to define the initial beam size. All other slits were removed or driven out of the way. The distance from the sample position to the detector was 3000 mm. No frame-overlap filter was installed.

The samples were (a) a $[\text{La}_{1/3}\,\text{Ca}_{2/3}\,\text{Mn}\,\text{O}_3\,/\,\text{Y}\,\text{Ba}\,\text{Cu}\,\text{O}_3]_5$ multilayer on $\text{Sr}\,\text{Ti}\,\text{O}_3$ with a period of 600 Å and a layer thickness ratio of $2:1$. As reference to normalise the measurements and to characterise the beam (b) a NiTi supermirror with $m = 5$ was used. Both samples had a surface area of $10 \times 10\,\text{mm}^2$.

Figure 11.12 shows the intensity maps $I(\lambda, \theta)$ for both samples, and for the re-normalised map. The reflectivity extracted there from is displayed in figure 11.13. The measurement times for the maps shown were 4 h, each, at an angle $\omega = 1.5°$. The same measurements were performed also in 24 min and in 2.5 min, and at higher angles.

In map 11.12 (a) the iso-$q_z$ lines for the first, second and fourth Bragg peak and for the total reflection edge are nicely visible. The dark line at $\theta \approx 0.9°$ originates from a mis-alignment of the guides. This just leads to a reduced intensity, not to systematic errors. Since these measurements and the data reduction were performed with a constant $\Delta\lambda \propto \Delta t$ while the instrument has a resolution $\Delta\lambda/\lambda = \text{const}.$, the resolution at low $q_z$ is underestimated, and at high $q_z$ a coarser binning could be performed without loss of information, which would qualify the error-bars.

| fixed values | / | mm |
|---|---|---|
| guide end – chopper housing start | : | 75 |
| guide end – chopper housing end | : | 1309 |
| guide end – earliest position polariser | : | 2744 |
| 1$^{st}$ slit – earliest position polariser | : | 1242 |
| typical values | | |
| chopper disc 1 – chopper disc 2 | : | 490 |
| 3$^{rd}$ slit – sample | : | 400 |
| sample – 4$^{th}$ slit | : | 400 |

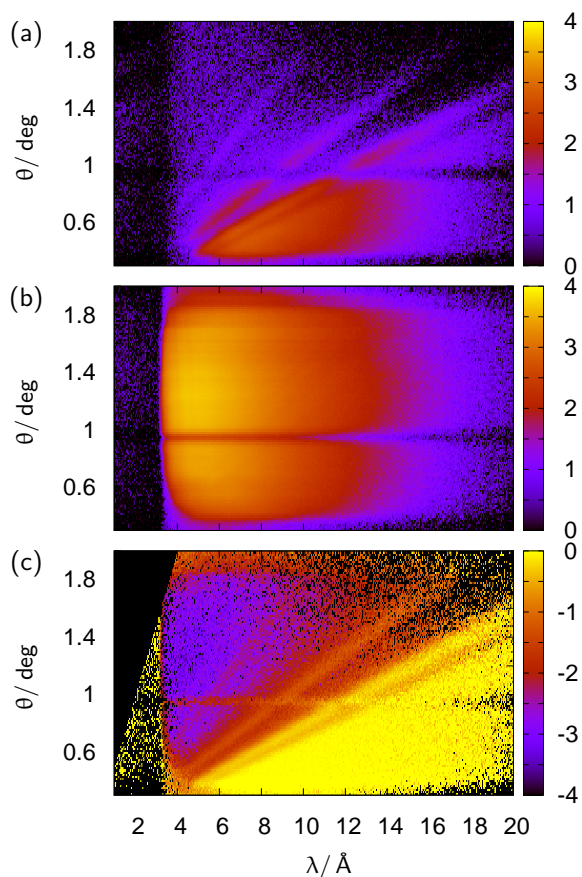Table 11.1: List of typical or fixed distances on Amor.

(a)

(b)

(c)

Figure 11.12: Intensity maps $\log_{10}[I(\lambda, \theta)]$ measured in 4 h with a LCMO/YBCO multilayer (a), and a NiTi supermirror (b). From these map (c) is obtained by division. (d, blue line) Reflectivity curves $R(q_z)$ obtained by summation over equal $q_z$ of the map (c). The red and green lines correspond to counting times of 24 min and 2.5 min. The differences visible at $q_z \approx 0.3\,\text{Å}^{-1}$ originate form a not yet correct treatment of the errors of zero-count channels.

(d)

Figure 11.13: Reflectivity of a LCMO/YBCO multilayer. The blue curve is identical to the one in figure 11.12 (d), the others were obtained in a similar way with $\omega = 3°$ (red), and $\omega = 4°$ (green). The resolution was reduced accordingly. The deviations clearly illustrate the influence of the $\lambda$-dependent background.
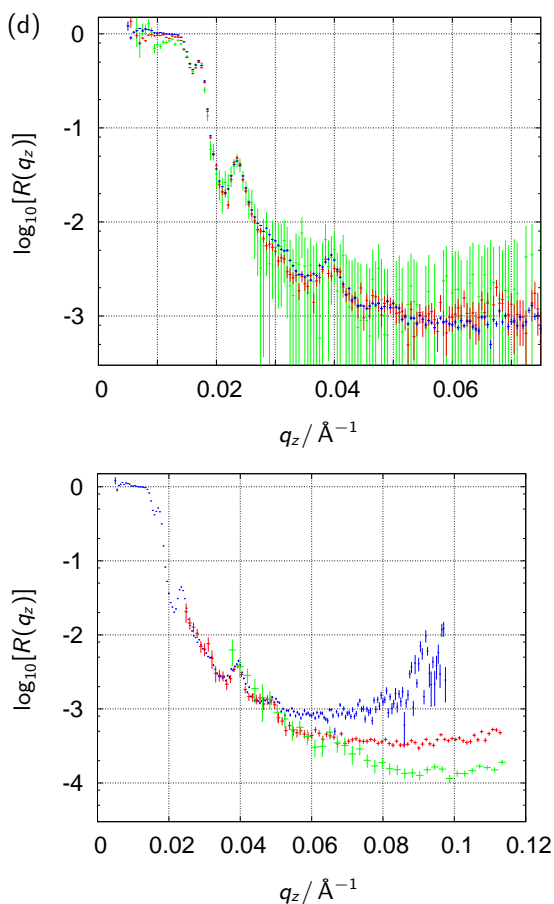
The fact that $R(q_z)$ reaches the background at $10^{-3}$, already, has two reasons: No frame-overlap filter was used, so that the totally reflected neutrons with $\lambda > 24\,\text{Å}$ leak in at nominally $\lambda > 4\,\text{Å}$. This leaking can be seen in the maps at $\lambda < 3.5\,\text{Å}$. And more severe, the instrument background is highest for $\lambda \approx 5\,\text{Å}$. This is visible in map (a) for $\theta > 1.8°$. In principle this can be suppressed, but the improvised set-up and the horizontal offset of the beam prevented the usage of the slits and shielding material available on Amor. Both problems will be solved for the next beamtime.

## 11.4.3    angle-wavelength encoding

In addition to the operation mode described in 11.4.2 a multilayer monochromator ($\rightarrow$ 11.2.4) is installed after the chopper. As a consequence the first slit on Amor could not be used anymore and was replaced by a manual slit system behind the monochromator. Unfortunately, the chopper was operated at 1500 rpm and with a non-adequate time binning scheme. This results in half the intensity for $\lambda < 6.8\,\text{Å}$. The samples where
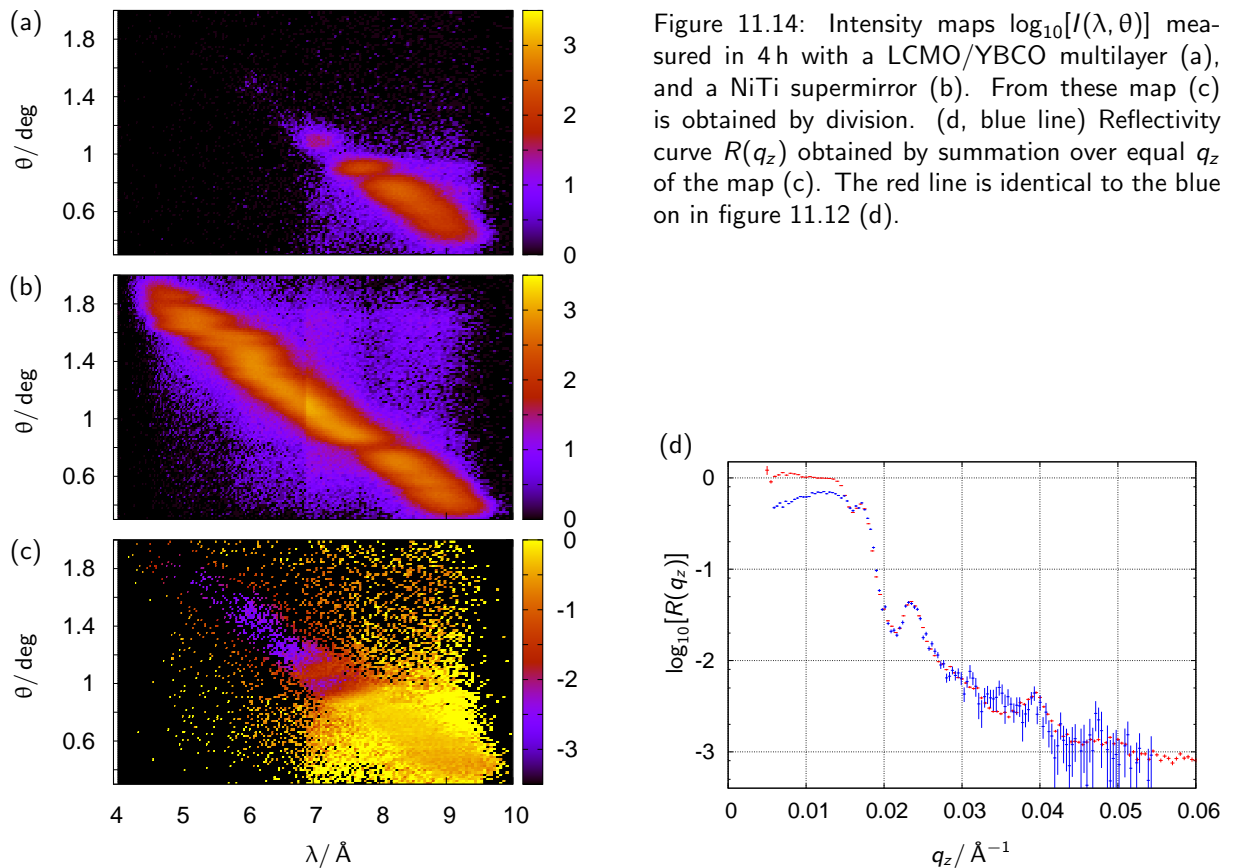
(a)

(b)

(c)

(d)

Figure 11.14: Intensity maps $\log_{10}[I(\lambda, \theta)]$ measured in 4 h with a LCMO/YBCO multilayer (a), and a NiTi supermirror (b). From these map (c) is obtained by division. (d, blue line) Reflectivity curve $R(q_z)$ obtained by summation over equal $q_z$ of the map (c). The red line is identical to the blue on in figure 11.12 (d).

the same LCMO/YBCO multilayer and NiTi supermirror discussed above.

The resulting reflectivity is compared to the one obtained with the height-intensity mode in figure 11.14 (d). The much reduced statistics displays the intensity gain one gets by loosening the resolution and using a high divergence. In addition for $q_z > 0.03\,\text{Å}^{-1}$ the mentioned mismatch of chopper speed and time binning leads to a further reduction of the statistics by a factor 2.

The deviation of $R(q_z)$ for small $q - z$ results from problems with the normalisation. Most likely the positions of both samples where not exactly identical, leading to a slightly different illumination. This is most severe for low angles, where the projected sample size might be smaller than the position off-set.

### 11.4.4    discussion

Overall the test series on Amor was successful, for it proved that even delicate samples can be measured. The gain in counting time relative to the normal operation mode on Amor is about one order of magnitude for small samples. This value was estimated from the actual counting time, the illuminated sample area, and the difference of the chopper speeds.

The measurements also revealed the problems still present. The different beam geometry requires adapted shielding and modified slit mounts to reduce background. This was already realised by end 2012.

The horizontal stripe pattern visible in the intensity maps results from a misalignment of the guide elements and from waviness on the reflecting surfaces. The relative alignment of the guides can be improved. Mechanical modifications are being discussed with SwissNeutronics. For the waviness the problem is more difficult to solve. We found area on the surface, almost free of detectable waviness, and area with severe deviations. It is planned to investigate this qualitatively and to find solutions together with SwissNeutronics. The waviness leads to distortions in the angle-wavelength encoding and thus to a reduced resolution in this operation mode. For the other modes it just results in a reduction of the intensity by fractions of a percent, so it might be neglected there.

The small sample size together with the small beam spot requests a more precise and reproducible way to align the sample. Here we want to investigate approaches as used in x-ray or synchrotron experiments. The challenge will be to realise these when using e.g. a cryomagnet.

To suppress the frame-overlap, a bent transmission filter according to section **??** will be constructed and build.

Further tests on Amor are scheduled for May 2013.

# Bibliography

[1] Sang-Wook Cheong and Maxim Mostovoy. Multiferroics: a magnetic twist for ferroelectricity. *NATURE MATERIALS*, 6(1):13–20, JAN 2007.

[2] R. Ramesh and Nicola A. Spaldin. Multiferroics: progress and prospects in thin films. *NATURE MATERIALS*, 6(1):21–29, JAN 2007.

[3] J. Hoppler, J. Stahn, Ch. Niedermayer, V. K. Malik, H. Bouyanfif, A. J. Drew, M. Roessle, A. Buzdin, G. Cristiani, H. U. Habermeier, B. Keimer, and C. Bernhard. Giant superconductivity-induced modulation of the ferromagnetic magnetization in a cuprate-manganite superlattice. *NATURE MATERIALS*, 8(4):315–319, APR 2009.

[4] B. J. Kirby, D. Kan, A. Luykx, M. Murakami, D. Kundaliya, and I. Takeuchi. Anomalous ferromagnetism in TbMnO3 thin films. *JOURNAL OF APPLIED PHYSICS*, 105(7), APR 1 2009. 53rd Annual Conference on Magnetism and Magnetic Materials, Austin, TX, NOV 11-14, 2008.

[5] J. S. White, M. Bator, Y. Hu, H. Luetkens, J. Stahn, S. Capelli, S. Das, M. Döbeli, Th. Lippert, V. K. Malik, J. Martynczuk, A. Wokaun, M. Kenzelmann, Ch. Niedermayer, and C. W. Schneider. Strain-induced ferromagnetism in antiferromagnetic lumno$_3$ thin films. *Phys. Rev. Lett.*, 111:037201, Jul 2013.

[6] A Ohtomo, DA Muller, JL Grazul, and HY Hwang. Artificial charge-modulation in atomic-scale perovskite titanate superlattices. *NATURE*, 419(6905):378–380, SEP 26 2002.

[7] A Ohtomo and HY Hwang. A high-mobility electron gas at the LaAlO3/SrTiO3 heterointerface. *NATURE*, 427(6973):423–426, JAN 29 2004.

[8] J. Mannhart, D. H. A. Blank, H. Y. Hwang, A. J. Millis, and J. M. Triscone. Two-Dimensional Electron Gases at Oxide Interfaces. *MRS BULLETIN*, 33(11):1027–1034, NOV 2008.

[9] Pavlo Zubko, Stefano Gariglio, Marc Gabay, Philippe Ghosez, and Jean-Marc Triscone. Interface Physics in Complex Oxide Heterostructures. In Langer, JS, editor, *ANNUAL REVIEW OF CONDENSED MATTER PHYSICS, VOL 2*, volume 2 of *Annual Review of Condensed Matter Physics*, pages 141–165. 2011.

[10] Marta Gibert, Pavlo Zubko, Raoul Scherwitzl, Jorge Iniguez, and Jean-Marc Triscone. Exchange bias in LaNiO3-LaMnO3 superlattices. *NATURE MATERIALS*, 11(3):195–198, MAR 2012.

[11] A. V. Boris, Y. Matiks, E. Benckiser, A. Frano, P. Popovich, V. Hinkov, P. Wochner, M. Castro-Colin, E. Detemple, V. K. Malik, C. Bernhard, T. Prokscha, A. Suter, Z. Salman, E. Morenzoni, G. Cristiani, H. U. Habermeier, and B. Keimer. Dimensionality Control of Electronic Phase Transitions in Nickel-Oxide Superlattices. *SCIENCE*, 332(6032):937–940, MAY 20 2011.

[12] H Schmidt, M Gupta, and M Bruns. Nitrogen diffusion in amorphous silicon nitride isotope multilayers probed by neutron reflectometry. *PHYSICAL REVIEW LETTERS*, 96(5), FEB 10 2006.

[13] H. Schmidt, U. Geckle, and M. Bruns. Simultaneous diffusion of Si and N in silicon nitride. *PHYSICAL REVIEW B*, 74(4), JUL 2006.

[14] E. Hueger, H. Schmidt, J. Stahn, B. Braunschweig, U. Geckle, M. Bruns, and A. Markwitz. Atomic transport in metastable compounds: Case study of self-diffusion in Si-C-N films using neutron reflectometry. *PHYSICAL REVIEW B*, 80(22), DEC 2009.

[15] Sujoy Chakravarty, Harald Schmidt, Ursula Tietze, Dieter Lott, N. P. Lalla, and Ajay Gupta. Self-diffusion and defect annihilation in nanocrystalline Fe films probed by neutron reflectometry. *PHYSICAL REVIEW B*, 80(1), JUL 2009.

[16] E. Hueger, U. Tietze, D. Lott, H. Bracht, D. Bougeard, E. E. Haller, and H. Schmidt. Self-diffusion in germanium isotope multilayers at low temperatures. *APPLIED PHYSICS LETTERS*, 93(16), OCT 20 2008.

[17] E. Hueger, J. Rahn, J. Stahn, T. Geue, and H. Schmidt. Diffusivity determination in bulk materials on nanometric length scales using neutron reflectometry. *PHYSICAL REVIEW B*, 85(21), JUN 4 2012.

[18] Erwin Hueger, Lars Doerrer, Johanna Rahn, Tobias Panzner, Jochen Stahn, Gerhard Lilienkamp, and Harald Schmidt. Lithium Transport through Nanosized Amorphous Silicon Layers. *NANO LETTERS*, 13(3):1237–1244, MAR 2013.

[19] D. Pantel, S. Goetze, D. Hesse, and M. Alexe. Reversible electrical switching of spin polarization in multiferroic tunnel junctions. *Nature Materials*, 11:289293, 2012.

[20] J. Stahn, T. Panzner, U. Filges, C. Marcelot, and P. Böni. Study on a focusing, low-background neutron delivery system. *N.I.M. A*, page in press, 2010.

[21] J. Stahn, U. Filges, and T. Panzner. Focusing specular neutron reflectometry for small samples. *The European Physical Journal Applied Physics*, 58, 4 2012.

[22] Frédéric Ott and Alain Menelle. Refocus: A new concept for a very high flux neutron reflectometer. *Nuclear Instruments and Methods in Physics Research A*, 586(1):23 – 30, 2008. Proceedings of the European Workshop on Neutron Optics - NOP '07.

[23] F. Ott and A. Menelle. New designs for high intensity specular neutron reflectometers. *European Physical Journal - Special Topics*, 167:93–99, 2009.

[24] Phillip M. Bentley, Shane J. Kennedy, Ken H. Andersen, Damian Martin Rodriguez, and David F. R. Mildner. Correction of optical aberrations in elliptic neutron guides. *N.I.M. A*, 693:268–275, 2012.

[25] L. D. Cussen, D. Nekrassov, C. Zendler, and K. Lieutenant. Multiple reflections in elliptic neutron guide tubes. *NUCLEAR INSTRUMENTS & METHODS IN PHYSICS RESEARCH SECTION A-ACCELERATORS SPECTROMETERS DETECTORS AND ASSOCIATED EQUIPMENT*, 705:121–131, MAR 21 2013.

[26] M. Russina, F. Mezei, and G. Kali. First Implementation of Novel Multiplexing Techniques for Advanced Instruments at Pulsed Neutron Sources. In *5TH EUROPEAN CONFERENCE ON NEUTRON SCATTERING*, volume 340 of *Journal of Physics Conference Series*, DIRAC HOUSE, TEMPLE BACK, BRISTOL BS1 6BE, ENGLAND, 2012. European Nucl Scattering Assoc, IOP PUBLISHING LTD. 5th European Conference on Neutron Scattering (ECNS), Prague, CZECH REPUBLIC, JUL 17-21, 2011.

[27] Maruyama R., Ebisawa T., Tasaki S., Hino M., Takeda M., Kawai T., Kawabata Y., and Sakai K. A resonance neutron-spin flipper for neutron spin echo at pulsed sources. *Physica B*, 335(1):238–242, 2003.

[28] J. Stahn. A switchable white-beam neutron polariser. *Physica B: Condensed Matter*, 345(1-4):243 – 245, 2004. Proceedings of the Conference on Polarised Neutron and Synchrotron X-rays for Magnetism.

[29] R. Cubitt. *N.I.M. A*, 558:547–550, 2006.

[30] R. Cubitt and J. Stahn. Neutron reflectometry by refractive encoding. *Eur. Phys. J. Plus*, 126:111, 2011.

[31] M. Schneider, J. Stahn, and P. Böni. Focusing of cold neutrons: Performance of a laterally graded and parabolically bent multilayer. *Nuclear Instruments and Methods in Physics Research Section A: Accelerators, Spectrometers, Detectors and Associated Equipment*, 610(2):530 – 533, 2009.

[32] M. Gupta, T. Gutberlet, J. Stahn, P. Keller, and D. Clemens. Amor - the time-of-flight neutron reflectometer at SINQ/PSI. *PRAMANA-JOURNAL OF PHYSICS*, 63:57–63, 2004.

[33] A.A. van Well. Double-disk chopper for neutron time-of-flight experiments. *Physica B: Condensed Matter*, 180-181(2):959 – 961, 1992.